University of Alberta

Electronic Structure and Properties of Quaternary Chalcogenides

by

Brent W. Rudyk

A thesis submitted to the Faculty of Graduate Studies and Research in partial fulfillment of the requirements for the degree of

Doctor of Philosophy

Department of Chemistry

© Brent W. Rudyk
Spring, 2014
Edmonton, Alberta

Permission is hereby granted to the University of Alberta to reproduce single copies of this thesis and to lend or sell such copies for private, scholarly or scientific research purposes only. Where the thesis is converted to, or otherwise made available in digital form, the University of Alberta will advise potential users of the thesis of these terms.

The author reserves all other publication and other rights in association with the copyright in the thesis and, except as herein before provided neither the thesis nor any substantial portion thereof may be printed or otherwise reproduced in any material for whatsoever without the author's prior written permission.

Abstract

Several series of quaternary chalcogenides were synthesized by high temperature reactions and their crystal structures were determined by X-ray diffraction methods. Differences in electronic structure were examined by X-ray photoelectron spectroscopy (XPS) and X-ray absorption near-edge spectroscopy (XANES). For some of these compounds, magnetic properties were also measured.

New non-centrosymmetric quaternary chalcogenides $RE_3MM'Ch_7$ (*RE* = La–Er; *M* = Fe, Co, Ni; *M′* = Ga, In; *Ch* = S, Se) were synthesized and characterized. Their structure consists of isolated 1D chains of *M*-centred octahedra and *M′*-centred tetrahedra. Shifts in the XPS and XANES spectra support the assignment of valence states consistent with the charge balanced formulation $(RE^{+3})_3(M^{2+})(M'^{3+})(Ch^{2-})_7$. On proceeding from the sulphides $RE_3MM'S_7$ to the selenides $RE_3MM'Se_7$, the *M*-*Ch* bonds show increased covalent character. The Co 2p spectrum of La_3CoInS_7 exhibits asymmetric line broadening suggestive of electronic delocalization. The *RE* substitution affects the *c*/*a* ratios, which are the largest observed to date for compounds with this structure type, but does not drastically modify the electronic structure. Magnetic measurements indicated predominantly paramagnetic behaviour for most members, but antiferromagnetic ordering at low temperatures is suggested for a few members.

The electronic structures of candidates for p-type transparent oxide semiconductors LaCuO*Ch* (*Ch* = S, Se, Te) were investigated using XPS and XANES. The observation of large XPS binding energy shifts and the analysis of Cu M-edge XANES spectra supports the valence states in the formulation $La^{3+}Cu^{+}O^{2-}Ch^{2-}$. Subtle changes in the fine structure of La 3d core-lines provide evidence for the occurrence of interlayer interactions, namely that charge transfer takes place from the insulating and highly ionic [LaO] layer to the semiconducting and more covalent [Cu*Ch*] layer. This phenomenon was further probed in the solid solution $LaCuOSe_{1-x}Te_x$, in which further evidence for interlayer charge transfer was found; intralayer Cu-to-*Ch* charge transfer within the [Cu*Ch*] layer becomes more pronounced upon substitution with more electronegative chalcogen atoms. Through a comparison of chalcogenide binding energy shifts, a new electronegativity value for Se, intermediate between S and Te, was proposed.

Acknowledgements

Throughout my Ph.D. studies, I have had the fortune to work with many amazing people. The contents of this thesis could not have been completed without their help and support.

First and foremost I would like to thank my supervisor, Prof. Arthur Mar. His constant guidance and encouragement helped shape the researcher that I have become. I am forever grateful for the support and leniency he provided me over all these years. My personal situation was not a typical one, and I am convinced that few supervisors would have had the patience and tolerance for my extremely busy and ever-fluctuating schedule as he did. Through extensive knowledge and the occasional snide remark, Arthur provided a phenomenal atmosphere of learning and development that I will carry with me beyond these walls. I also thank Prof. Ron Cavell for sharing his vast synchrotron knowledge and for his accompaniment on all synchrotron trips.

The Mar group has had a steady but not overwhelming stream of graduate students throughout my time here who've all contributed in some fashion over the last five years. Special thanks goes to Dr. Peter Blanchard for taking me under his wing for my first couple years where he proceeded to teach me XPS and XANES and answer every question I could think to throw his way. Learning to decipher his accent filled in the waiting hours on many long synchrotron trips. His constant pushing helped keep me motivated and moving forward. Special thanks also goes to Dr. Stanislav Stoyko for his assistance with synthesis,

crystallography and the months and months that went in to fixing the PPMS. Not to mention, he is one of the most entertaining concert buddies in recent memory. As for the rest, current and past, I thank you all tremendously.

Dr. Dimitre Karpuzov and friends at the Alberta Centre for Surface Engineering and Science (ACSES) are thanked for allowing me essentially on demand use of the Kratos AXIS 165 spectrometer for all the XPS work done in this thesis. ACSES was established with funding from the Canada Foundation for Innovation (CFI) and Alberta Innovation and Science. As far as XANES goes, I would like to thank Dr. Tom Regier, Mr. Dave Chevier, Dr. Lucia Zuin, and Dr. Andrew Grosvenor and his group for assistance on the SGM (11-ID-1), and PGM (07B2-1) beamlines at the Canadian Light Source (CLS) located at the University of Saskatchewan, Saskatoon, Saskatchewan. Dr. Robert Gordon and Dr. Trudy Bolin are thanked for their assistance on the PNC/XOR-CAT (20-BM) and 9-BM beamlines at the Advanced Photon Source (APS) located at Argonne National Lab in Argonne, Illinois supported by the US Department of Energy – Basic Energy Services and major research support grants from NSERC, the University of Washington, Simon Fraser University, and the Advanced Photon Source.

I would like to thank Dr. Anna Jordan, my TA supervisor, for her continued support through the last four years. Her motivational speeches and no-nonsense approach to pretty much everything helped keep me grounded. The skills I learned during the course of teaching for Anna range from organization to experiment design to teaching styles, all of which can only help me moving forward. Also, she bakes treats. I like treats.

There are far too many friends to mention individually and I fear that I would inadvertently leave someone out. I treasure all the friends I've made over the years and many have contributed substantially to my ability to complete this work and I thank you all from the bottom of my heart. Whether it was a needed distraction, a chemistry discussion, or an impromptu babysitter, I could always count on someone. They know who they are, and more importantly they know how grateful I am for their help and support.

Last, but certainly not least, I would like to thank my family. My Mom and Dad have been a pillar of support in all aspects of my life and this was no different. The help they provided was immeasurable and I am forever grateful. I thank my sister and her family for their moral support and friendly ears. Finally, I would like to thank my beautiful wife Angela, and my wonderful children, Cohen and Jackson. I couldn't have done any of this without your unwavering support.

Table of Contents

List of Tables

List of Figures

List of Symbols and Abbreviations

φ	Work function
ε	Dielectric constant; One-electron energy
θ	Angle of reflection; Take-off angle
λ	Wavelength; Inelastic mean free path
χ	Electronegativity; Magnetic susceptibility
χ_n	Basis function
Ψ	Wave function
μ	Absorption coefficient
θ_p	Weiss constant
μ_{eff}	Effective magnetic moment
1D	One dimensional
2D	Two dimensional
3D	Three dimensional
a b c	Unit cell parameters
AFM	Atomic force microscopy; Antiferromagnetism
APS	Advanced Photon Source
ARXPS	Angle-resolved X-ray photoelectron spectroscopy
ASA	Atomic sphere approximation
BE	Binding energy
C	Curie constant
CCD	Charge-coupled device
Ch	Chalcogen
CHA	Concentric hemispherical analyser
CLS	Canadian Light Source

CN	Coordination number
COHP	Crystal orbital Hamiltonian population
COOP	Crystal orbital overlap population
cps	Counts per second
CS	Coordination sphere
CW	Curie-Weiss
d_{hkl}	d- spacing
DOS	Density of states
e^-	Electron
E_F	Fermi level
E_V	Vacuum energy
EDX	Energy dispersive X-ray analysis
ESCA	Electron spectroscopy for chemical analysis
EXAFS	Extended X-ray absorption fine-structure
FC	Field-cooled
FM	Ferromagnetism
FRAM	Ferroelectric random access memory
FWHM	Full-width-at-half-maximum
g	Landé factor
H	Hamiltonian; Magnetic field
hkl	Miller indices
$h\nu$	Incident energy
I	Intensity of transmitted radiation
I_o	Intensity of incident radiation
I_f	Intensity of radiation produced by fluorescence

I_{ref}	Intensity of radiation transmitted through a reference sample
IR	Infrared
j; *J*	Angular momentum; Total angular momentum
k	Wave vector
KE	Kinetic energy
l; *L*	Orbital angular momentum; Total orbital angular momentum
LED	Light-emitting diode
LMTO	Linear muffin-tin orbital
M	Magnetization; Metal
m_j	Magnetic quantum number
MQW	Multiple quantum well
n	Principle quantum number; Number of valence electrons
NLO	Non-linear optics
NMR	Nuclear magnetic resonance
P_s	Spontaneous polarization
PM	Paramagnetism
Pn	Pnicogen
PNC/XOR-CAT	Pacific Northwest Consortium/X-ray Operations and Research Collaborative Access Team
PPMS	Physical property measurement system
PZT	Lead zirconate titanate, $Pb(Zr_xTi_{1-x})O_3$
q	Point charge
r	Orbital radius
r_{cov}	Covalent radius

RE	Rare-earth
s; S	Screening factor; Spin angular momentum; Total spin angular momentum
SEM	Scanning electron microscope
SGM	Spherical grating monochromator
SHG	Second harmonic generation
t	Sample thickness
T	Temperature; Lattice translations
T_c	Critical temperature; Curie temperature
T_N	Néel temperature
TB	Tight-binding
TCO	Transparent conducting oxide
TM	Transition metal
UPS	Ultraviolet photoelectron spectroscopy
TFY	Total fluorescence yield
TEY	Total electron yield
VLS-PGM	Variable line spacing plane grating monochromator
V	Cell volume; applied voltage
XANES	X-ray absorption near-edge spectroscopy
XAS	X-ray absorption spectroscopy
XPS	X-ray photoelectron spectroscopy
XRD	X-ray diffraction
Z	Atomic number; nuclear charge
Z_{eff}	Effective nuclear charge
ZFC	Zero-field-cool

Chapter 1

Introduction

1.1 Solid state compounds

Solid state chemistry has undergone significant changes, in part because of rapid developments in nanotechnology and materials science. Although exploratory synthesis remains important, greater emphasis is now placed on targeted synthetic strategies. These approaches fall into a few broad categories: (i) design of specific structures, (ii) investigations of the reactivity of different elements, and (iii) modification of known compounds to enhance their properties. Through a combination of the first two approaches, this thesis describes the study of compounds that were chosen because of their particular structure (exhibiting low dimensionality)[1–3] and their element classes (chalcogenides and oxychalcogenides).

Chalcogenides exhibit a rich diversity of structures. Relative to oxides, the smaller electronegativity differences found in the heavier chalcogenides (compounds of S, Se, Te) can lead to interesting bonding networks and different physical properties.[1–6] The contrast persists between nitrides and the heavier pnictides (compounds of P, As, Sb).[7,8] In general, chalcogenides are less toxic than pnictides and are therefore more amenable to applications.[6] The structures of oxides are starkly different from those of the heavier chalcogenides. Because

oxygen atoms are highly electronegative, they tend to repel each other so that more symmetric structures tend to be favoured in oxides.[1] The lower electronegativity of the heavier chalcogen atoms can give rise to less symmetric and low-dimensional structures.[1–4] In this thesis, quaternary chalcogenides containing one-dimensional chains and quaternary oxychalcogenides containing two-dimensional layers are investigated. Their electronic structures and some of their magnetic properties are also examined.

The structures of solid-state compounds consisting of elements with small differences in electronegativity are difficult to predict because they can display many types of bonding within a given structure. Ionic, covalent, and metallic bonding, or a combination thereof, can exist simultaneously in such compounds.[9] When there is a large difference in electronegativity, an ionic model is often helpful in understanding the bonding within the extended structure. Although band structure calculations have long been used as a theoretical tool to probe the electronic structures of solids, experimental techniques have not been applied as frequently. X-ray photoelectron spectroscopy (XPS) and X-ray absorption near-edge spectroscopy (XANES) are potentially attractive techniques to probe electronic structures directly. However, the interpretation of shifts in binding energies in XPS or absorption energies in XANES has not been straightforward, partly because the bonding in chalcogenides and oxychalcogenides has such mixed character and does not follow a simple ionic model.

A major focus of this thesis is the challenging application of X-ray spectroscopy to chalcogenides and oxychalcogenides. In the early development

of these techniques, detailed interpretation of the subtle energy shifts was made difficult by the poor resolution of instruments. However, in recent years, improvements in both instrumental resolution and analytical procedures have permitted meaningful interpretation of these compounds. Within our research group, XPS was first used to examine simple binary transition-metal pnictides and then extended to ternary mixed-metal pnictides.[10–14] Later, quaternary pnictides (e.g., ZrCuSiAs) and rare-earth oxypnictides (e.g., *REM*AsO) were analyzed.[15–17] This latter series of compounds belongs to the set of high-temperature Fe-containing superconductors that have gained worldwide attention in the last few years.[18–22] Their structure consists of $[REO]^{-}$ and $[M\mathrm{As}]^{+}$ layers that alternate along the stacking direction. Current belief for the superconductivity mechanism is that the insulating $[REO]^{-}$ layer acts as an electron reservoir which funnels electrons into the $[M\mathrm{As}]^{+}$ layer, within which conduction takes place.[23,24] Thus, these interlayer interactions should be evidenced by the observation of energy shifts in the X-ray spectra as a manifestation of the charge transfer. However, no such shifts were found in the XPS and XANES spectra, or they were too small to be detected.[15,16] It was hypothesized that replacement of pnicogen by more electronegative chalcogen atoms could enhance the charge transfer to lead to observable energy shifts. Chapters 4 and 5 present investigations along these lines. Further details about X-ray spectroscopy and other characterization techniques are discussed later in this chapter.

1.2 Properties and applications

The classes of compounds examined in this thesis were chosen because of their potential to exhibit interesting physical properties associated with their structures.

1.2.1 Non-centrosymmetric structures and properties

Most compounds crystallize in centrosymmetric space groups, for which the presence of a centre of inversion necessarily leads to a zero dipole moment. In contrast, non-centrosymmetric space groups lack a centre of inversion. An important consequence is that such compounds may exhibit unusual optical (nonlinear optical (NLO) response, second harmonic generation (SHG)) and electrical properties (piezoelectricity, pyroelectricity, ferroelectricity).[25] Among the 32 crystal classes (point groups), 11 are centrosymmetric and not conducive to such properties. Within the remaining classes, 20 have the symmetry required to exhibit piezoelectricity, whereas only 10 possess a unique polar axis required for pyroelectricity. Although pyroelectric compounds are also piezoelectric, the reverse is not necessarily true.[25,26] Pyroelectrics that exhibit reversible electric polarization are called ferroelectrics.

In some cases, compounds with non-zero dipole moments can generate an electrical voltage under an applied external stress, in the absence of an electric field. The external stress is mechanical (e.g., pressure, deformation) in piezoelectric materials but thermal in pyroelectric materials. Care must be taken not to confuse pyroelectric materials, in which the voltage is generated through

heating or cooling of the *entire* body, with thermoelectric materials, in which a voltage is generated through a temperature gradient. Ferroelectricity is manifested by a spontaneous and reversible electric polarization in the absence of an external electric field.[27,28]

There are many compounds that are normally centrosymmetric that undergo transitions which lead to a lowering of symmetry to non-centrosymmetric structures. For example, perovskites ($CaTiO_3$-type) are normally centrosymmetric (space group *Pnma*) (Figure 1-1). However, below a critical temperature T_c (e.g., 408 K for $BaTiO_3$), some can undergo slight deformations such that independent dipole moments arising from displaced atoms combine to a non-zero value.[28] These structural deformations occur and remain persistent because of a phenomenon known as the *polarization catastrophe*.[28] When a distortion takes place below T_c, the displaced atom experiences an electric field created from neighbouring atoms that is strong enough to overcome the natural

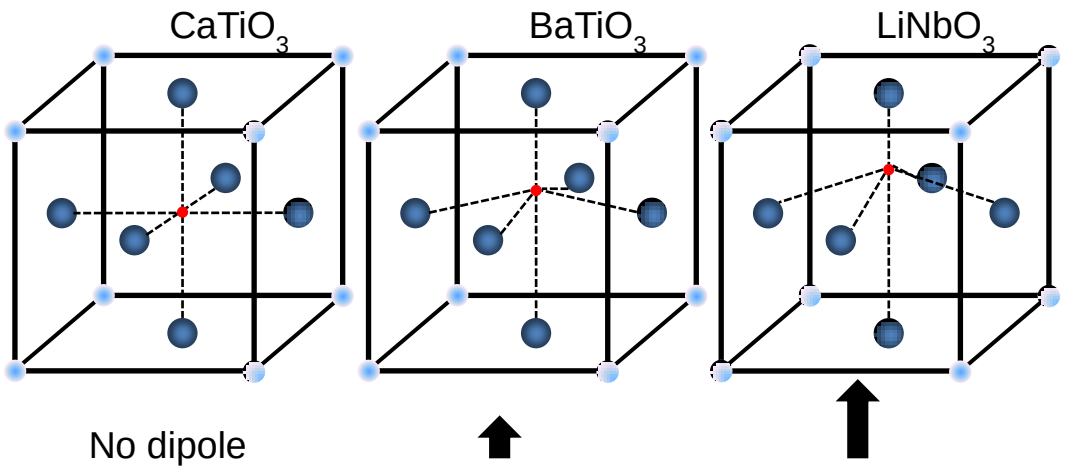

Figure 1-1 Schematic representation of structural transitions in perovskites that induce a non-zero net dipole moment. The degree of polarization changes with element substitution.

tendency for the atom to return to its original position due to elastic restoring forces. The result is a permanent distortion. Table 1-1 lists values for the critical temperature T_c and spontaneous polarization P_s for a selection of ferroelectric perovskites.[28,29] Another figure of merit, the dielectric constant ε, is sometimes quoted; it is directly proportional to the polarizability of a medium, so that a high ε is desirable.

Table 1-1 Ferroelectric figures of merit for selected perovskites.

Compound	T_c (K)	P_s ($\mu C\ cm^{-2}$)
$BaTiO_3$	408	26
$KNbO_3$	708	30
$PbTiO_3$	765	50
$LiTaO_3$	938	50
$LiNbO_3$	1480	71

Structural deformations can thus induce an asymmetry that enhances the overall dipole moment and, in turn, induce non-centrosymmetry-based properties such as ferroelectricity. Greater distortions give rise to larger dipole moments and increased spontaneous polarization; for example, the cations shift ~0.1 Å in $BaTiO_3$ and 0.5–0.9 Å in $LiNbO_3$.[28] The idea of introducing enhanced structure distortions is revisited in Chapter 3.

The ability to generate a voltage from external stimuli, or the reverse process of inducing an external response by applying a voltage, finds many interesting applications. Piezoelectric materials are used as actuators, transducers, capacitors, and sensors.[30] For example, lead zirconate titanate, $Pb(Zr_xTi_{1-x})O_3$ (PZT), is a commonly used ceramic piezoelectric material that is highly versatile

because its dielectric constant can be tuned for various uses.[31,32] Piezoelectric materials are used to precisely adjust positions in apparatus such as AFM stages in which extremely small changes in dimensions can be delivered through applied voltages. The reversible nature of ferroelectric materials is exploited in low-power, long-lasting memory storage devices such as FRAM.[33]

1.2.2 Layered structures and properties

There has been a resurgence of interest in layered compounds, particularly oxides, in large part because of recent discovery of Fe-based high-temperature oxypnictide superconductors.[18–22] Predating the oxypnictides, the less well-known oxychalcogenides were initially identified as potential candidates for use in optoelectronic devices.[34–42] As in the oxypnictides, the properties of the oxychalcogenides are connected to the layered structure adopted (Figure 1-2a).

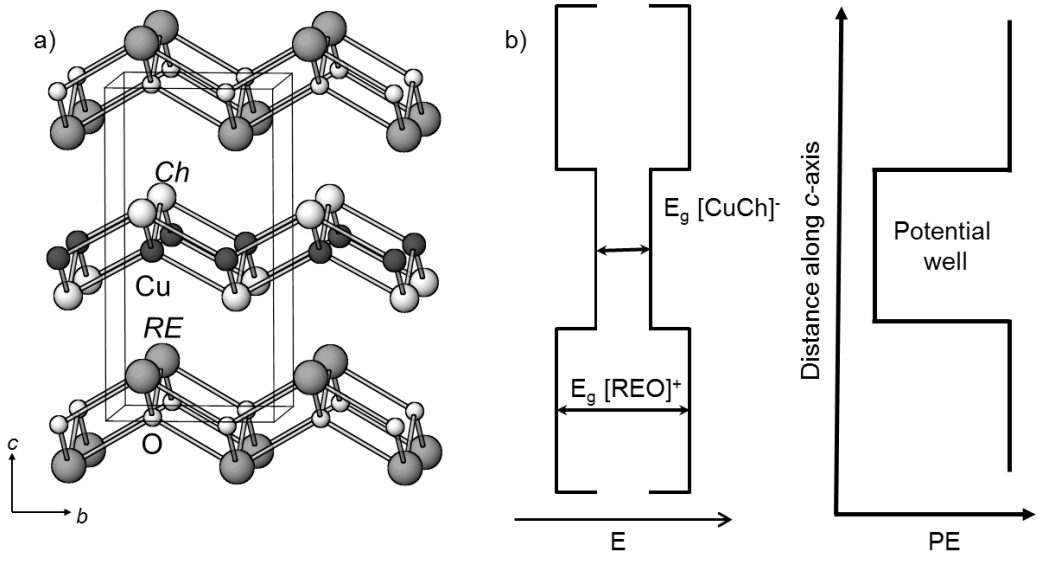

Figure 1-2 (a) Layered crystal structure formed for *RE*CuO*Ch*. (b) Comparison of relative band gap sizes for each layer and the potential well generated.

The sizeable band gap (2.8–3.3 eV) of the oxychalcogenides renders them attractive materials for transparent electronics. The structure is marked by a subtle interplay between two distinct layers. This stacking of nearly independent layers generates what has been described as a pseudo-heterostructure with highly 2D character. There is a large difference in the relative magnitudes of the band gaps of these two types of layers (as determined from density of states calculations) (Figure 1-2b). The [LaO] layer is sufficiently insulating that a potential well is created, which confines the charge carriers to the more conducting (smaller band gap) [Cu*Ch*] layer.[34–42]

A prototypical transparent electronic device is shown in Figure 1-3. It is composed of a *p*-*n* junction grown on an appropriate substrate (e.g., MgO (001)).[42] The compounds chosen to act as the transparent conducting oxides (TCO) for a given device will dictate how it operates. For example, *p*-LaCuOSe coupled with *n*-$InGaZn_5O_8$ combine to form a blue LED when under an applied voltage.[42] More intricate device design and careful choice of components can

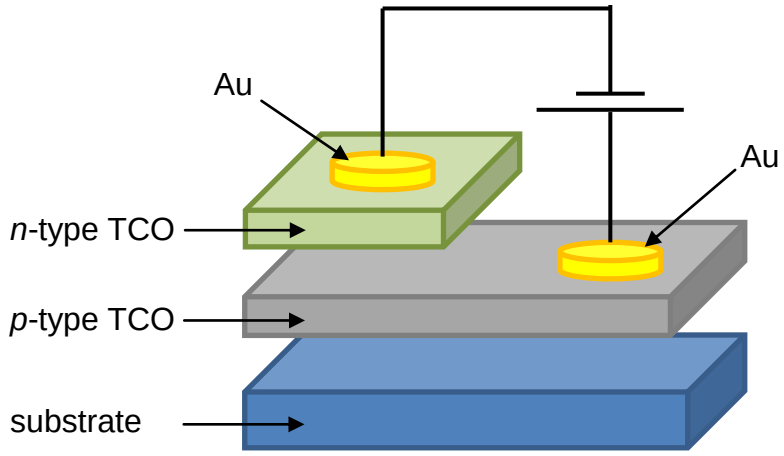

Figure 1-3 Schematic of a general *p*-*n* junction device.

lead to the development of transparent conductive electronic components (*p*-$ZnRh_2O_4$ with *n*-ZnO make a transparent diode).[42]

To construct a working device, each side of the *p*-*n* junction must meet certain requirements: high optical transparency, high electrical conductivity, which stems from high carrier concentration (>10^{19} cm^{-3}), and high carrier mobility (>1 cm^2 V^{-1} s^{-1}).[34–42] The unfortunate reality here is that carrier concentration and carrier mobility are inversely proportional as are high optical transparency and high electrical conductivity, so finding suitable candidates can be difficult. Historically, appropriate *n*-type semiconductors have been easier to make. Well-known compounds that have been long used include In_2O_3, SnO_2, and ZnO. The current industry standard for *n*-type transparent conducting oxides is indium tin oxide (In_2O_3 doped with 10% SnO_2), which has highly tunable properties, but generally has carrier concentrations close to 1×10^{21} cm^{-3} and carrier mobilities ranging from 18–54 cm^2 V^{-1} s^{-1}, both of which are well above the required benchmarks.[43,44] The major problem that arises is that appropriate *p*-type semiconductors are more difficult to identify. First, hole mobility is inherently slower than electron mobility. For example, *n*-type single crystal silicon (with electrons as carriers) has a mobility of 90 cm^2 V^{-1} s^{-1}, whereas *p*-type silicon (with holes as carriers) has a mobility of 50 cm^2 V^{-1} s^{-1} at a carrier concentration of ~10^{20} cm^{-3}.[45] Second, it has proven exceedingly difficult to find a *p*-type semiconductor with an appropriate band gap that satisfies all the necessary conditions. In 1997, Hosono et al. discovered $CuAlO_2$, opening up an entirely new field of exploration.[46] However, $CuAlO_2$ and other early Cu-based

p-type semiconductors suffered from low hole concentration and low hole mobility. The idea to extend to the layered oxychalcogenides, *RE*CuO*Ch*, discussed within this thesis, was the result of the targeted synthesis approach mentioned earlier.[42] In principle, the incorporation of *Ch* valence *p*-orbitals near the Fermi level would allow mixing with the Cu 3d states to create a hybridized set of orbitals that would be more dispersed in energy than the O 2p orbitals in $CuAlO_2$, resulting in a reduced effective carrier mass and thus increased mobility.[42] This was indeed observed experimentally, and an entirely new series of functional materials was identified. LaCuOSe has carrier concentrations on the order of 10^{20} cm^{-3}, and mobilities of ~8 cm^2 V^{-1} s^{-1}, depending on the doping level.[42]

1.3 Diffraction

In molecular chemistry, the most commonly used techniques include NMR spectroscopy, IR spectroscopy, and mass spectrometry. In solid state chemistry, these methods are not typical. By far the most important technique is X-ray diffraction, which is used to identify the structures of solid-state compounds. XRD can be applied to powder and single-crystal samples, but the underlying principles are the same. X-rays are scattered by the periodic arrangement of atoms in an extended crystal structure; they undergo constructive and destructive interference to form a characteristic diffraction pattern which can be analyzed to extract structural information.[47] The general protocol in analyzing products of solid state reactions is to initially identify the phases present through

powder XRD, and then to determine the detailed crystal structures if required through single-crystal XRD.

XRD can be conveniently analyzed as a series of reflections across different sets of lattice planes (identified by Miller indices, (*hkl*)) separated by constant *d*-spacings.[47,48] This description is physically inaccurate, because the X-rays are really not reflected off crystal planes, but rather scattered by atoms. However, the model yields the same results for the angles at which diffracted X-rays are found.

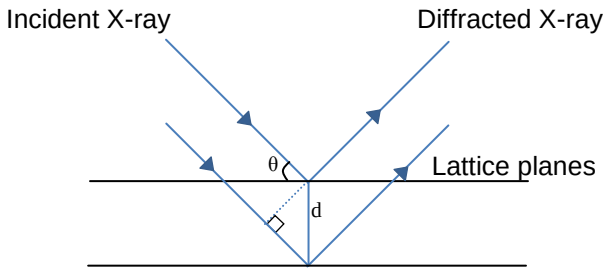

Figure 1-4 Diffraction of X-rays off crystal lattice planes to satisfy Bragg's Law.

Bragg's law is a general equation that describes the conditions required, as depicted in Figure 1-4, for constructive interference of scattered X-rays:[47,48]

$$\sin\theta = n\lambda/2d_{hkl} \qquad \text{(Equation 1-1)}$$

where λ is the wavelength of the incident X-ray beam (usually Cu $K\alpha_1$ in powder XRD, or Mo $K\alpha_1$ in single-crystal XRD), d_{hkl} is the spacing between parallel planes with Miller indices (*hkl*), θ is the angle of diffraction, and *n* is the order of diffraction. The angle made between the incident and diffracted X-ray beam is 2θ. The equation can be simplified by noting that higher order reflections from planes (*hkl*) are equivalent to first order reflections from planes (*nh*, *nk*, *nl*):

$$\sin\theta = \lambda/2d_{hkl} \qquad \text{(Equation 1-2)}$$

1.3.1 Powder XRD

Powder XRD can be considered to be a two-dimensional projection of the three-dimensional array of reflections that would occur in single-crystal XRD, with symmetry-equivalent reflections overlapping at the same diffraction angle 2θ. Randomly oriented crystallites allow for the collection of average reflections for all diffraction angles simultaneously.[48] It is generally quite difficult to determine the crystal structure of an unknown compound directly from powder XRD. However, if a model is suspected to be likely, the structure can be determined through Rietveld refinement.[47,49] In this process, the combined information from the peak positions (which depend on unit cell parameters) and intensities (which depend on atom type and positions) is analyzed. In this thesis, powder XRD patterns were used mainly for qualitative analysis and not for structure determination.

Some of the quaternary compounds investigated in this thesis, such as the oxychalcogenides (e.g., LaCuO*Ch*) are difficult to obtain in the form of suitable single crystals. In these cases, powder XRD becomes the essential method of structural characterization. It is critical, of course, that such samples are crystalline. Amorphous components within the sample do not generate reflections in the XRD pattern and thus cannot be detected. A particular crystal structure gives rise to a unique set of reflections with *d*-spacings and intensities in the powder XRD pattern. Related structures can give similar patterns and care must be taken to recognize minor peaks and small differences in peak positions and intensities to distinguish between these phases. Qualitative phase analysis

proceeds by matching of simulated patterns, which are generated through crystallographic parameters of known compounds or isostructural ones, with the observed patterns, as shown in an example in Figure 1-5. Cell parameters are then refined through the use of various peak matching programs such as UnitCell or CSD.[50,51]

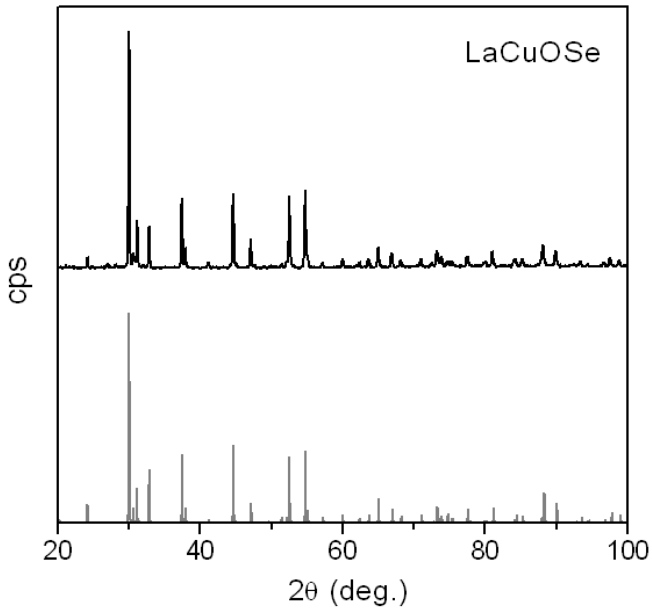

Figure 1-5 Sample XRD pattern of LaCuOSe experimental (top) compared to calculated (bottom).

1.3.2 Single-crystal XRD

Although powder X-ray diffraction is helpful for phase identification and for refinement of cell parameters, it is desirable whenever possible to determine accurate structural information through single-crystal X-ray diffraction. Crystallographic analysis is discussed in detail in many textbooks;[48,52,53] herein, only an overview is given of the fundamentals of data collection and refinement procedures.

A suitable single crystal, typically with dimensions of ~0.1–0.5 mm, is mounted on a glass fiber which is placed on a goniometer head of a single-crystal diffractometer (Bruker PLATFORM diffractometer equipped with a SMART APEX II CCD area detector and a graphite-monochromated Mo Kα radiation source). A few frames of intensity data are collected and inspected to ensure that reflections are sharp and that the crystal does not suffer from twinning or other problems. Data collection proceeds through the recording of many frames of reflection intensities. Most of the compounds studied in this work were of known structure types, so developing structural models was a relatively simple task, with initial atomic coordinates taken from isostructural compounds. Structural refinement proceeds through a comparison of calculated and observed intensities of reflections, carried out through routine crystallographic programs (SHELXTL).[54] Through a least-squares analysis, the differences of the squares of the calculated and observed intensities are minimized by adjusting crystallographic parameters (atomic positions, displacement parameters). The residual (*R*-value) and the goodness-of-fit are measures of the reliability of a crystal structure determination. Generally, a good structure refinement leads to an *R*-value of less than 0.10 and a goodness-of-fit of close to one.[48] However, the resulting structure must also show reasonable displacement parameters and, foremost, make chemical sense.

Crystallographic analysis alone is not a definitive characterization method. It is of utmost importance to confirm the chemical composition of single-crystal

samples through other independent means. A common spectroscopic method for determining chemical composition is energy-dispersive X-ray analysis (EDX).

1.4 X-ray spectroscopy

X-ray photoelectron spectroscopy (XPS) and X-ray absorption spectroscopy (XAS) are used to examine the electronic structures of ternary and quaternary chalcogenides. XPS is a smaller scale, laboratory method performed locally, whereas XAS techniques require the use of a synchrotron facility, such as the Canadian Light Source (CLS) in Saskatoon, Saskatchewan, or the Advanced Photon Source (APS) in Argonne, Illinois. Like XPS, EDX is a small-scale, laboratory method; spectra were collected on single-crystals using a JEOL JSM-6010LA scanning electron microscope (SEM).

1.4.1 Energy-dispersive X-ray analysis

In a sample containing many elements, it is possible to uniquely identify the chemical composition. When the sample is examined in a SEM, the bombarding electrons eject core-level electrons from the atoms of different elements. These excited atoms then relax through the emission of X-ray photons with wavelengths characteristic of the energy levels of the specific element. The presence of a given element is identified by a unique pattern of X-ray wavelengths. The intensities of the characteristic X-rays are directly proportional to the concentration of the source element.[55] Errors on these concentrations are

typically around 2-3%, but they can also depend on the sample mounting and smoothness (e.g., a smooth, flat sample will generally give a lower error).

1.4.2 X-ray photoelectron spectroscopy

XPS (originally termed electron spectroscopy for chemical analysis (ESCA)) was developed by Kai Siegbahn in 1954 and remains a powerful technique to analyze electronic structures.[56] XPS has traditionally been considered to be a surface sensitive technique, but under certain conditions information about the bulk solid can be inferred. XPS provides information about chemical composition, oxidation state, and bonding. The basic principle behind XPS is the photoelectric effect, a phenomenon which was discovered by Hertz in 1887 and later explained by Einstein.[56] Electromagnetic radiation incident on matter is absorbed and a photoelectron is emitted:

$$M \overset{h\nu}{\rightarrow} M^{+} + e^{-} \qquad \text{(equation 1-3)}$$

This photoelectron is completely ejected from the system and its kinetic energy (KE) is measured. The KE of the photoelectron is characteristic of the element from which it originates and depends on the valence state as well as interactions with neighbouring atoms:[56,57]

$$h\nu = KE + BE + \varphi \qquad \text{(equation 1-4)}$$

The binding energy (BE) is the energy required to excite a core-level electron to the Fermi level (E_F), and is characteristic of different elements and the electronic environment.[56,57] The work function (φ) is the energy required to bring the photoelectron from the Fermi level to the vacuum (E_v). Although the KE is the

quantity measured experimentally, this equation permits the determination of BE, the quantity of interest.[56]

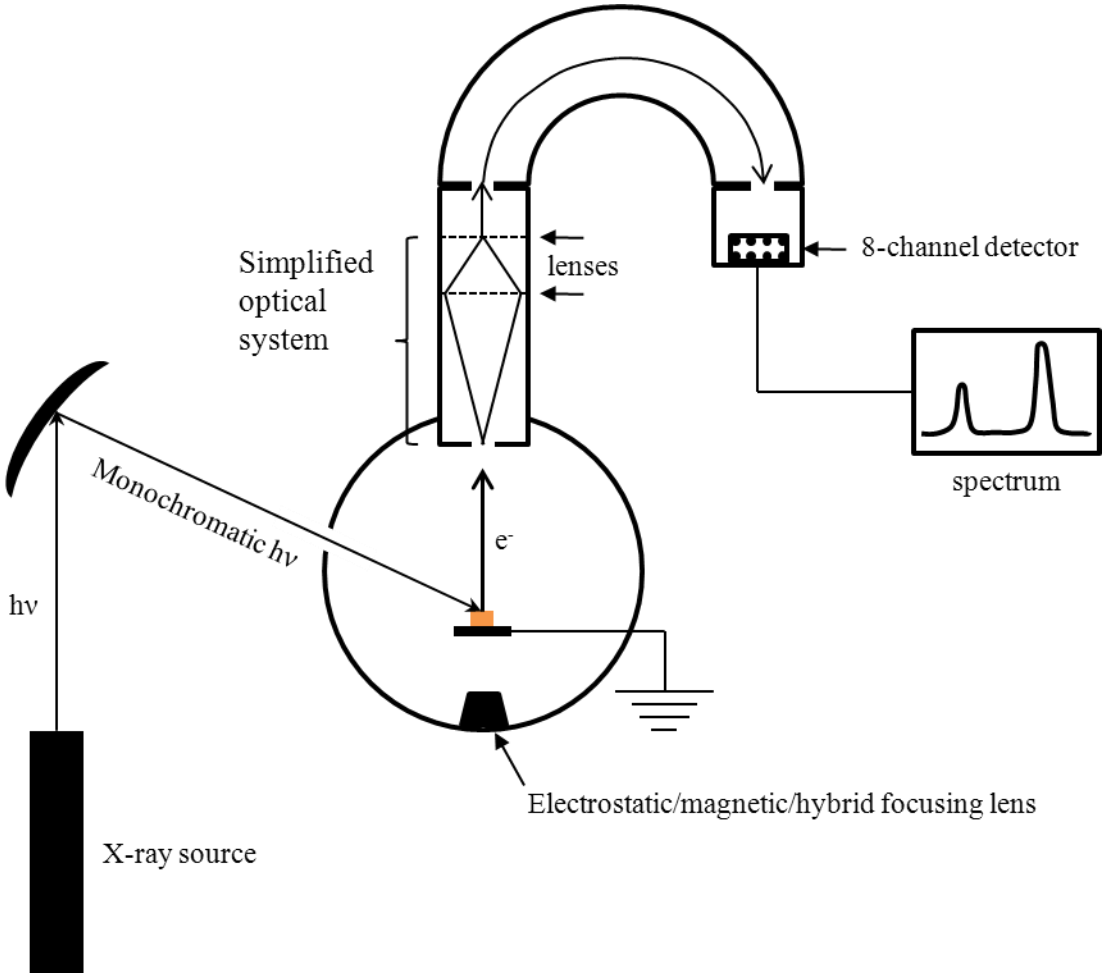

Figure 1-6 Box diagram of a generic XPS instrument equipped with monochromatic X-ray source and 8-channel detector.

A schematic of a generic XPS instrument is shown in Figure 1-6. The process begins with the irradiation of a sample with X-rays, typically monochromatic or achromatic, from an Al Kα or Mg Kα source, or a synchrotron source. For the related technique of Ultraviolet Photoelectron Spectroscopy (UPS) a helium source is used.[58] In XPS, monochromatic Al Kα radiation is generally preferred for the substantial increase in resolution,[56] but where

necessary achromatic radiation can be used. The sample is mounted on a grounded stage. The angle between the monochromatic X-rays and the transfer lens is set to 54.7° to minimize the orbital angular symmetry factor and increase spectral resolution.[56] The ejection of a photoelectron and its detection proceeds through several steps (Figure 1-7). The photoelectron overcomes the BE to reach the Fermi level, and then is further promoted to the vacuum by overcoming the work function. Unfortunately, the work function depends on the identity of the sample and is not normally known experimentally because there is no reference point from which it can be measured. To overcome this problem, two new work functions are introduced: a spectrometer work function, φ_{sp}, which is instrument-specific, and a contact work function, $\varphi_{contact}$, which is the difference

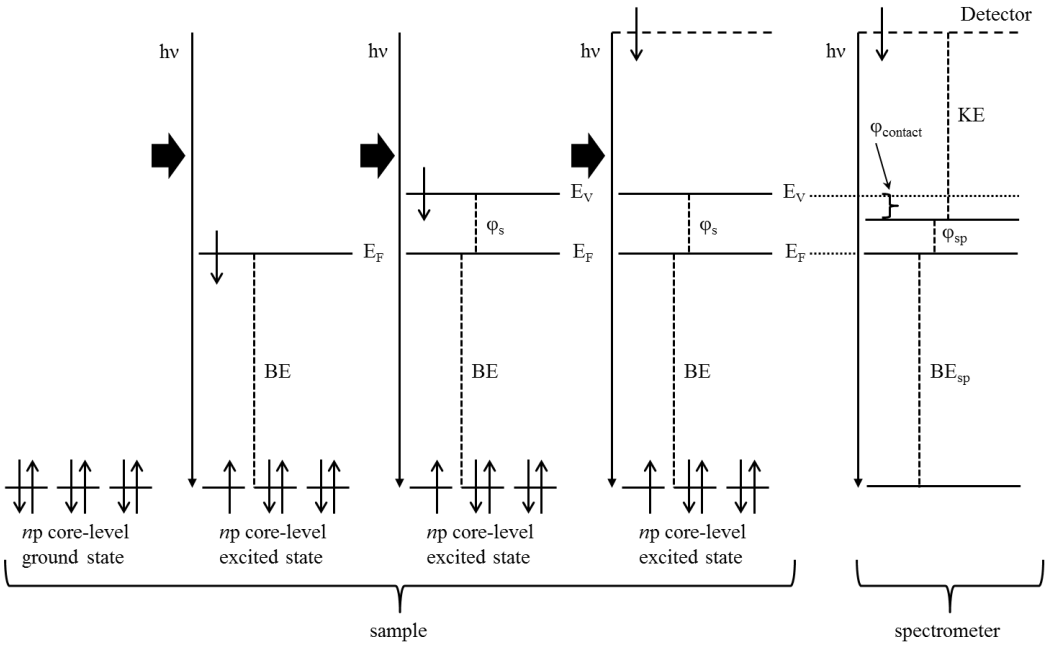

Figure 1-7 Schematic diagram showing sequential steps in the ejection and measurement of a photoelectron.

between the sample work function and the spectrometer work function.[56] By pinning the Fermi level of the sample to the Fermi level of the spectrometer, equation 1-4 can be rearranged as follows:

$$BE = h\nu - \varphi_s - \varphi_{contact} - KE \quad \text{(equation 1-5)}$$

$$BE = h\nu - \varphi_s - \left(\varphi_{sp} - \varphi_s\right) - KE \quad \text{(equation 1-6)}$$

$$BE = h\nu - \varphi_{sp} - KE \quad \text{(equation 1-7)}$$

The spectrometer work function can be determined accurately through calibration with a known sample, typically the 4f core-line of Au.

Once the photoelectron is completely ejected from the sample, it is focused by a combination of electrostatic and magnetic lenses and enters a transfer chamber, where it is again focused through further lenses and mirrors.[56,57] At the end of the transfer chamber, the photoelectron encounters a retarding energy and an entrance slit. The purpose of the retarding energy is to limit the energy of the particles that are allowed to enter the concentric hemispherical analyzer (CHA) to a pass energy that is set to a fixed value.[56,57] By scanning through the retarding field, all photoelectrons generated are slowed to the same pass energy. This procedure sets the benchmark for the measured KE of a photoelectron. By adjusting the pass energy to a lower value, fewer photoelectrons will enter the analyzer and arrive at the detector. Lower pass energies will result in a higher resolution in the final spectrum, but will suffer from lower count rates.[56,57] Spectra that suffer from low count rates (e.g., low concentration samples) may require a higher pass energy to increase the intensity without jeopardizing the fine structure.

At this point, the CHA filters only those photoelectrons with the chosen pass energy to proceed to the detector. The CHA is composed of two concentric hemispherical plates to which negative voltages ($-V_1$ and $-V_2$) are applied, the more negative to the top plate.[56] The two potentials are chosen so that photoelectrons that slip through the retarding field with higher or lower energies will either curve too much or too little and collide with the analyzer walls.[56] Once through the CHA, the photoelectrons are collected in a series of 8 Channeltron detectors, amplified to a pulse current and read by the instrument as individual events. The spectra are plotted as counts per second (cps) versus KE.[56]

As in EDX analysis, XPS also permits quantitative analysis of samples, because the number of photoelectrons is proportional to the concentration of the elements.[57] For accurate determination of BEs, the spectra are additionally calibrated to a reference standard. Normally the C 1s peak arising from adventitious carbon (residual carbon in the atmosphere) is set to a BE of 284.8 eV.[56]

Perhaps the most difficult obstacle to overcome with respect to obtaining good quality spectra deals with the phenomenon known as charging. The ejection of a photoelectron necessarily leaves behind a residual positive charge. If the sample is sufficiently conducting (e.g., metallic) then the same grounding that is responsible for pinning the Fermi levels also acts to funnel electrons back into the sample to replace those that were ejected.[56] However, in cases where the sample is not sufficiently conducting (e.g., insulating samples or problems with sample mounting), the constant depletion of core electrons can result in a significant

build-up of positive charge which can unduly alter the final spectrum. The most common manifestation of charging is an instrumental shift to a more positive binding energy, but this can be easily rectified by the calibration process.[56] When the charging is severe, peaks can be completely obscured by the background and cannot be detected.

In most cases where grounding is not sufficient, artificial replenishment of core electrons can be provided by bombarding the sample with low energy electrons from a tungsten filament.[56] By fine tuning the parameters of the bombardment to compensate for the photoemission process, the effects can be minimized. However, sometimes differential charging can occur when the sample conduction is not uniform. This leads to poorly resolved peaks and in the worst cases, multiple core-lines present for the same sample. Remounting the sample to improve conductivity is an option, but it may be easier to prepare the sample in extreme insulating conditions (prepared on double sided Scotch tape) to ensure the entire sample is insulating and will require charge neutralization throughout.

Because of the surface sensitive nature of the technique, exposure to even minimal amounts of air can introduce impurities in the form of surface oxides, which can obscure signals from the sample. Handling the sample in an inert atmosphere is recommended but not always practical. Samples that have been exposed to oxygen can be cleaned by sputtering with Ar^+ ions to remove surface oxides. However, sputtering can cause adverse effects such as the preferential removal of lighter elements and selective reduction of other elements. Thus it is important to limit exposure and to carefully monitor the effects of sputtering.

Several mechanisms can take place as a photoelectron escapes from the surface. Each time a photoelectron is scattered, it loses part of its initial kinetic energy, which corresponds to an apparently higher binding energy. Only those photoelectrons that escape without collision contribute to the observed core-lines. The average distance that an electron can travel before being scattered is called the inelastic mean free path, λ; within a value of 3λ, there is a 95% chance that the photoelectron will be scattered and lose energy.[57] Scattered electrons that escape contribute to the background and may sometimes even generate satellite peaks. A typical value for λ is 1–3 nm, meaning that a photoelectron must originate from no more than 3–9 nm from the surface to have greater than 5% chance of escaping.[56,59] The analysis depth follows the equation $d = 3\lambda \cdot \sin\theta$ and is thus maximized at an angle of incidence of 90°.[57] This relationship can be exploited to probe how surface structure varies with depth through a technique called angle-resolved photoelectron spectroscopy (ARXPS).[56,60] To analyze bulk samples with XPS they must be finely ground and mounted such that the first ~10 nm of the sample is representative of the bulk.

Two types of spectra are typically collected in XPS experiments.[56] First, a survey spectrum is a wide scan (step size of ~0.7 eV, pass energy of 160 eV, 180 s sweep time) through the entire energy range and is used to check the presence of the expected elements and their concentration. It is also used to confirm the removal of oxides from the sputtering procedure. The survey spectrum is marked by a stepped background which arises from the energy loss of photoelectrons as they escape the surface. This stepped energy-loss background is most frequently

fit to a Shirley-type background.[61] A representative survey spectrum is shown in Figure 1-8. Once core-level peaks are identified for further analysis, a higher resolution spectrum is obtained by selecting a narrower binding energy range. High-resolution spectra are collected with the same sweep time (180 s) as a survey spectrum, but with much smaller step size (~0.05 eV) and pass energy (~20 eV).

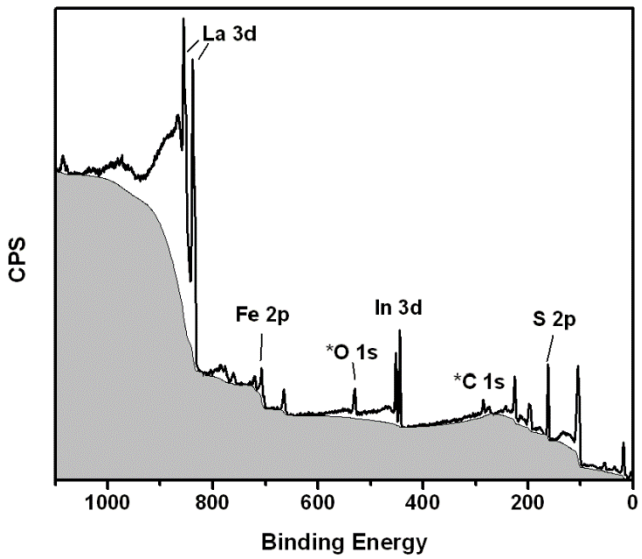

Figure 1-8 Survey spectrum of La_3FeInS_7. Sample has been sputtered, but contains trace amounts of oxygen. The shaded region is the energy-loss background arising from inelastic collisions fit with multiple regions of Shirley-type background spread out to cover the entire region. Core-lines that were focussed on are labelled. C 1s arises from adventitious carbon and was used for calibration.

In the early development of XPS, the simplest interpretation was that the BE of the photoelectron is equal to the energy difference between the excited state (M^+) and the ground state (M) of an atom (Koopman's theorem).[62] The ejection of a photoelectron is an ionization event; the remaining atom with its core hole is

assumed not to relax ("the frozen-orbital approximation") and can be described by a single wave-function.[56,57,62] Although this interpretation was adequate at the time, it is too simplistic and could not explain features which emerged in higher resolution spectra.

Core-line peaks originating from energy levels with an orbital angular momentum (l) greater than zero (i.e., p-, d-, and f-orbitals) are split into two components. This occurs because there are two possible orientations of the electron remaining in the core level.[56,57] An example for Cu 2p is shown in Figure 1-9. The energy difference between the two peaks is called the exchange energy which is proportional to the spin-orbit coupling of the electron in the final state, as well as to $1/r^3$ (r = orbital radius), the orbital angular momentum, and the atomic number of the element.[56]

Spin-orbit coupling represents the interaction of the orbital angular momentum with the spin momentum of an electron. It is evaluated through a vector summation, which can be performed in two ways: *j–j* coupling and *L–S* (Russell-Saunders) coupling.[56] For heavy elements ($Z > 75$), *j-j* coupling is used. The angular momentum (j) is calculated for each electron individually as $j = l + s$ and then summed over all the electrons to give the total angular momentum for the atom, $J = \Sigma j$. For lighter elements, *L–S* coupling is used.[56] The total orbital (L) and total spin (S) angular momenta are calculated for all electrons individually and the resultant values are combined to give the total angular momentum of the atom, $J = |L \pm S|$.[56] Common spectroscopic notations, nl_j, indicate the orientation of the spin of the remaining core electron (spin-up, $j = l + s$; spin-down, $j = l – s$)

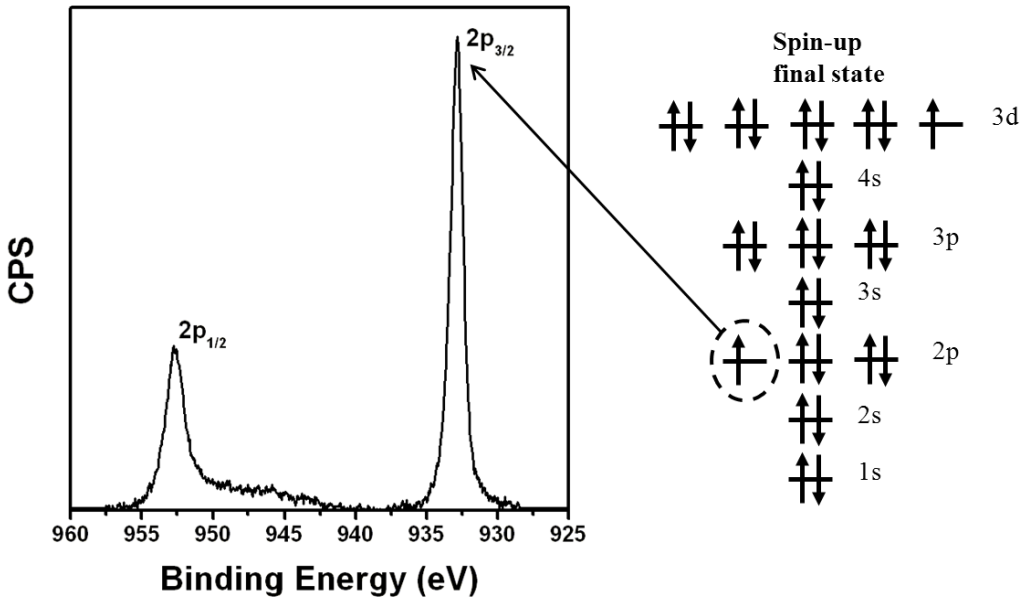

Figure 1-9 High resolution Cu 2p XPS spectrum for LaCuTeO. Spin-orbit split core-lines are appropriately labelled. Accompanied by an orbital diagram representing the more stable spin-up final state configuration.

in the final state.[56] The spin-up orientation is always the most intense and the lowest in energy.[56,57] The intensity ratio of the peaks is related to the degeneracy of the final states, which is equal to $2j+1$, the number of possible values of m_j (ranging from $-j, j+1,\ldots,+j$). For example, any p-orbital ($l = 1$) will give rise to two peaks, $np_{3/2}$ and $np_{1/2}$ in a 2:1 intensity ratio.[56,57] For s-orbitals, which have zero orbital angular momentum ($l = 0$), no spin-orbit coupling occurs and only one peak is observed.

The line shape of core-line peaks can provide useful information.[56] Core-line peaks that are symmetric are normally fit to a pseudo-Voigt function which is a combination of Gaussian and Lorentzian (~70%/30%) functions.[56] This line shape originates from spectrometer and lifetime broadening effects. The full-width-at-half-maximum (FWHM) depends on the analyzer resolution, the spectral

width of the X-ray source, and the natural line width of the core line. The contributions from the analyzer and the X-ray source width (0.85 eV for Al Kα; 0.7 eV for Mg Kα) are sample independent, but the natural line width depends on the core-hole lifetime.[56,57] This lifetime varies with relaxation mechanisms; a shorter lifetime gives a broader peak.[56,57] Line widths can be used to distinguish between different valence states. For example, the Cu $2p_{3/2}$ core line is markedly wider for Cu^{2+}-containing compounds (e.g., CuO)[63] than Cu^{1+}-containing compounds[64,65] because the core-hole lifetime of Cu^{2+} is much shorter than that of Cu^{1+}.[56]

When an atom already has unpaired electrons (e.g., transition metal or rare-earth atoms with partly filled d- or f- subshells), these can couple with the remaining core electron leading to more complicated line shapes (e.g., multiplet splitting).[56,66–70] Metals or small band-gap semiconductors typically show asymmetric line shapes with a tail towards higher binding energies. The photoemission process can cause valence electrons to be promoted into empty conduction states (a kinetic-energy loss process for the photoelectron). The presence of a continuum of states causes a tail instead of a discrete satellite. Satellite peaks can be generated if there are energy levels available for the promotion of a valence electron.[71,72] Various mechanisms such as shake-up, shake-down, and shake-off processes can generate satellites.[73–75]

BE shifts provide valuable chemical information because they depend on the type of element, its coordination environment, and the nature of its bonding to neighbouring atoms.[56] Because electrons in cationic species experience a higher

Z_{eff} they are more difficult to remove and lead to higher BE relative to the neutral atom. Conversely, electrons in anionic species have lower BE. The screening of the core electron from the nuclear charge can be estimated through Slater's rules. The degree of ionic and covalent bonding character can also have an effect on the binding energy. A greater electronegativity difference between elements in a bond will increase the ionic nature, which will reduce the nuclear screening and give a higher BE shift. Second and higher coordination sphere effects are possible to detect, and will be discussed in more detail in later chapters.

1.4.3 X-ray absorption near-edge spectroscopy (XANES)

Although XPS has advantages of being easily performed in a laboratory setting, it suffers from difficulties in interpretation arising largely from final-state effects. An alternative technique is XANES, in which final-state effects are minimized because the core electrons are not ejected entirely out of the atom. As a result, the associated absorption energies are more representative of local chemical environments. The main inconvenience of XANES is that it must be performed in a large scale synchrotron facility. Synchrotron radiation, which is generated by the bending of electrons travelling close to the speed of light, is highly resolved, intense, and tunable. Further details about synchrotron radiation can be found elsewhere.[76,77]

XANES is an absorption process that follows the Beer-Lambert law:[78]

$$I = I_0 e^{-\mu t} \qquad \text{(Equation 1-8)}$$

where I_0 is the incident radiation intensity, I is the transmitted intensity, μ is the absorption coefficient, and t is the sample thickness. In a typical XANES experiment, there are three modes of detection, as depicted in Figure 1-10.[78]

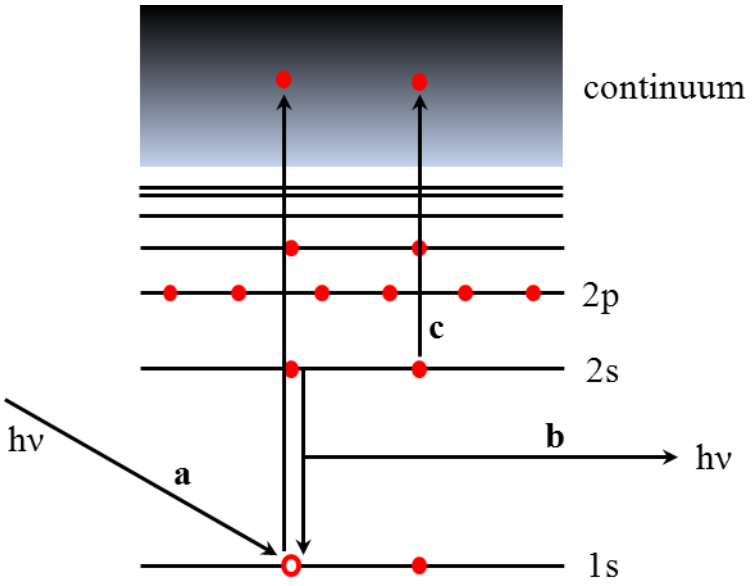

Figure 1-10 Schematic showing the possible detection mode processes. (a) Direct absorption resulting in core-hole generation, "transmission mode"; (b) electronic relaxation into core-hole producing fluorescence, TFY; (c) electronic relaxation resulting in generation of an Auger electron, which combines with photoelectron for TEY.

First, in transmission mode, the preferred method of detection, the transmitted intensity is directly measured and converted to absorbance through the Beer-Lambert law:

$$\mu(E) = \log\frac{I_0}{I} \qquad \text{(Equation 1-9)}$$

where the sample thickness remains constant and can be omitted because only relative values are of importance.[78] This approximation works well if the sample thickness is negligible and the transmitted intensity is high. However, this

approximation fails when the absorption edges require the use of low incident X-ray energies, so that the transmitted intensity is inherently weak. Thus a second method of detection, called total fluorescence yield (TFY), can be used in which the transmitted intensity is inferred from the fluorescence that takes place as the excited atom relaxes.[78] When the core hole is filled by a higher energy electron, a photon is emitted with an intensity I_f. This process is independent of the incident energy and proportional to the photoionization cross-section of the original photoelectron.[78] The absorbance is then proportional to the ratio of fluorescence intensity to incident intensity I_o:

$$\mu(E) = \frac{I_f}{I_o} \qquad \text{(Equation 1-10)}$$

A third method of detection, called total electron yield (TEY), measures the electrons, rather than photons, that are emitted from the sample during this relaxation process.[78,79] This includes Auger electrons, secondary electrons, and backscattered electrons.[78,79] Because of the low energy of the emitted electrons, TEY is the most surface sensitive detection method.[78,79] The experimental setup for XANES depends on whether the transmitted intensity is high (transmission mode) or low (TFY or TEY mode) (Figure 1-11). In transmission mode, the intensity is measured by ion-chamber detectors positioned before the sample (I_o), after the sample (I) and after a reference sample (I_{ref}).[78] The reference is preferably a sample of the element of interest, or of an element whose edge is close to that of the analyte.[78] In TFY or TEY mode, the fluorescence intensity or the total number of electrons is measured, respectively.[78] To prevent interference from stray signals caused by the interaction of incident X-rays and air molecules,

it is important to maintain ultra-high vacuum (>10^{-9} Pa) within the sample chamber. The reference standard is placed in proximity to the sample.

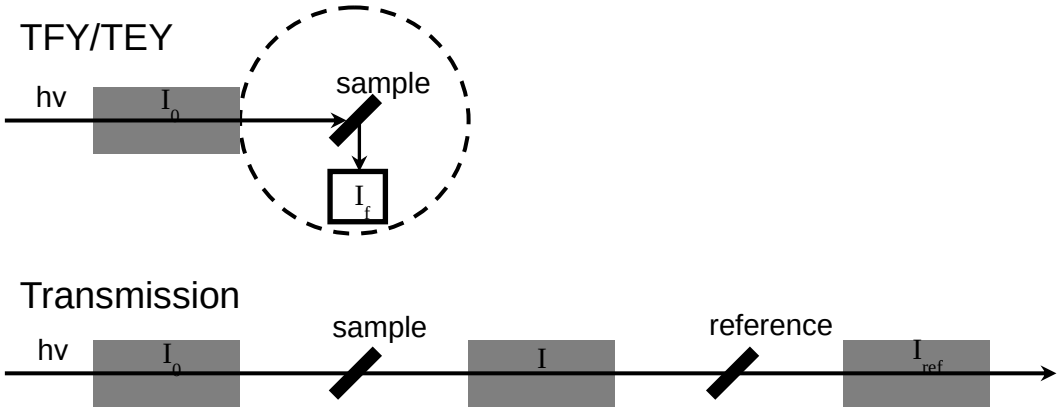

Figure 1-11 Block diagram of an XAS experimental setup.

The XAS spectrum is generated by scanning incident energies selected through various monochromators (e.g., spherical grating monochromator (SGM), variable line spacing plane grating monochromator (VLS-PGM)) and measuring the absorbances.[77] An example is shown in Figure 1-12 highlighting two distinct regions. The sharp increase in absorbance, when core electrons are promoted to empty conduction states above the Fermi level, defines the absorption edge which is in the feature of interest in XANES.[78] These excited electrons can scatter off neighbouring atoms and return to the originating atom, causing a pattern of constructive and destructive interference of electron waves. The oscillating resonance appears in the post-edge region (~10 eV above the edge) and is called the extended X-ray absorption fine-structure (EXAFS).[78] Although not discussed in this thesis, EXAFS is useful for determining local structure.

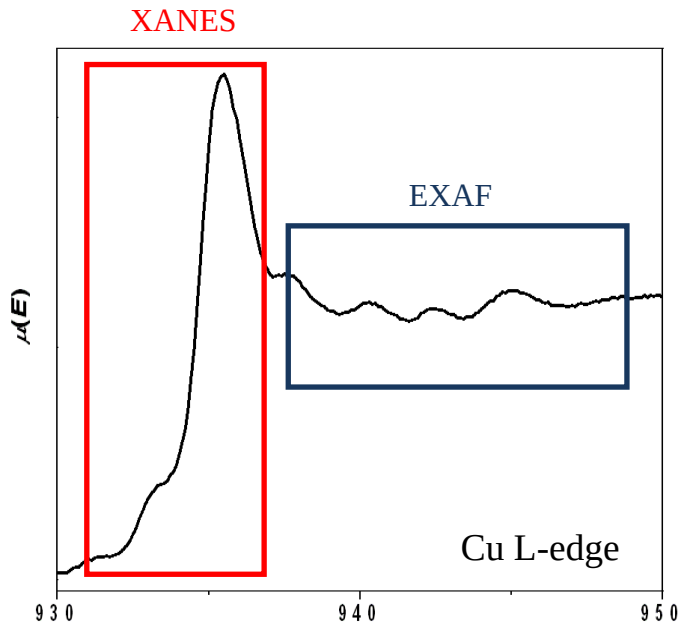

Figure 1-12 Cu L-edge spectrum for LaCuTeO with XANES and EXAFS regions highlighted.

For historical reasons, absorption edges in XAS are identified by an older notation. The originating core electron is identified by a letter representing the principal quantum number and a numerical suffix representing the type of orbital and the spin-state (Table 1-2). Electronic transitions are governed by the dipole selection rule, $\Delta l = \pm 1$.[78] For example, an L_3-edge results from a transition from 2p (l = 1; leaving a $2p_{3/2}$ final state) to both *n*s (l = 0) and *n*d (l = 2) states. Transitions that violate the dipole selection rule, such as quadrupolar transitions ($\Delta l = \pm 2$), can occur when there is mixing of conduction states.[78,80]

Table 1-2 Comparison of XPS and XAS term symbol notations.

XPS notation (nl_j)	XAS notation
$1s_{1/2}$	K
$2s_{1/2}$	L_1
$2p_{1/2}$	L_2
$2p_{3/2}$	L_3
$3s_{1/2}$	M_1
$3p_{1/2}$	M_2
$3p_{3/2}$	M_3
$3d_{3/2}$	M_4
$3d_{5/2}$	M_5

XANES provides information that is similar, as well as complementary, to XPS. First, the absorption energy edge varies with oxidation state. Shifts in absorption energies are often more reliable than XPS binding energy shifts because XANES is less susceptible to final state effects.[78] For example, the binding energies of Cu^0 and Cu^{1+} are identical in XPS,[81,82] but the absorption edges are distinguishable in XANES.[83,84] Second, changes in fine structure in XANES can reveal information about the empty conduction states.[78]

1.5 Band structure calculations

The electronic structure of an extended solid provides useful information to understand structure and bonding and to help interpret features in the XPS and

XANES spectra. Just as for molecules, the electronic structure of solids is obtained by solving the Schrödinger equation:[85,86]

$$H\Psi = E\Psi \qquad \text{(Equation 1-11)}$$

Unlike a molecule, which consists of a finite number of atoms, an extended solid contains an extremely large number of atoms. However, the problem becomes tractable when the solid is crystalline because the potential energy is now a periodic function and the Schrödinger equation becomes:[85,86]

$$(k + V_{r,T})\Psi = E\Psi \qquad \text{(Equation 1-12)}$$

where H is composed of kinetic (k) and potential (V) energy terms. The potential energy is defined for all points r within a unit cell, and is repeated through lattice translations T.[85,86] In a many-electron system, not only are there Coulombic attractions between electrons and nuclei, but there are also electron-electron interactions as expressed through the exchange-correlation potential and the Hartree potential.[85,86] By applying the Kohn-Sham equation, a many-electron system can be approximated to a one-electron system.[85]

Molecular orbitals are conveniently expressed as linear combinations of atomic orbitals which serve as basis functions for solving the Schrödinger equation.[86] Applying symmetry arguments through group theory can simplify the problem considerably. The computational effort to solve the Schrödinger equation increases dramatically with the number of atoms.[85] In an extended solid, the translational symmetry of the crystal is used to simplify the calculation. A Bloch function is a periodic representation of wavefunctions.[85,86] For example, in

a one dimensional crystal, the Bloch function Ψ is expressed as a linear combination of atomic orbitals χ_n:[85,86]

$$\Psi(k) = \sum_{n=1}^{N} e^{ikna} \chi_n \qquad \text{(Equation 1-13)}$$

where *N* is the total number of unit cells, *a* is unit cell repeat length, and *k* is a quantum number in reciprocal space called the *wave vector*. This sum is taken over the reciprocal unit cell repeat, called the Brillouin zone, $-\frac{\pi}{a} \leq k \leq \frac{\pi}{a}$.[85] However, because the function is symmetric about the origin, it suffices to sum over $0 \leq k \leq \frac{\pi}{a}$.[85,86] The wave vector is quantized over very finely spaced intervals (the total number of k points is proportional to the number of unit cells in a macroscopic crystal).[85,86] A band structure is a plot of the energies of these Bloch functions versus *k*. Because the number of *k* points is enormous, only a selected number of *k* points are evaluated during a calculation. The overall quality of the calculation is dictated by the number of *k* points calculated.[85,86]

As an example, the d-band of a chain of transition metal atoms can be constructed by considering combinations of d_{xz} orbitals of each atom. The origin (k = 0) and the boundary (k = $\frac{\pi}{a}$) of the Brillouin zone represent two extremes of such combinations (Figure 1-13). At k = 0, the orbitals are combined in such a way that the nearest-neighbour interactions are antibonding. At k = $\frac{\pi}{a}$, they are combined to lead to all-bonding interactions. Thus the energy decreases on proceeding from k = 0 to k = $\frac{\pi}{a}$, and intervening Bloch functions have intermediate energy. The energy depends on the type of orbitals being combined;

for example, an *s* band would increase in energy from 0 to $\frac{\pi}{a}$. The dispersion, or width, of the band depends on the strength of the interaction.[85,86]

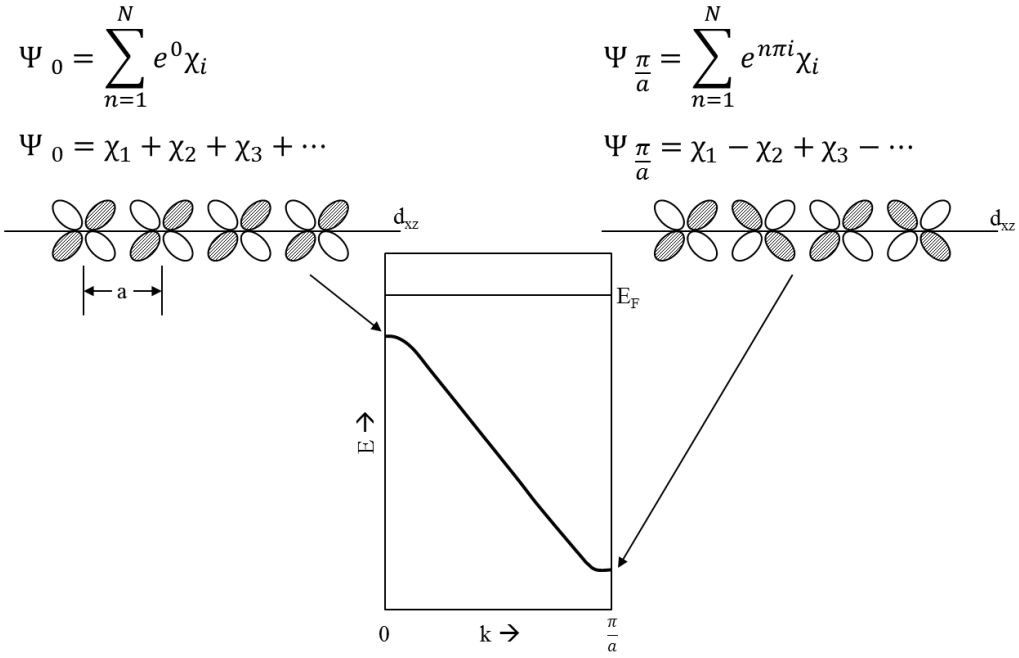

Figure 1-13 Schematic representation of a set of d_{xz} orbitals located on a set of equally spaced transition metal atoms.

The band structures of real 3D crystals are much more complex, of course. Instead of showing bands, it is more convenient to plot the density of states (DOS), which is a measure of the total number of states at a particular energy interval.[86] For a single band, the DOS is inversely proportional to the slope of *E* vs *k*.[86] As part of the computation, the Hamiltonian and overlap matrices are obtained. Analysis of these matrices provides information about bonding interactions in the form of crystal orbital Hamiltonian population (COHP) and crystal orbital overlap population (COOP) curves, respectively.[85,86]

This work makes use of the tight-binding linear muffin-tin orbital (TB-LMTO) program, which operates under the local density and the atomic spheres

approximations.[87] In this program, the potential energy function is simplified by replacing the infinite negative potential energy wells at atom cores by a finite constant potential, much like the shape of a muffin tin. Atoms are modeled as hard spheres with defined radii and the space between each atom is filled with empty spheres to ensure that the potential energy is a continuous function.[85] There are limitations with this method, the most pertinent being the inability to deal with *f*-electrons and the general underestimation of band gap. Whenever possible, other experimental methods should be used to confirm band gap.

1.6 Magnetism

Another way to probe electronic structure is through magnetic measurements. Magnetic properties depend on the presence of unpaired electrons and thus can help identify different valence states. Moreover, in some compounds, the unpaired electrons can align cooperatively to give rise to ferromagnetism which is useful for many applications.

Compounds that contain atoms with unpaired electrons such as rare-earth or transition metals, or both, are likely to exhibit interesting magnetic properties. The unpaired *d*- and *f*- electrons can couple in different ways. There are several fundamental types of magnetic behaviour: diamagnetism, paramagnetism, ferromagnetism, anitferromagnetism, and ferrimagnetism (Figure 1-14).[28,88]

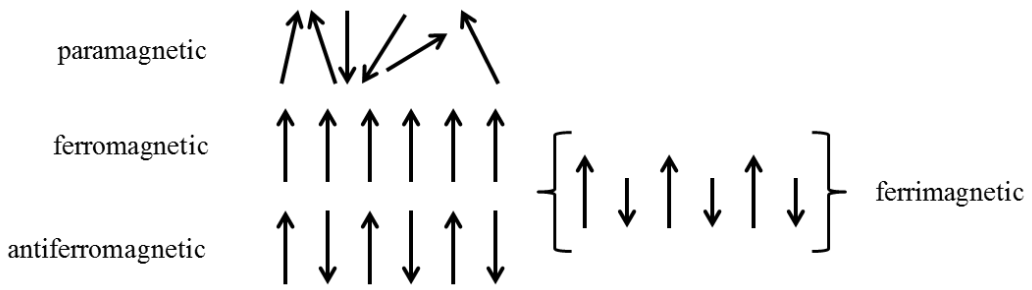

Figure 1-14 Electron alignment in the main types of magnetism.

Magnetic measurements must be made on phase pure samples. They were performed on a Quantum Design Physical Property Measurement System (QD-PPMS), equipped with a 9 T magnet. Usually the samples are in the form of powders and they are accurately weighed out (between 50 and 100 mg). The sample is placed into the chamber of the instrument, the chamber is evacuated, and the sample is centered within the magnetic field. When a sample is subjected to an external magnetic field (*H*), its magnetization (*M*) is measured. The d.c. magnetic susceptibility (χ) is given by:[28,88]

$$\chi = \frac{M}{H} \qquad \text{(Equation 1-14)}$$

Two basic types of measurements are normally made. The temperature dependence of the magnetic susceptibility, χ vs T, can help identify the magnetic behaviour present (Figure 1-15).

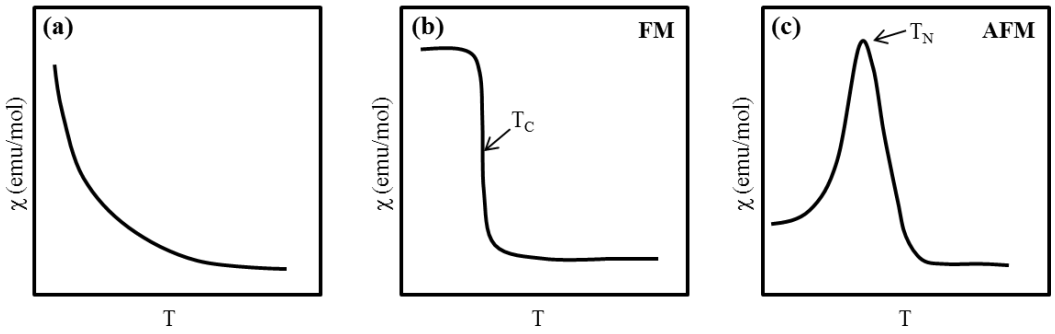

Figure 1-15 Temperature dependent magnetic susceptibility for materials exhibiting (a) paramagnetism (b) ferromagnetism (FM) and (c) antiferromagnetism (AFM).

If a transition is observed in the temperature dependence, it is useful to measure the field-dependence of the magnetization, *M* vs *H*, below this transition. These transitions generally signal the onset of long-range magnetic ordering below the Curie temperature (T_C) in a ferromagnetic sample and the Néel temperature (T_N) in an antiferromagnetic sample.[28,88]

1.6.1 Diamagnetism

Diamagnetic samples contain no unpaired electrons and are repelled by the external magnetic field, giving a small negative magnetic susceptibility that is constant with temperature.[28] Even samples that are not diamagnetic have contributions from the core-electrons that are present in all atoms. These diamagnetic contributions are subtracted in routine measurements. The sample holder itself is diamagnetic and its contribution must also be subtracted.

1.6.2 Paramagnetism

Paramagnetic samples contain unpaired electrons whose spins are randomly oriented until an external magnetic field is applied.[28,88] The magnetic moments act independently of each other. As the temperature decreases, the thermal motion of the electrons decreases and their magnetic moments become increasingly aligned with the magnetic field as expressed by the Curie law:[28,88]

$$\chi = \frac{C}{T} \qquad \text{(Equation 1-15)}$$

where C is the Curie constant (mol/emu·K) and T is temperature (K). It is convenient to plot χ^{-1} vs T, which is linear, to extract the Curie constant from the slope:[28]

$$\chi^{-1} = \left(\frac{1}{C}\right)T \qquad \text{(Equation 1-16)}$$

At a fixed temperature, the magnetization simply increases linearly with field.

In the discussion above, it is assumed that the magnetic moments are localized on atoms. However, magnetic moments can also be carried by the spins of delocalized electrons in the conduction bands of metals giving rise to what is called Pauli paramagnetism (Figure 1-16).[28,88] In the absence of an external field there are equal numbers of spin-up and spin-down conduction electrons filled to the Fermi level.[28,88] When an external field is applied, those electrons with spins aligned parallel to the applied field are lowered in energy, whereas those aligned anti-parallel are raised in energy by the same amount. To equilibrate to the same Fermi level, there has to be a greater population of electrons aligned parallel.[28,88]

This imbalance creates a small concentration of unpaired electrons giving a small, temperature independent magnetic susceptibility.[28,88]

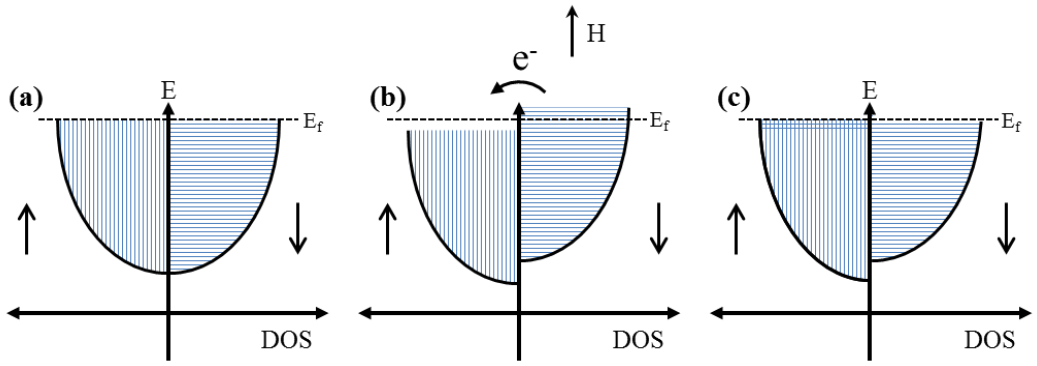

Figure 1-16 Band structure representation of a Pauli paramagnet: (a) conduction band ground state with spin-up (left) and spin down (right) electrons; (b) non-equilibrium state with external magnetic field; (c) equilibrium state.

1.6.3 Cooperative magnetism

Under some circumstances there are strong coupling interactions between magnetic moments that can lead to long-range ordering of spins. This is signaled by observation of non-zero *x*-intercepts in χ^{-1} vs T plots (Figure 1-17):[28,88]

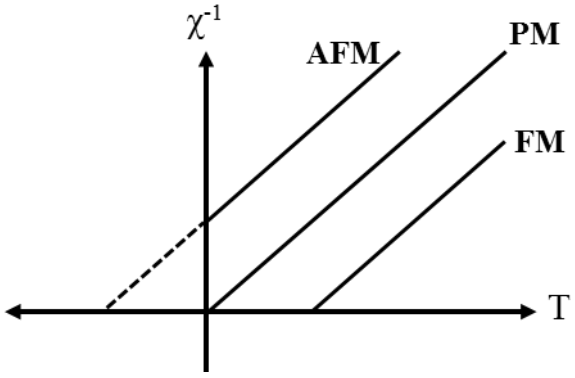

Figure 1-17 Schematic showing typical responses for the three types of magnetism shown in Fig 1-15.

To fit these plots, the Curie law must be modified through the introduction of the Weiss constant (θ) giving the Curie-Weiss law:[28,88]

$$\chi = \frac{C}{T - \theta_p} \qquad \text{(Equation 1-17)}$$

This equation is easily rearranged to:

$$\chi^{-1} = \left(\frac{1}{C}\right) T - \frac{\theta_p}{C} \qquad \text{(Equation 1-18)}$$

The Curie constant is extracted from the slope and the Weiss constant from the intercept. The sign of the Weiss constant indicates the overall coupling interaction. A positive value indicates the presence of ferromagnetic interactions and a negative value indicates antiferromagnetic interactions.[28,88]

In ferromagnetic samples, long-range ordering develops below the transition temperature, in which magnetic moments spontaneously align parallel to each other.[28,88] With no external magnetic field, the magnetic moments are completely aligned within individual domains but these domains are randomly oriented with respect to each other. As the field is increased, domains whose spins are aligned with the field grow at the expense of others until the entire sample is aligned and a saturation magnetization is reached in the *M* vs *H* plot.[28,88] As the field is decreased, the reverse process takes place, but there is often a hysteretic behaviour such that a remanent magnetization is retained, even at zero field. The additional field required to bring the magnetization to zero is called the coercive field.[28,88] Deviations from linearity in the inverse susceptibility plot of ferromagnets can be modeled by the modified Curie-Weiss law:[28,88]

$$\chi - \chi_0 = \frac{C}{T - \theta_p} \qquad \text{(Equation 1-19)}$$

in which a temperature independent term χ_0 is introduced to account for the contribution from conduction electrons.[28,88]

In antiferromagnetic samples, the long-range order of spins below the Néel temperature is antiparallel.[28] Sometimes the spins are canted with respect to each other giving more complicated spin arrangements in which there is still a non-zero magnetic moment overall, mimicking ferromagnetic behaviour.[28,88] Caution has to be exercised because a negative θ value does not necessarily imply long-range antiferromagnetic ordering; more complicated ordering arrangements may be possible.

1.6.4 Analysis of magnetic data

Routine magnetic experiments proceed with field-cooled (FC) and zero-field-cooled (ZFC) measurements of χ vs T. In FC experiments, the magnetic field is first applied and then the magnetization is measured as the temperature is decreased. In ZFC experiments, the sample is first cooled, the magnetic field is applied, and then the magnetization is measured as the temperature is increased. Differences in FC vs ZFC curves can be an indication of important domain effects in ferromagnetic samples. From the fit of the Curie-Weiss law to χ^{-1} vs T, it is easy to extract values for C and θ_p. From the Curie constant, the effective magnetic moment can be evaluated through:[28]

$$\mu_{\text{eff}} = \sqrt{8C} \qquad \text{(Equation 1-20)}$$

The theoretical value for μ_{eff} can be determined as follows:

$$\mu_{eff} = g_J\sqrt{J(J+1)} \qquad \text{(Equation 1-21)}$$

where J is the total angular momentum and g_J is the Landé factor. The addition of the orbital angular momentum L and the spin angular momentum S to give the total angular momentum J has been discussed earlier. According to Hund's rules the ground-state electronic configuration has J = L – S for less than half-filled subshells and J = L + S for more than or exactly half-filled subshells.[28] The Landé factor is also called the gyromagnetic ratio which is the proportionality constant between the magnetic dipole moment and the orbital angular momentum; it measures the magnitude of the splitting of degenerate states in the presence of a weak external magnetic field. In its most rigorous form, the g_J is given by:[28]

$$g_J = g_L\frac{J(J+1) - S(S+1) + L(L+1)}{2J(J+1)} + g_S\frac{J(J+1) + S(S+1) - L(L+1)}{2J(J+1)} \qquad \text{(Equation 1-22)}$$

where g_L and g_S are component magnetic dipoles arising from orbital and spin angular momentum, respectively. For a free electron, g_S has a value of approximately 2, and from the definition of the gyromagnetic ratio g_L is 1. The equation then simplifies to:[28]

$$g_J = \frac{3}{2} + \frac{S(S+1) - L(L+1)}{2J(J+1)} \qquad \text{(Equation 1-23)}$$

For atoms containing f-electrons, this full expression is required. However, for atoms with d-electrons the degeneracy is lifted by crystal-field splitting and the orbital dependence is removed so that J can be replaced by S in this expression, resulting in the spin-only formula:[28]

$$\mu_{\text{eff}} = 2.00\sqrt{S(S+1)} \qquad \text{(Equation 1-24)}$$

For compounds containing more than one magnetic component, the total effective magnetic moment is given by:

$$\mu_{eff} = \sqrt{n_1{\mu_1}^2 + n_2{\mu_2}^2 + n_3{\mu_3}^2 + \cdots} \qquad \text{(Equation 1-25)}$$

where n_k is the stoichiometric ratio of each component. By comparison of calculated and experimental values of μ_{eff}, it is possible to determine which components contribute.[28]

1.7 Electronegativity

The idea of electronegativity is central to many arguments presented in this thesis, especially those involving spectroscopic interpretation. It is important to understand the basic concepts and definitions of electronegativity. Since its original conception by Linus Pauling 80 years ago,[90] electronegativity has undergone many refinements from its original definition as the strength with which a bonded atom attracts surrounding electrons.[91] Some scales are derived from first principles whereas others are based on experiments. The interpretation of shifts in XPS and XANES spectra often make use of arguments involving electronegativity.

1.7.1 Pauling scale

Pauling first defined electronegativity on the basis of experimental bond energies.[90] He noted that the bond energy in heteroatomic molecules A–B (A, B = H, F, Cl, Br, I) was greater than the average in the homoatomic molecules A–A and B–B, and attributed the excess to a stabilizing ionic resonance energy.[90,92]

That is, the wavefunction for the heteratomic molecule A–B is a linear combination of three single-electron wavefunctions:[89]

$$\psi_{tot} = a\psi_{A-B} + b\psi_{A^+-B^-} + c\psi_{A^--B^+} \qquad \text{(Equation 1-26)}$$

where the first term represents the covalent contribution, and the two remaining terms represent ionic contributions assuming different polarities. Depending on the relative contributions of these terms, three different situations can arise (Table 1-3).[89] The coefficient *a* dictates the magnitude of the covalent contribution.

Table 1-3 Relative coefficient scenarios.

Relative electronegativity	Coefficients	Dominant term
A ≈ B	$b = c << a$	ψ_{A-B}
A < B	$b < a << c$	$\psi_{A^+-B^-}$
A > B	$c < a << b$	$\psi_{A^--B^+}$

Pauling defined the electronegativity difference as the square root of ionic resonance energy:

$$\chi_A - \chi_B = (eV)^{-\frac{1}{2}} \sqrt{E_d(AB) - \frac{[E_d(AA + BB)]}{2}} \qquad \text{(Equation 1-27)}$$

where χ is electronegativity, E_d is the experimental bond dissociation energy, and $(eV)^{-1/2}$ is a scaling factor included to make this quantity unitless. The electronegativity was fixed arbitrarily to a value of 4.0.[89,91] Unfortunately not all bond energies are experimentally available, and it is useful to derive electronegativity values from first principles. The problem, of course, is that electronegativity is somewhat ill-defined.

1.7.2 Mulliken-Jaffé scale

The Mulliken scale was originally defined as the arithmetic average of the first ionization energy and the electron affinity of a neutral atom. It was later extended by Jaffé to ions, whose energy follows a parabolic dependence on charge (Figure 1-18).[89] The Mulliken electronegativity for a neutral element is thus the slope of the energy curve as it passes through zero. The advantage of this definition is that it recognizes that electronegativity varies with charge on an atom: a cation is more electronegative and an anion is less electronegative than the parent neutral atom.[89] The electronegativity of an ion is evaluated by the slope of the energy curve at a specified charge. This definition is thus useful in accounting for partial charges. The minimum in the curve corresponds to the most stable charge preferred by a given element.[89] Electronegativity can also vary on the hybridization of the atom in question. For example, atoms with strong s-character in their hybrid orbitals will be more electronegative.[89] While the Mulliken-Jaffé definition brings some insight for molecules, for which classical bonding schemes are generally adequate, it falters in more complicated situations, such as those found in extended solids.

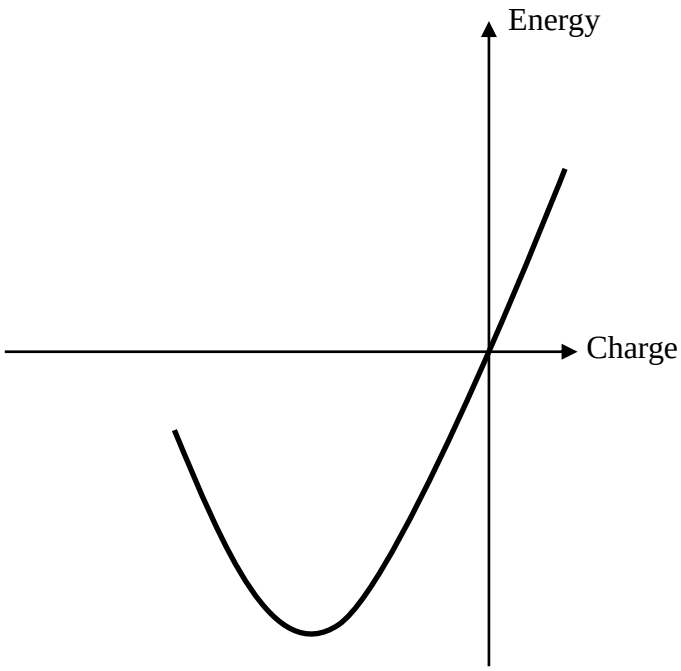

Figure 1-18 Ionization energy-electron affinity energy diagram for an arbitrary element.

1.7.3 Allred-Rochow scale

For the interpretation of X-ray spectra, it is possible to view each excitation event as the removal of an electron from a certain distance away from the nucleus. An appropriate electronegativity scale is thus the one proposed by Allred and Rochow, who viewed the interaction between an electron and the nucleus as a simple electrostatic one governed by Coulomb's law:[93,94]

$$F = \frac{kq_1q_2}{r^2} \qquad \text{(Equation 1-28)}$$

where q_1 and q_2 are point charges, r is the separation between them, and k is the permittivity of the electric field in the associated medium.

The electronegativity is proportional to this electrostatic force but because a valence electron with charge q_1 is screened from the full nuclear charge Z, an

effective nuclear charge Z_{eff} must be introduced to replace q_2. Z_{eff} can be determined through Slater's rules which provide simple estimates for the screening *s* felt by a given electron:[89]

$$Z_{eff} = Z - s \qquad \text{(Equation 1-29)}$$

With the electron-nucleus separation estimated by the covalent radius of the atom r_{cov}, the Allred-Rochow electronegativity is defined as:[93,94]

$$\chi = 3590 \frac{Z_{eff}}{r_{cov}^2} + 0.744 \qquad \text{(Equation 1-30)}$$

where scaling factors are included so that the numerical values match well with those on the Pauling scale.

Because this scale is based entirely on atomic properties, it works well for the analysis of X-ray spectra. However, there are still some drawbacks. It assumes that the electronegativity is independent of the charge on the atom, and that the covalent radius is constant. Of course, atoms in a solid often carry a charge and there are variations in bond lengths in real structures.

1.7.4 Allen scale

A relatively new definition of electronegativity was introduced by Allen, who examined the large set of experimentally determined energy levels found in the NIST database. Because these energies were measured from spectroscopic data, the Allen scale is sometimes referred to as spectroscopic electronegativities. The Allen electronegativity of an atom is defined as:[95]

$$\chi = \frac{n_s \varepsilon_s + n_p \varepsilon_p}{n_s + n_p} \qquad \text{(Equation 1-31)}$$

where n_s and n_p are the number of valence *s* and *p* electrons and ε_s and ε_p are the corresponding one-electron energies, respectively. This method works well when there is no ambiguity about what constitutes the valence electrons as in most main group elements.[95] However, elements with partly filled d- and f- subshells may have ill-defined electronegativities.[95] Moreover, if spectroscopic data are not available, an electronegativity value cannot be evaluated.

1.8 Research motivation

As noted previously, there is a link between the structure of a compound and the properties observed, such as necessarily noncentrosymmetric based piezoelectricity and the existence of MQWs within layered structures leading to interesting optical properties. The versatility of the chalcogenides is attractive as there are many opportunities, especially in quaternary compounds, for elemental substitution which can lead to changes in structure and properties, such as the increased symmetry observed through the incorporation of oxygen. Changes in the electronic structures induced by these aliovalent substitutions are monitored through the application of XPS and XANES, facilitated by theoretical calculations.

The goal of this thesis is to synthesize and characterize quaternary chalcogenides, to examine their crystal and electronic structures, and to gain a greater understanding of how these structures might influence their properties. This is done in two parts. First, it is desirable to synthesize and characterize new noncentrosymmetric rare-earth, transition-metal quaternary chalcogenides to

expand the known body of compounds and to investigate the effect of structural changes on local atomic electronic structure and magnetic properties. A greater understanding of how the structure changes with substitution may allow for the enhancement of the noncentrosymmetry which should enhance any exhibited noncentrosymmetry based properties. Also, the presence of unpaired d- and f-electrons may lead to interesting magnetic properties. Second, the electronic structures of a known series of layered oxychalcogenides are investigated, in an attempt to further understand the complex interplay between interlayer and intralayer interactions. The use of the more electronegative chalcogenides in place of the previously examined pnictides may enhance interactions which were undetectable in the latter. The second half of this thesis also further develops the field of employing XPS and XANES to detect subtle changes in electronic structures.

By developing an understanding of the structures (crystal and electronic) of these quaternary compounds and relating them to observed properties, we intend to lay the groundwork for designing functional solid-state materials that may have important applications in energy conversion technologies.

1.9 References

[1] M.A. Pell, J.A. Ibers, Chem. Ber. 130 (1997) 1–8.

[2] E. Makivicky, Rev. Mineral. Geochem. 61(2006) 7–125.

[3] J. Rouxel, Crystal Chemistry and Properties of Materials with Quasi-one-dimensional Structures, D. Reidel Publishing Company, Dordrecht, Netherlands, 1986.

[4] V.A. Starodub, Russ. Chem. Rev. 68 (1999) 801–820.

[5] F.J. Di Salvo, Science 247 (1990) 649–655.

[6] D. Aldakov, A. Lefrançois, P. Reiss, J. Mater. Chem. C 1 (2013) 3756–3776.

[7] W. Jeitschko, D.J. Braun, Acta. Cryst. B34 (1978) 3196–3201.

[8] S. Rundqvist, Acta. Chem. Scand. 16 (1962) 1-19.

[9] G. Sauthoff, Intermetallics, VCH, Wienheim, 1995.

[10] A.P. Grosvenor, S.D. Wik, R.G. Cavell, A. Mar, Inorg. Chem. 44 (2005) 8988–8996.

[11] A.P. Grosvenor, R.G. Cavell, A. Mar, J. Solid State Chem. 180 (2007) 2702–2712.

[12] A.P. Grosvenor, R.G. Cavell, A. Mar, J. Solid State Chem. 181 (2008) 2549–2558.

[13] P.E.R. Blanchard, A.P. Grosvenor, R.G. Cavell, A. Mar, Chem. Mater. 20 (2008) 7081–7088.

[14] P.E.R. Blanchard, A.P. Grosvenor, R.G. Cavell, A. Mar, J. Mater. Chem. 19 (2009) 6015–6022.

[15] P.E.R. Blanchard, B.R. Slater, R.G. Cavell, A. Mar, Solid State Sci. 12 (2010) 50–58.

[16] P.E.R. Blanchard, R.G. Cavell, A. Mar, J. Solid State Chem. 183 (2010) 1477–1483.

[17] P.E.R. Blanchard, R.G. Cavell, A. Mar, J. Solid State Chem. 183 (2010) 1536–1544.

[18] B.I. Zimmer, W. Jeitschko, J.H. Albering, R. Glaum, M. Reehuis, J. Alloys Compd. 229 (1995) 238–242.

[19] P. Quebe, L.J. Terbüchte, W. Jeitschko, J. Alloys Compd. 302 (2000) 70–74.

[20] Y. Kamihara, H. Hiramatsu, M. Hirano, R. Kawamura, H. Yanagi, T. Kamiya, H. Hosono, J. Am. Chem. Soc. 128 (2006) 10012–10013.

[21] H. Takahashi, K. Igawa, K. Arii, Y. Kamihara, M. Hirano, H. Hosono, Nature 453 (2008) 376–378.

[22] Y.-W. Ma, Z.-S. Gao, L. Wang. Y.-P. Qi, D.-L. Wang, X.-P. Zhang, Chin. Phys. Lett. 26 (2009) 037401-1–037401-4.

[23] Y, Kamihara, M. Hirano, H, Yanagi, T. Kamiya, Y. Saitoh, E. Ikenaga, K. Kobayashi, H. Hosono, Phys. Rev. B 77 (2008) 214515-1–214515-9.

[24] T. Sato, K. Nakayama, Y. Sekiba, T. Arakane, K. Terashima, S. Souma, T. Takahashi, Y. Kamihara, M, Hirano, H. Hosono, J. Phys. Jpn. Suppl. C 77 (2008) 65-68.

[25] P.S. Halasyamani, K.R. Poeppelmeier, Chem. Mater. 10 (1998) 2753–2769.

[26] A.M. Glazer, K. Stadnicka, Acta. Cryst. A45 (1989) 234–238.

[27] M.E. Lines, A.M. Glass, Principles and Applications of Ferroelectrics and Related Materials, Oxford University Press, London, 1977.

[28] C. Kittel, Introduction to Solid State Physics, 8th ed., John Wiley & Sons, Hoboken, 2005.

[29] E.C. Subbarao, Ferroelectrics, 5 (1973) 267–280.

[30] P. Muralt, J. Micromech. Microeng. 10 (2000) 136–146.

[31] B. Jaffe, W. Cook, H. Jaffe, *Piezoelectric Ceramics*, Academic, New York, 1971.

[32] A.J. Moulson, J.M. Herbert, *Electroceramics—Materials, Properties, Applications*, Chapman & Hall, London, 1990.

[33] K.-T. Kim, C.-I. Kim, S.-G. Lee, Microelectron. Eng. 66 (2003) 662–669.

[34] M. Palazzi, C. Carcaly, J. Flahaut, J. Solid State Chem. 35 (1980) 150–155.

[35] S. Inoue, K. Ueda, H. Hosono, N. Hamada, Phys. Rev. B 64 (2001) 245211-1–245211-5.

[36] K. Ueda, K. Takafuji, H. Hiramatsu, H. Ohta, T. Kamiya, M. Hirano, H. Hosono, Chem. Mater. 15 (2003) 3692–3695.

[37] H. Hiramatsu, H. Kamioka, K. Ueda, M. Hirano, H. Hosono, J. Ceram. Soc. Jpn. 113 (2005) 10–16.

[38] H. Hiramatsu, K. Ueda, H. Ohta, T. Kamiya, M. Hirano, H. Hosono, Appl. Phys. Lett. 87 (2005) 211107-1–211107-3.

[39] K. Ueda, H. Hiramatsu, M. Hirano, T. Kamiya, H. Hosono, Thin Solid Films 496 (2006) 8–15.

[40] H. Hiramatsu, H. Kamioka, K. Ueda, H. Ohta, T. Kamiya, M. Hirano, H. Hosono, Phys. Status Solidi A 203 (2006) 2800–2811.

[41] H. Hiramatsu, H. Yanagi, T. Kamiya, K. Ueda, M. Hirano, H. Hosono, Chem. Mater. 20 (2008) 326–334.

[42] H. Hosono, Thin Solid Films 515 (2007) 6000–6014.

[43] J.E. Morris, M.I. Ridge, C.A. Bishop, R.P. Howson, 51 (1980) 1847–1849.

[44] O. Tuna, Y. Selamet, G. Aygun, L. Ozyuzer, J. Phys D: Appl. Phys. 43 (2010) 055402-1–055402-7.

[45] N.D. Arora, J.R. Hauser, D.J. Roulston, IEEE Trans. Electron Devices, ED-29 (1982) 292–295.

[46] H. Kawazoe, M. Yasukawa, H. Hyodo, M. Kurita, H. Yanagi, H. Hosono, Nature, 389 (1997) 939–942.

[47] V.K. Pecharsky, P.Y. Zavalij, Fundamentals of Powder Diffraction and Structural Characterization of Materials, Kluwer Academic Publishers, Boston, 2004.

[48] W. Massa, Crystal Structure Determination, 2nd ed., Springer–Verlag, Berlin, 2004.

[49] H. Rietveld, J. Appl. Crystallogr. 2 (1969) 65–71.

[50] T.J.B. Holland, S.A.T. Redfern, Mineral. Mag. 61 (1997) 65–77.

[51] a) L. Akselrud, Y. Grin, V.K. Pecharski, P.Y. Zavalij, WinCSD, version 08.11, Dresden, Germany, 1993 <http://wincsd.eu/> b) L.G. Akselrud, P.Y. Zavalij, Y.N. Grin, V.K. Pecharski, B. Baumgartner, E. Wölfel, Mat. Sci. Forum 133–136 (1993) 335–340.

[52] L. Smart, E. Moore, Solid State Chemistry: An Introduction, 2nd ed, Chapman & Hall, London, 1996.

[53] A.R. West, Basic Solid State Chemistry, 2nd ed, Wiley, New York, 1999.

[54] G.M. Sheldrick, SHELXTL, version 6.12, Bruker AXS Inc., Madison, WI, 2001.

[55] J.C. Russ, Fundamentals of energy dispersive X-ray analysis, Butterworths, London, 1984.

[56] D. Briggs, M.P. Seah, Practical Surface Analysis Volume 1: Auger and X-ray Photoelectron Spectroscopy, 2nd ed, Wiley, Chichester, 1990.

[57] J.F. Watts, J. Wolstenholme, An Introduction to Surface Analysis by XPS and AES, Wiley, Rexdale, 2003.

[58] J.W. Rabalais, Principles of ultraviolet photoelectron spectroscopy, Wiley, New York, 1977.

[59] S. Tougaard, QUASES-IMFP-TPP2M: Database for Calculation of IMFPs by TPP2M Formula, version 2.1, QUASES-Tougaard Inc, Odense, Denmark, 2000 <www.quases.com>.

[60] C.S. Fadley, Prog. Surf. Sci. 16 (1984) 275–388.

[61] D.A. Shirley, Phys. Rev. B 5 (1972) 4709–4714.

[62] T. Koopmans, Physica 1 (1933) 104–113.

[63] R.P. Vasquez, Surf. Sci. Spectra 5 (1998) 262–266.

[64] R.P. Vasquez, Surf. Sci. Spectra 2 (1993) 144–148.

[65] R.P. Vasquez, Surf. Sci. Spectra 2 (1993) 149–154.

[66] R.P. Gupta, S.K. Sen, Phys. Rev. B 10 (1974) 71–77.

[67] R.P. Gupta, S.K. Sen, Phys Rev. B 12 (1975) 15–19.

[68] A.P. Grosvenor, B.A. Kobe, M.C. Biesinger, N.S. McIntyre, Surf. Interface Anal. 36 (2004) 1564-1574.

[69] N.S. McIntyre, D.G. Zetaruk, Anal. Chem. 49 (1977) 1521–1529.

[70] S.P. Kowalczyk, L. Ley, F.R. McFeely, D.A. Shirley, Phys. Rev. B 11 (1975) 1721–1727.

[71] J.C. Riviere, Surface Analytical Techniques, Oxford University Press, Oxford, 1990.

[72] H. Anno, K. Matsubara, T. Caillat, J.-P. Fleurial, Phys. Rev. B 62 (2000) 10737–10743.

[73] A.J. Signorelli, R.G. Hayes, Phys. Rev. B 8 (1973) 81–86.

[74] G. Crecelius, G.K. Wertheim, D.N.E. Buchanan, Phys. Rev. B 18 (1978) 6519–6524.

[75] S.-J. Oh, G.-H. Kim, G.A. Sawatzky, H.T. Jonkman, Phys. Rev. B 37 (1988) 6145–6152.

[76] T.K. Sham, M.L. Rivers, Rev. Miner. Geochem. 49 (2002) 117–147.

[77] H. Winnick, Synchrotron Radiation Sources – A Primer, World Scientific Publishing, London, 1994.

[78] M. Newville, Fundamentals in XAFS, Consortium for Advanced Radiation Sources, University of Chicago, Chicago, 2004.

[79] S.L.M. Schroeder, G.D. Moggridge, T. Rayment, R.M. Lambert, J. Mol. Catal. A: Chem. 119 (1997) 357-365.

[80] T. Yamamoto, X-ray Spectrom. 37 (2008) 572–584.

[81] S.K. Chawla, N. Sankarraman, J.H. Payer, J. Electron Spectrosc. Relat. Phenom. 61 (1992) 1–18.

[82] A.C. Miller, G.W. Simmons, Surf. Sci. Spectra 2 (1993) 55–60.

[83] G. Cressey, C.M.B. Henderson, G. van der Laan, Phys. Chem. Minerals 20 (1993) 111–119.

[84] R.A.D. Pattrick, G. van der Laan, J.M. Charnock, B.A. Grguric, Am. Mineral. 89 (2004) 541–546.

[85] R. Dronskowski, Computational Chemistry of Solid State Materials, Wiley-VCH, Weinheim, 2005.

[86] R. Hoffman, Angew. Chem. Int. Ed. Engl. 26 (1987) 846–878.

[87] R. Tank, O. Jepsen, A. Burkhardt, O.K. Andersen, TB-LMTO-ASA Program, Version 4.7, Max Planck Institut für Festkörperforschung, Stuttgart, Germany, 1998.

[88] D.H. Martin, Magnetism in Solids, M.I.T. Press, Cambridge, 1967.

[89] J.E. Huheey, E.A. Keiter, R.L. Keiter, Inorganic Chemistry: Principles of Structure and Reactivity, 4th ed., HarperCollins College Publishers, New York, 1993.

[90] L. Pauling, J. Am. Chem. Soc. 54 (1932) 3570–3582

[91] L. Pauling, The Nature of the Chemical Bond, 3rd ed., Cornell University Press, Ithaca, New York, 1960.

[92] R.G. Pearson, J. Chem. Phys. 17 (1949) 969–971.

[93] A.L. Allred, E.G. Rochow, J. Inorg. Nucl. Chem. 5 (1958) 264–268.

[94] A.L. Allred, J. Inorg. Nucl. Chem. 17 (1961) 215–221.

[95] L.C. Allen, J. Am. Chem. Soc. 111 (1989) 9003–9014.

Chapter 2

Rare-earth transition-metal indium sulphides RE_3FeInS_7 (*RE* = La–Pr), RE_3CoInS_7 (*RE* = La, Ce), and La_3NiInS_7[1]

2.1 Introduction

First discovered by Flahaut and co-workers nearly 50 years ago,[1–4] the quaternary rare-earth chalcogenides $RE_3MM'Ch_7$ (*Ch* = S, Se) are known for many combinations of *M* and *M*′, the most prevalent being monovalent and tetravalent elements (*M* = Cu, Ag; *M*′ = Si, Ge, Sn).[1–24] Other combinations are possible as long as the valences of *M* and *M*′ sum to five,[3,4,25–28] or if they do not, vacancies are introduced.[29–31] These compounds adopt related noncentrosymmetric structures (space group $P6_3$) which may be described as the La_3CuSiS_7-type structure if *M* resides in a trigonal planar site,[1–4] or an ordered derivative of the ternary $Ce_3Al_{1.67}S_7$-type structure if *M* resides in an octahedral site.[32–35] They have been identified as attractive candidates for several materials applications, given the lack of an inversion centre in the structure, the presence of *f*-electrons imparted by the *RE* component, and the flexible coordination geometry of the *M* site. Ferroelectric behaviour has been predicted for these compounds, with Curie temperatures as high as 1000 K for La_3MnGaS_7,[36] although no

[1] *A version of this chapter has been published. B.W Rudyk, S.S. Stoyko, A. Mar, J. Solid State Chem. 208 (2013) 78-85. Copyright (2013) by Elsevier.*

measurements have been forthcoming. Non-linear optical properties initially measured for $La_3CuGeSe_7$ and $La_3Mg_{0.5}SiS_7$ were unimpressive,[8,29] but they were dramatically improved in $Y_3Zn_{0.5}SiS_7$ and related compounds.[31] Ionic conductivity may be likely in Ag-containing derivatives such as $La_3Ag_{0.82}SnS_7$ and $Ce_3Ag_{0.63}SiS_{6.63}Cl_{0.37}$.[37,38] The optical luminescence of Tb_3CaGaS_7 and the magnetic susceptibility of some $RE_3MM'S_7$ (M = transition metals; M' = Al, Ga, Fe) compounds have been measured.[25,26,28] The latter compounds represent some of the limited examples known in which M is a divalent and M' is a trivalent element.

Reported here is the elucidation of the quaternary rare-earth sulphides RE_3MInS_7 (M = Fe, Co, Ni), which are the first representatives of chalcogenides $RE_3MM'Ch_7$ containing In atoms as the M' component. Their crystal structures have been determined by X-ray diffraction (XRD) methods, and their electronic structures have been investigated by X-ray photoelectron spectroscopy (XPS) and magnetic measurements. The bonding in these compounds has been further evaluated through band structure calculations.

2.2 Experimental

2.2.1 Synthesis

Starting materials were freshly filed *RE* pieces (*RE* = La–Pr, 99.9%, Hefa), Fe powder (99.9%, Cerac), Co powder (99.8%, Cerac), Ni powder (99.9%, Cerac), In shot (99.999%, Cerac), and S flakes (99.998%, Sigma-Aldrich). Stoichiometric mixtures in a total mass of 0.200 g were pressed into pellets (6 mm

diameter, 1–3 mm thickness) and placed within fused-silica tubes which were evacuated and sealed. The tubes were heated to 1050 °C, kept there for 96 h, heated to 1150 °C, and cooled to room temperature over 2–3 d. Powder X-ray diffraction (XRD) patterns were collected with Cu $K\alpha_1$ radiation on an Inel diffractometer equipped with a curved position-sensitive detector (CPS 120). They revealed that La_3FeInS_7, La_3CoInS_7, and La_3NiInS_7 were formed nearly quantitatively, about 95–99% of the product (Figure 2-1), whereas Ce_3FeInS_7, Pr_3FeInS_7, and Ce_3CoInS_7 were formed with 7–17% admixtures of other phases (generally various forms of RE_2S_3) (not shown). Attempts to extend the *RE* substitution (up to Tb) beyond the title compounds were unsuccessful. Small single crystals were available for all samples except Ce_3CoInS_7, for which the cell parameters were refined from the powder XRD pattern (Figure A1-1 in Appendix 1) to be a = 9.9977(2) Å, c = 6.2534(2) Å, and V = 541.31(2) Å^3. Energy-dispersive X-ray (EDX) analysis on these crystals was performed on a JEOL JSM-6010LA scanning electron microscope. Multiple points on multiple crystals for each compound were analyzed. The chemical composition was similar in all compounds. The average chemical composition (28(2)% *RE*, 7(2)% *M*, 10(2)% In, 55(2)% S) over all compounds analyzed is in reasonable agreement with expectations (25% *RE*, 8% *M*, 8% In, 58% S).

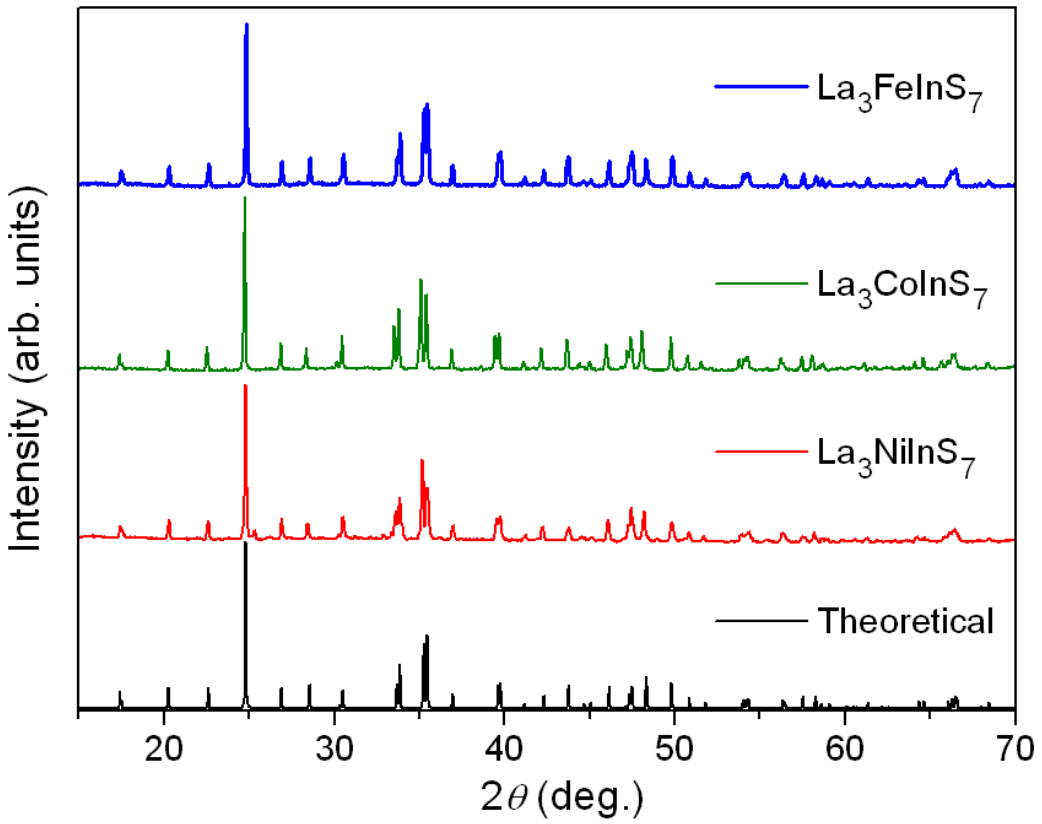

Figure 2-1 Powder XRD patterns for La_3MInS_7 (*M* = Fe, Co, Ni). The theoretical pattern for La_3FeInS_7 is shown at the bottom.

2.2.2 Structure determination

Intensity data were collected at 173 K on a Bruker PLATFORM diffractometer equipped with a SMART APEX II CCD area detector and a graphite-monochromated Mo *K*α radiation source, using ω scans at 4–6 different ϕ angles with a frame width of 0.3° and an exposure time of 12 s per frame. Face-indexed absorption corrections were applied. Structure solution and refinement were carried out with use of the SHELXTL (version 6.12) program package.[39] The noncentrosymmetric space group $P6_3$ was chosen upon recognition from the powder XRD patterns that these compounds belong to the family of hexagonal

chalcogenides $RE_3MM'Ch_7$.[1–4] Initial atomic positions were located by direct methods. Refinements proceeded in a straightforward manner, with the displacement parameters being well-behaved and providing no evidence for partial occupancy or disorder between *M* and In atoms. Within this polar space group, the *z*-coordinate of the *M* atom was restrained to be at the origin. Of the five crystals examined here, four had the same absolute configuration and one (La_3CoInS_7) had the opposite configuration; no inversion twinning was observed, as indicated by the Flack parameter, which refined to values of 0.02(2)–0.04(2). Atomic positions were standardized with the program STRUCTURE TIDY (while ensuring that the absolute configuration was retained).[40] Table 2-1 lists crystal data and details of the data collection, Table 2-2 lists positional and displacement parameters, and Table 2-3 lists selected interatomic distances. Further data, in CIF format, have been sent to Fachinformationszentrum Karlsruhe, Abt. PROKA, 76344 Eggenstein-Leopoldshafen, Germany, as supplementary material No. CSD-426492 to 426496 and can be obtained by contacting FIZ (quoting the article details and the corresponding CSD numbers).

2.2.3 XPS Analysis

XPS spectra for La_3MInS_7 (*M* = Fe, Co, Ni) were collected on a Kratos AXIS 165 spectrometer equipped with a monochromatic Al *K*α radiation source and a hybrid lens with a spot size of 700 μm × 400 μm. The spectrometer was operated at 15 mA and 14 kV. The samples were ground, pressed onto In foil, mounted on a copper holder with carbon tape, and transferred in a sealed

container to the analysis chamber, which was maintained at a pressure between 10^{-7} and 10^{-9} Pa. To remove surface oxides, the samples were sputter-cleaned with an Ar^{+} beam (4 kV, 10 mA) until no further changes were observed in the intensities of the O 1s peak and other shoulders associated with oxides. Binding energies (BE) were the same before and after this sputtering procedure.

Survey spectra from 1100 to 0 eV were collected with a pass energy of 160 eV, a step size of 0.7 eV, and a sweep time of 180 s. These spectra confirmed the presence of all expected elements. The In foil used in the sample mounting interfered with the In signal belonging to the sample itself, precluding accurate quantitative analysis. However, it was still possible to identify the position of the In peak intrinsic to the sample. High-resolution La 3d, *M* 2p, In 3d, and S 2p core-line spectra were collected with a pass energy of 20 eV, a step size of 0.05 eV, and a sweep time of 180 s, with appropriate BE ranges as determined from the survey spectra. The Ni 2p core line peaks are concealed within the La 3d peaks. Charge neutralization was applied, with the settings on the charge balance (1.8–3.6 eV) and filament current (1.6–2.0 A) adjusted on a case-by-case basis to give the sharpest, most intense peaks. The spectra were calibrated to the C 1s line at 284.8 eV which arises from adventitious carbon. All spectra were analyzed with use of the CasaXPS software package.[41] The background arising from energy loss was removed by applying a Shirley-type function and the peaks were fitted to pseudo-Voigt (70% Gaussian and 30% Lorentzian) line profiles to take into account spectrometer and lifetime broadening effects. On the basis of many

previous measurements made on this instrument, we estimate a precision of better than ±0.1 eV in the BEs.

Special attention was paid to the Fe 2p spectra of La_3FeInS_7, which exhibited complex fine structure. To enhance the intensity, the Fe 2p spectra were re-collected with a larger pass energy of 40 eV, without degrading the spectral features. Further, these measurements were repeated on additional freshly prepared samples of La_3FeInS_7, handled within an inert atmosphere at all times to minimize surface oxidation. Sputtering over different durations did not affect the lineshape of the Fe 2p core-line peak, indicating that these features are intrinsic to the sample.

Table 2-1 Crystallographic data for RE_3FeInS_7, La_3CoInS_7, and La_3NiInS_7.

Formula	La_3FeInS_7	Ce_3FeInS_7	Pr_3FeInS_7	La_3CoInS_7	La_3NiInS_7
Formula mass (amu)	811.82	815.45	817.82	814.90	814.68
Space group	$P6_3$ (No. 173)	$P6_3$ (No. 173)	$P6_3$ (No. 173)	$P6_3$ (No. 173)	$P6_3$ (No. 173)
a (Å)	10.1276(5)	10.0280(8)	9.9510(5)	10.1307(6)	10.1470(12)
c (Å)	6.2864(3)	6.2720(5)	6.2593(3)	6.2762(4)	6.2827(7)
V (Å^3)	558.40(5)	546.22(8)	536.77(5)	557.84(6)	560.21(11)
Z	2	2	2	2	2
ρ_{calcd} (g cm^{-3})	4.828	4.958	5.060	4.852	4.830
T (K)	173	173	173	173	173
Crystal dimensions (mm)	0.13 × 0.04 × 0.03	0.17 × 0.08 × 0.06	0.08 × 0.06 × 0.03	0.13 × 0.05 × 0.04	0.11 × 0.11 × 0.06
Radiation	Graphite monochromated Mo $K\alpha$, λ = 0.71073 Å				
μ(Mo $K\alpha$) (mm^{-1})	15.78	16.90	18.09	15.98	16.11
Transmission factors	0.400–0.708	0.241–0.597	0.350–0.660	0.282–0.668	0.344–0.530
2θ limits	4.64–66.46°	4.70–66.32°	4.72–66.46°	4.64–66.50°	4.64–66.42°

Data collected	$-15 \le h \le 15$, $-15 \le k \le 15$, $-9 \le l \le 9$	$-14 \le h \le 15$, $-15 \le k \le 15$, $-9 \le l \le 9$	$-15 \le h \le 15$, $-15 \le k \le 15$, $-9 \le l \le 9$	$-15 \le h \le 15$, $-15 \le k \le 15$, $-9 \le l \le 9$	$-15 \le h \le 15$, $-15 \le k \le 15$, $-9 \le l \le 9$
No. of data collected	7843	7485	7636	7728	7709
No. of unique data, including $F_o^2 < 0$	1422 (R_{int} = 0.032)	1376 (R_{int} = 0.024)	1359 (R_{int} = 0.032)	1423 (R_{int} = 0.033)	1416 (R_{int} = 0.026)
No. of unique data, with $F_o^2 > 2\sigma(F_o^2)$	1369	1353	1291	1369	1397
No. of variables	39	39	39	39	39
Flack parameter	0.02(2)	0.02(1)	0.02(2)	0.02(2)	0.04(2)
$R(F)$ for $F_o^2 > 2\sigma(F_o^2)$ [a]	0.016	0.014	0.016	0.017	0.015
$R_w(F_o^2)$ [b]	0.035	0.033	0.035	0.033	0.035
Goodness of fit	1.05	1.11	1.07	1.07	1.08
$(\Delta\rho)_{max}$, $(\Delta\rho)_{min}$ (e Å^{-3})	1.26, –0.73	1.46, –0.98	0.93, –1.11	1.26, –0.78	1.31, –0.69

[a] $R(F) = \sum||F_o| - |F_c|| / \sum|F_o|$ for $F_o^2 > 2\sigma(F_o^2)$.

[b] $R_w(F_o^2) = [\sum[w(F_o^2 - F_c^2)^2] / \sum wF_o^4]^{1/2}$; $w^{-1} = [\sigma^2(F_o^2) + (Ap)^2 + Bp]$, where $p = [\max(F_o^2,0) + 2F_c^2] / 3$.

Table 2-2 Positional and equivalent isotropic displacement parameters (Å^2) [a] for RE_3FeInS_7, La_3CoInS_7, and La_3NiInS_7.

	La_3FeInS_7	Ce_3FeInS_7	Pr_3FeInS_7	La_3CoInS_7	La_3NiInS_7
RE in 6*c* (*x*, *y*, *z*)					
x	0.37425(2)	0.37424(2)	0.37476(2)	0.37411(2)	0.37419(2)
y	0.22310(2)	0.22294(2)	0.22231(2)	0.22329(2)	0.22442(2)
z	0.19620(4)	0.19318(4)	0.19167(5)	0.30231(4)	0.19780(4)
U_{eq}	0.00871(5)	0.00868(5)	0.00851(5)	0.00899(5)	0.01026(5)
M in 2*a* (0, 0, *z*)					
z	0.00000(13)	0.00000(12)	0.00000(15)	0.00000(12)	0.00000(13)
U_{eq}	0.00976(16)	0.00964(15)	0.00936(18)	0.00897(16)	0.01085(17)
In in 2*b* (1/3, 2/3, *z*)					
z	0.12295(6)	0.12123(6)	0.11963(7)	0.37545(6)	0.12452(6)
U_{eq}	0.00937(8)	0.00989(8)	0.01085(9)	0.00942(8)	0.01023(8)

S1 in 6*c* (*x*, *y*, *z*)					
x	0.09607(8)	0.09718(8)	0.09867(10)	0.09572(9)	0.09695(9)
y	0.23150(9)	0.23309(8)	0.23465(10)	0.23104(10)	0.23509(11)
z	0.25998(14)	0.25986(13)	0.26021(16)	0.23727(15)	0.25943(17)
U_{eq}	0.00923(14)	0.00896(13)	0.00905(15)	0.01140(15)	0.01773(18)
S2 in 6*c* (*x*, *y*, *z*)					
x	0.51546(9)	0.51499(9)	0.51508(10)	0.51508(9)	0.51473(9)
y	0.08166(9)	0.08069(9)	0.08004(11)	0.08174(10)	0.08217(9)
z	0.45896(13)	0.45427(12)	0.45215(14)	0.03941(13)	0.45972(13)
U_{eq}	0.00932(14)	0.00915(13)	0.00941(16)	0.00956(15)	0.01076(14)
S3 in 2*b* (1/3, 2/3, *z*)					
z	0.5020(2)	0.5007(2)	0.4984(2)	0.9959(2)	0.5042(2)
U_{eq}	0.0080(2)	0.0086(2)	0.0088(3)	0.0079(2)	0.0089(2)

[a] U_{eq} is defined as one-third of the trace of the orthogonalized U_{ij} tensor.

Table 2-3 Selected interatomic distances (Å) in RE_3FeInS_7, La_3CoInS_7, and La_3NiInS_7.

	La_3FeInS_7	Ce_3FeInS_7	Pr_3FeInS_7	La_3CoInS_7	La_3NiInS_7
RE–S3	2.8636(4)	2.8348(6)	2.8128(7)	2.8634(6)	2.8684(7)
RE–S1	2.8888(8)	2.8614(7)	2.8434(9)	2.8893(8)	2.8948(9)
RE–S2	2.8933(8)	2.8686(8)	2.8502(9)	2.8952(9)	2.8928(9)
RE–S1	2.9395(8)	2.9189(7)	2.9056(9)	2.9402(8)	2.9514(9)
RE–S2	2.9789(8)	2.9533(8)	2.9307(9)	2.9777(9)	2.9804(9)
RE–S1	3.0191(9)	2.9860(9)	2.9627(10)	3.0093(10)	3.0181(11)
RE–S2	3.0935(8)	3.0694(8)	3.0573(9)	3.0885(9)	3.0856(9)
M–S1 (×3)	2.5375(9)	2.5306(9)	2.5252(11)	2.5232(10)	2.5683(12)
M–S1 (×3)	2.6141(9)	2.6061(9)	2.6031(11)	2.6207(10)	2.6397(11)
In–S3	2.3832(14)	2.3798(13)	2.3710(16)	2.3822(14)	2.3856(14)
In–S2 (×3)	2.4497(8)	2.4444(8)	2.4342(9)	2.4494(9)	2.4525(9)

2.2.4 Band structure calculations

Tight-binding linear muffin tin orbital band structure calculations were performed on La_3MInS_7 (M = Fe, Co, Ni) within the local density and atomic spheres approximation with use of the Stuttgart TB-LMTO-ASA program (version 4.7).[42] The basis set consisted of La 6s/6p/5d/4f, M 4s/4p/3d, In 5s/5p/5d/4f, and S 3s/3p/3d orbitals, with the La 6p, In 5d/4f, and S 3d orbitals being downfolded. Integrations in reciprocal space were carried out with an improved tetrahedron method over 208 irreducible k points within the first Brillouin zone.

2.2.5 Magnetic susceptibility measurements

Measurements of dc magnetic susceptibility were made on La_3MInS_7 (M = Fe, Co, Ni) between 2 and 300 K under an applied field of 0.5 T on a Quantum Design 9T-PPMS magnetometer. Susceptibility values were corrected for contributions from the holder and sample diamagnetism.

2.3 Results and discussion

2.3.1 Structure

The six quaternary sulphides RE_3MInS_7 prepared here fall into three series in which the extent of RE substitution becomes narrower on proceeding from RE_3FeInS_7 (RE = La, Ce, Pr) to RE_3CoInS_7 (RE = La, Ce) to RE_3NiInS_7 (RE = La). These compounds crystallize in the noncentrosymmetric hexagonal space group $P6_3$ adopted by other quaternary chalcogenides $RE_3MM'Ch_7$ (Ch = S, Se).[1-4]

Such chalcogenides can be divided according to the valences of *M* and *M*′: I-IV combinations (*M* = Cu, Ag; *M*′ = Si, Ge, Sn) constitute the vast majority of representatives,[1–24] whereas II-III (*M* = Mg and divalent transition metals; *M*′ = Al, Ga)[3,4,25–28] and III-II combinations (*M* = Ti, V, Cr, Sb, Bi, Sc, Yb, Lu, In; *M*′ = Be)[3,4] are much rarer. The title compounds are the first examples of II-III combinations in which the *M*′ site contains In atoms. The elegant structure of these compounds is easy to visualize (Figure 2-2). The *M* atoms reside at centres of octahedra, which form confacial chains extending along the 6_3 screw axes parallel to the *c*-direction. This octahedral coordination geometry is more properly described as trigonal antiprismatic; it contrasts with the much more common trigonal planar geometry observed in the I-IV combinations whereby Cu or Ag atoms are displaced towards the triangular base of the antiprism to attain CN3.[1–24] The *M*′ atoms reside at centres of tetrahedra, which all point in the same orientation as they stack along the threefold rotation axes parallel to the *c*-direction; equivalently, this arrangement is sometimes described as chains of corner-sharing trigonal bipyramids (pairs of opposite-pointing tetrahedra) with the *M*′ site being considerably displaced from the centre.[34] The *RE* atoms lying in the intervening spaces between these two chains are seven-coordinate, within monocapped trigonal prisms. In the strictest sense, the designation of "La_3CuSiS_7-type" should be restricted to those structures in which the *M* site is trigonal planar, which correspond to the I–IV combinations of the $RE_3MM'Ch_7$ family. When the *M* site is octahedral, as is the case here and for other II–III as well as III–II combinations, the more accurate description is an ordered derivative

of the ternary $Ce_3Al_{1.67}S_7$-type structure.[32–35] Despite this difference, both structures are often collectively referred to as "La_3CuSiS_7-type" in the literature.

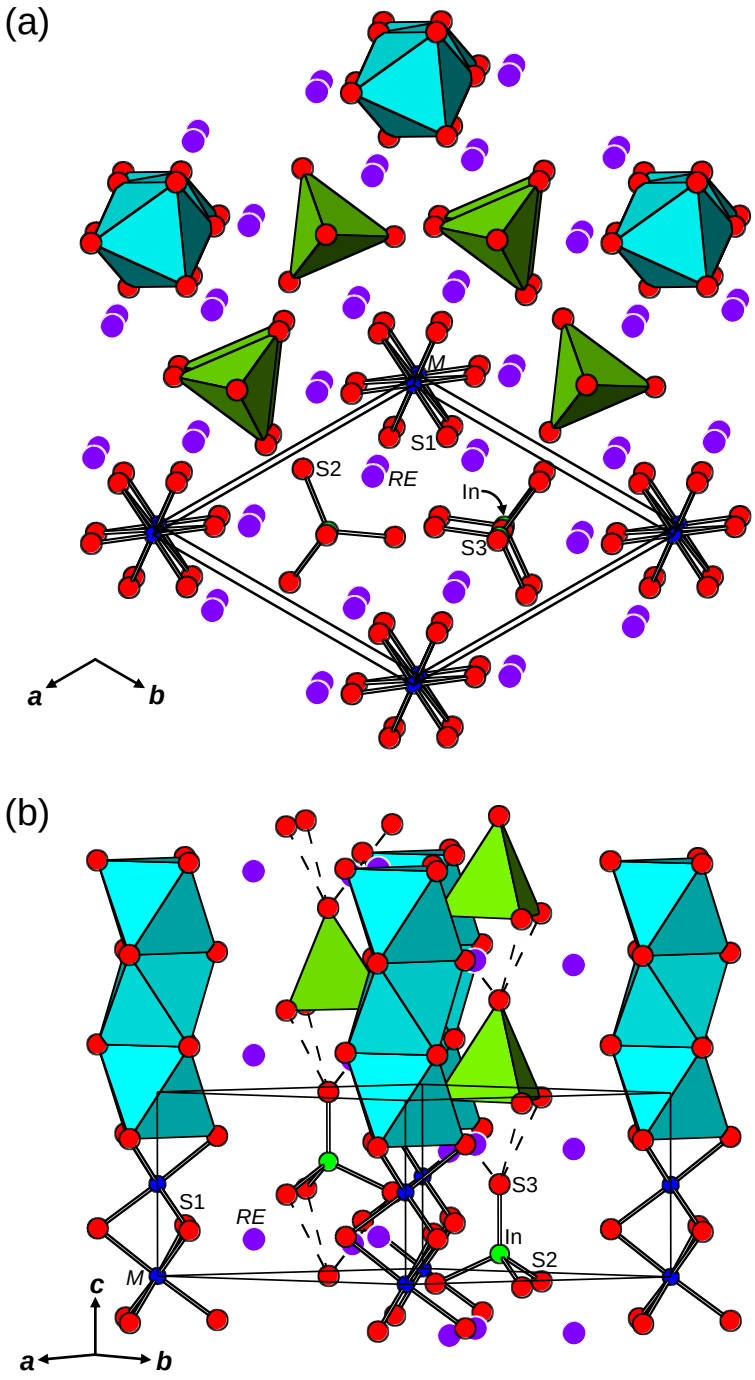

Figure 2-2 Structure of $RE_3M\mathrm{InS}_7$ (M = Fe, Co, Ni) viewed (a) along and (b) perpendicular to the c-direction. The M-centred octahedra and the In-centred tetrahedra are highlighted.

Many of the crystal chemical principles guiding the stability of La_3CuSiS_7-type structures were first enunciated by Flahaut and co-workers,[4] and it is interesting to see how they apply to these RE_3MInS$_7$ compounds. The coordination of the *RE* site can be considered to be [7+1]; the eventual occurrence of the eighth *RE*–*Ch* interaction, which extends nearly parallel to the *c*-direction, depends on the *c*/*a* ratio. In RE_3MInS$_7$, the seven shortest *RE*–S distances lie in the range of 2.8–3.1 Å, but the eighth distance is far too long (>3.7 Å) to be significant. The lowering of the CN from 8 to 7 is consistent with observed *c*/*a* ratios in these compounds (0.62–0.63), which are among the highest observed so far in any $RE_3MM'Ch_7$ compounds (typically 0.57–0.61). The substitution of *RE* or *M* atoms within a given series also results in clear trends in the cell parameters (Figure 2-3). Progressing to a smaller *RE* component in RE_3FeInS$_7$ strongly contracts the *a*-parameter but barely changes the *c*-parameter, implying that bonding within the hexagonal *ab*-plane (i.e., between the chains of octahedra and tetrahedra) is provided largely by the *RE* atoms. Progressing to a later transition-metal component in La_3MInS$_7$ results in smaller changes in both the *a*- and *c*-parameters. In fact, the *M*–S distances within the *M*-centred octahedra tend to increase slightly, from 2.54–2.61 Å in La_3FeInS$_7$ to 2.57–2.64 in La_3NiInS$_7$; the trend runs counter to the size of *M* atoms, suggesting that electronic effects may also be at play. Notwithstanding the face-sharing of these octahedra, the *M*–*M* distances exceed 3.1 Å and are probably too long to be bonding. The *c*-parameter is essentially controlled by the choice of the *M*′ component occupying the tetrahedral sites; here, the large In atoms are responsible for the large *c*/*a* ratios

noted above. The In–S distances are practically invariant (2.37–2.45 Å) among all members of this $RE_3M\text{InS}_7$ series. The expanded structure of this In-containing series $RE_3M\text{InS}_7$ implies that only the largest *RE* components (La–Pr) are compatible, whereas various Ga-containing series $RE_3M\text{GaS}_7$ can be extended to smaller *RE* components (up to Dy).[3,26,28]

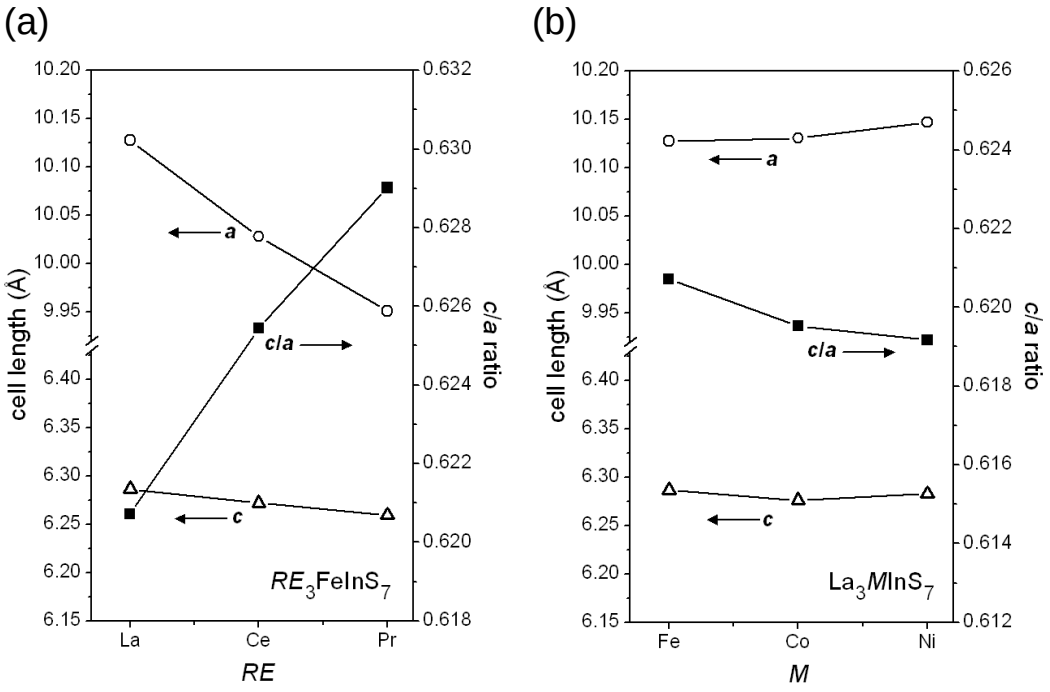

Figure 2-3 Plots of cell parameters and *c*/*a* ratios for (a) $RE_3\text{FeInS}_7$ and (b) La_3MInS_7.

2.3.2 XPS Analysis

Implicit in the discussion above is that the transition-metal atoms are divalent and the indium atoms are trivalent. This assignment is consistent with the observation that the higher-valent element generally prefers the tetrahedral site in $RE_3MM'Ch_7$ compounds.[4] The valences can be further assessed through bond valence sums evaluated from the observed interatomic distances.[43] In $\text{La}_3\text{FeInS}_7$,

the valences calculated in this manner are 2.0 for the Fe atoms and 3.3 for the In atoms. A similar calculation for La_3NiInS_7 leads to valences of 1.3 for the Ni atoms and 3.3 for the In atoms; this result seems to suggest significant underbonding around the Ni atoms, unless other factors, such as metal-metal bonding, may be at play. In any case, the crystal structure refinements support the observed site preference, which can be definitively ascertained given the pronounced difference in X-ray scattering between the first-row transition metal (Fe, Co, Ni) and indium atoms.

To obtain further information about the electronic structure of these compounds, XPS spectra have been analyzed for the La_3MInS_7 series (*M* = Fe, Co, Ni). To our knowledge, these are the first such spectroscopic measurements made on any $RE_3MM'Ch_7$ compounds. The La 3d, Fe and Co 2p, In 3d, and S 2p core-line XPS spectra are shown in Figures 2-4 and 2-5, and the measured BEs are listed in Table 2-4.

The La 3d spectra are similar for all three compounds, with the La $3d_{5/2}$ BE (833.6–833.8 eV) being higher than in La_2O_3 (831.9 eV)[44] (Figure 2.4a). However, these BEs are not reliable measures of oxidation states because spectra of *RE* atoms are strongly influenced by final state effects, which are also responsible for the prominent satellite peaks. As has been previously observed in the spectra of other La-containing compounds,[44–47] these satellite peaks are believed to arise from a ligand-to-metal shake-up process whereby some of the kinetic energy (KE) of the ejected photoelectron is expended to promote electrons in the valence states of the ligands (here, S atoms) to the empty La-based

conduction states. This loss in KE results in satellite peaks, which are found at higher BE (by ~4 eV) to the core-line peaks and are commonly diagnostic of La^{3+} species.[45–50] The relative intensity of these satellite peaks does not vary in the La_3MInS_7 series because the La environment remains essentially unchanged (Table 2-3).

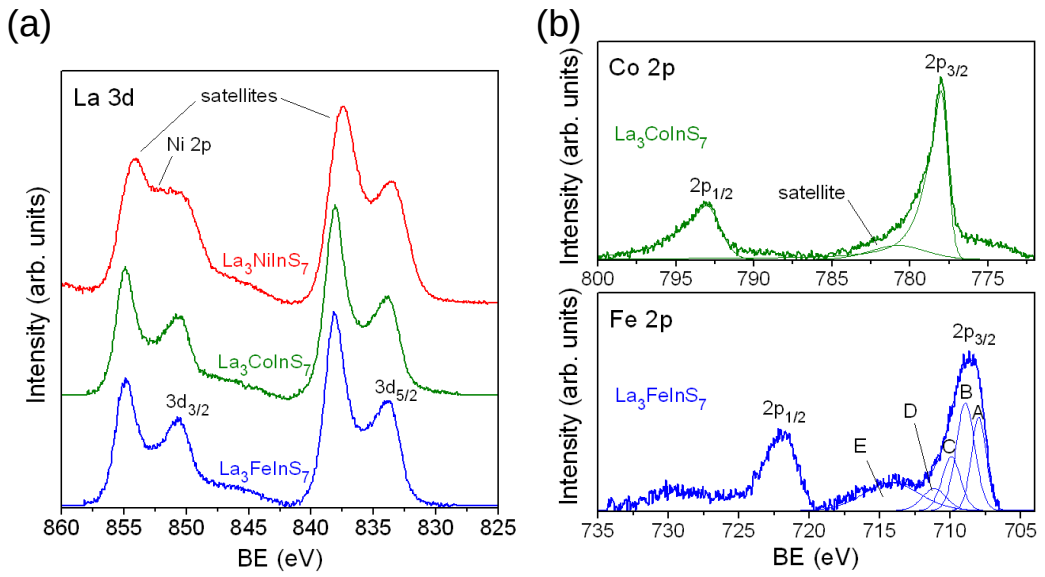

Figure 2-4 (a) La 3d and (b) Fe and Co 2p XPS spectra for La_3MInS_7.

The *M* 2p spectra are expected to provide important information about the valence of the transition-metal component in La_3MInS_7. Both the Fe 2p and Co 2p spectra are quite well-resolved (Figure 2-4b), the former being relatively complex for reasons to be explained separately below. The Co 2p spectrum of La_3CoInS_7 reveals peaks with asymmetric tails to higher BE, a feature that originates from delocalization of valence electrons and is observed in electrically conducting compounds such as Co metal itself, CoS_2, and $CoSb_3$.[51,52] The Co $2p_{3/2}$ BE in La_3CoInS_7 (778.0 eV) is essentially unchanged from these compounds (778.1 eV). Satellite peaks to the high BE side of the core-line peaks are typical

in Co 2p spectra,[52] but here their intensity is too low to permit analysis. Unfortunately, the Ni 2p spectrum is partly obscured within the La 3d spectrum (Figure 2-4a). In fact, the Ni $2p_{3/2}$ peak lies between the La $3d_{3/2}$ peak and the shake-up satellite peak, and its BE could only be approximately estimated as 852.3 eV, which is closer to Ni metal (852.7 eV) and NiS (853.0 eV) than to NiO (854.8 eV).[53]

The Fe 2p spectrum reveals considerable fine structure that provides rich information about the local bonding environment of Fe atoms in La_3FeInS_7. The Fe $2p_{3/2}$ core-line peak is manifested as an envelope centred around 709 eV. A broad satellite peak (E) is found at higher BE centred around 714 eV, which can be attributed in part to shake-up or charge transfer processes involving Fe^{2+} species;[54–56] this peak is persistent in repeated measurements over multiple samples. However, an In loss peak related to the In $3p_{1/2}$ core-line likely overlaps in this region, precluding further analysis of this Fe satellite peak. On the basis of theoretical predictions by Gupta and Sen[54,55] and previous analysis of other metal 2p spectra,[56–58] the main Fe core-line peak can be fitted to three component peaks, which originate from multiplet splitting, at 708.0 eV (A), 708.9 eV (B), and 709.9 eV (C). The relative areas of these component peaks (31.2% for A, 45.9% for B, and 22.8% for C) are similar to those found for iron(II) halides (e.g., 31.3%, 42.4%, and 26.3%, respectively, in $FeBr_2$)[56] and are in reasonable agreement with theoretical values (36.1%, 46.4%, and 17.5%, respectively).[54–56] The widths of these component peaks (full-width-at-half-maximum, FWHM, of 1.2–1.6 eV) lie within similar ranges as in previous analyses.[54–58] The Fe $2p_{3/2}$ BE, which is

typically evaluated as the peak centre of gravity weighted by the relative component peak areas, is 708.9 eV for La_3FeInS_7. Correlations deduced from the literature indicate that the Fe $2p_{3/2}$ BE tends to increase with greater ionic bonding character and higher Fe valence, as demonstrated by the values seen in iron(II) halides (708.0 eV in $FeBr_2$, 711.5 eV in FeF_2) vs. iron(III) halides (710 eV in $FeBr_3$, 715.1 eV in FeF_3).[56] The low Fe $2p_{3/2}$ BE seen in La_3FeInS_7 supports the presence of high-spin Fe^{2+} species and implies significant covalent character in the Fe–S bonds. In this respect, it is interesting that La_3FeInS_7 is quite dissimilar to FeS_2, which also contains Fe^{2+} species octahedrally coordinated by S atoms, but shows an Fe $2p_{3/2}$ BE of 707 eV and little multiplet splitting in its Fe 2p spectrum[59]. The difference arises because the Fe^{2+} species in FeS_2 are low-spin in the bulk solid, and the absence of unpaired electrons will not generate multiplet splitting in the spectrum. Finally, proper fitting of the spectrum of La_3FeInS_7 requires an additional small peak (D) at 711.1 eV, which we attribute to surface oxides.

The In 3d spectra contain peaks intrinsic to the sample as well as from the metallic indium foil used in the sample mounting. The indium foil thus conveniently serves as an internal standard. The In $3d_{5/2}$ peak lies at higher BE (444.6–444.7 eV) for all members of La_3MInS_7 (M = Fe, Co, Ni) relative to that for elemental indium (443.7 eV), consistent with the presence of trivalent In species, similar to In_2S_3 (444.7–445.1 eV), $CuInS_2$ (444.6–444.8 eV), and In_2O_3 (444.8 eV).[53] The S 2p spectra show that the $2p_{3/2}$ core-line peaks are substantially shifted to lower BE (161.2–161.3 eV) relative to elemental sulphur

(163.8 eV) and are similar to various transition-metal sulphides (e.g., 160.8–161.4 eV in FeS),[53] indicating the presence of anionic S species.

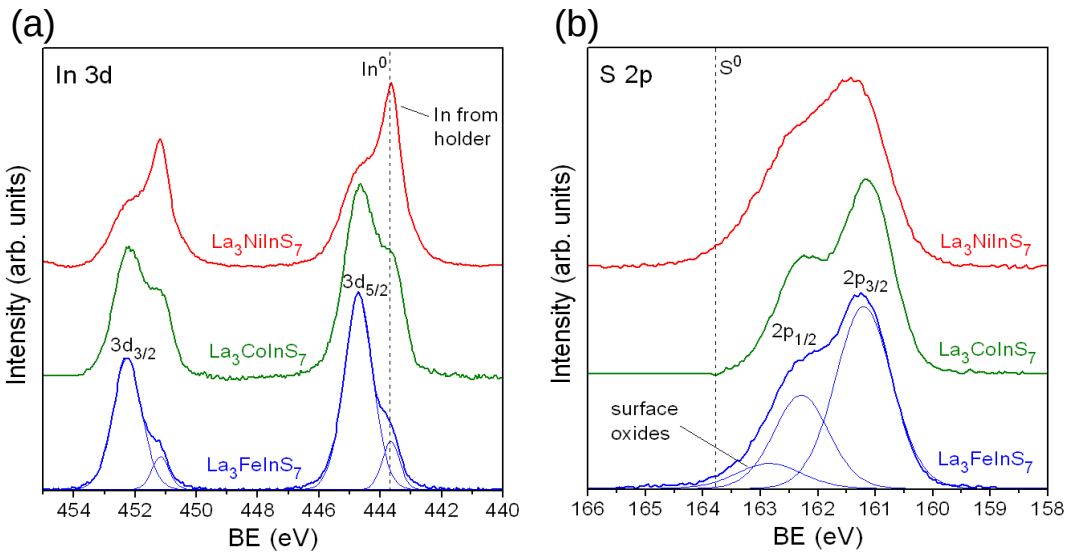

Figure 2-5 (a) In 3d and (b) S 2p XPS spectra for La_3MInS_7. The vertical dashed lines mark the In $3d_{5/2}$ BE at 443.7 eV for elemental In and the S $2p_{3/2}$ BE at 163.8 eV for elemental S.

Table 2-4 XPS binding energies (eV) for La_3MInS_7 (*M* = Fe, Co, Ni). [a]

	La_3FeInS_7	La_3CoInS_7	La_3NiInS_7
La $3d_{5/2}$	833.8	833.8	833.6
M $2p_{3/2}$	708.9 [b]	778.0	852.3
In $3d_{5/2}$	444.7	444.7	444.6
S $2p_{3/2}$	161.2	161.2	161.3

[a] BEs have an estimated precision of better than ±0.1 eV. [b] Fe $2p_{3/2}$ BE is evaluated as peak centre of gravity weighted by component peak areas; see text for further details.

2.3.3 Magnetism

The magnetic properties of La_3MInS_7 (M = Fe, Co, Ni) are potentially interesting given the one-dimensional arrangement of M atoms within isolated chains of face-sharing octahedra. The magnetic susceptibility for these compounds tends to remain rather flat upon decreasing temperature and then rises rapidly at low temperature, but the overall dependence is decidedly non-Curie-Weiss (Figure 2-6). In La_3FeInS_7, there is a kink around 30 K suggestive of an antiferromagnetic transition; although the sample appears to be >99% phase-pure from its XRD powder pattern (Figure 2-1), we remain skeptical that it is intrinsic to the quaternary compound. (For example, monoclinic pyrrhotite, Fe_7S_8, is ferrimagnetic with a transition between 30 and 34 K.[60]) In La_3CoInS_7, the curvature at intermediate temperatures near 100 K is concave down, resembling the behaviour previously seen for the isostructural aluminum-containing series La_3MAlS_7 (M = Mn, Fe, Co) for which broad maxima are found near this temperature.[25] In La_3NiInS_7, no transitions are evident but the inverse susceptibility is clearly non-linear. The rounded maxima in the magnetic susceptibility of La_3MAlS_7 have been interpreted as evidence for one-dimensional antiferromagnetic ordering;[25] an Ising model was applied to extract effective magnetic moments μ_{eff} that imply high-spin M^{2+} species and exchange energies J that are negative.[25,61] We have attempted to fit the high-temperature data for La_3MInS_7 (M = Fe, Co, Ni) in the same manner (not shown), yielding effective magnetic moments of 6.5, 4.6, and 1.7 μ_B that are inconsistent with the free-ion spin-only values (4.9, 3.9, and 2.8 μ_B) for Fe^{2+}, Co^{2+}, and Ni^{2+}, respectively.

Efforts are in progress to optimize crystal growth to permit measurements of single-crystal magnetization as well as electrical resistivity. Given that the exchange interactions will be controlled largely by the intrachain *M*–*M* distances, which are slightly longer in La_3MInS_7 (3.14 Å) than in La_3MAlS_7 (3.01 Å),[25] it will also be interesting to determine the magnetic properties of the currently unknown gallium-containing series La_3MGaS_7, which will have an intermediate *M*–*M* distance.

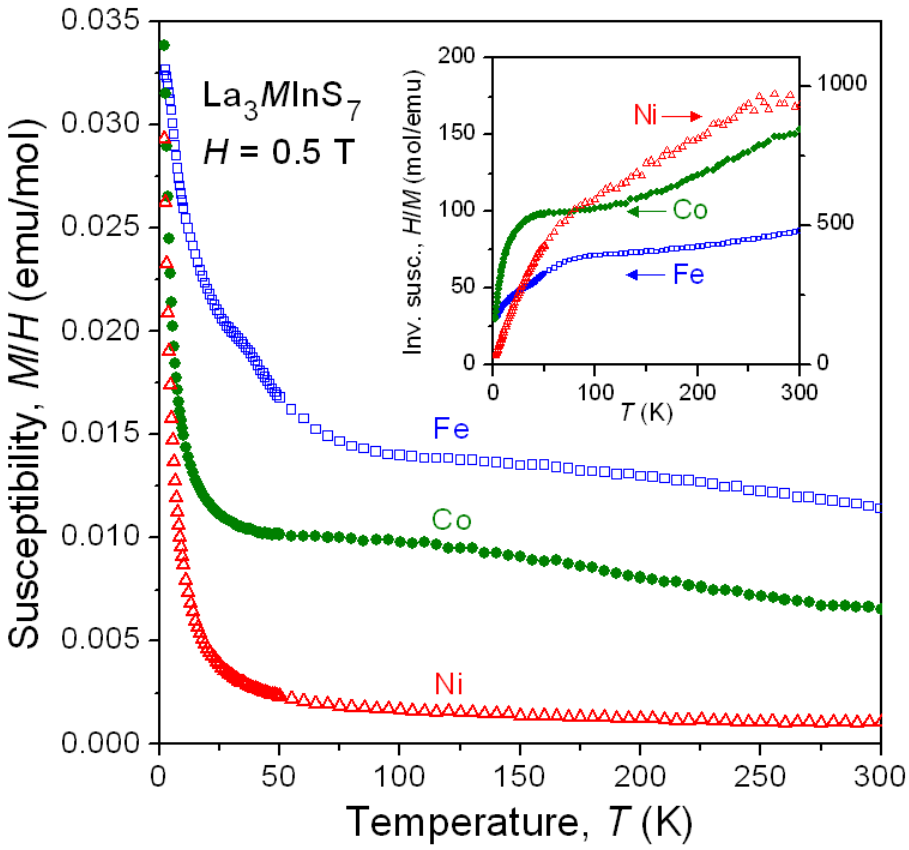

Figure 2-6 Magnetic susceptibility and its inverse (inset) as a function of temperature for La_3MInS_7 (*M* = Fe, Co, Ni).

To further examine the effect of transition-metal substitution in this series, the electronic band structures have been calculated for La_3MInS_7 (*M* = Fe, Co,

Ni). To a first approximation, the charge-balanced formulation $(La^{3+})_3(M^{2+})(In^{3+})(S^{2-})_7$ implies that the valence orbitals are empty for La and In atoms, partly occupied for *M* atoms, and completely filled for S atoms. This expectation is largely met in the density of states (DOS) curves (Figure 2-7a). The valence band is dominated by S 3p-based states at lower energies and *M* 3d-based states at higher energies, especially near the Fermi level, with small admixtures of La- and In-based states throughout the energy range from about –5 to +1 eV. The pattern of the *M* 3d-bands reflects the familiar crystal field splitting of the octahedrally coordinated *M* atoms; more precisely, they correspond to 1a, 1e, and 2e bands (the former two overlapping) in order of increasing energy derived from a chain of face-sharing octahedral.[62] The Fermi level is located just at the gap between the 1a/1e and 2e bands in La_3FeInS_7, which is predicted to be semiconducting with a band gap of 0.25 eV, similar to many other $RE_3MM'Ch_7$ compounds. On proceeding from La_3FeInS_7 to La_3NiInS_7, the increased electronegativity and greater number of electrons provided by the *M* atom combine to lower these bands in energy and shift the relative position of the Fermi level so that it now cuts the upper 2e band. However, these bands are fairly narrow and the development of metallic behaviour will also depend on consideration of the on-site electron-electron repulsion, not evaluated in this calculation. More rigorous calculations may be helpful for interpreting the magnetic properties of these compounds. The strongest bonding interactions in La_3MInS_7 are provided by the *M*–S and In–S contacts, as exemplified by the crystal orbital Hamilton population curves for La_3FeInS_7 (Figure 2-7b). The

narrow *M* 3d bands participate in strongly antibonding *M*–S interactions, and their increasing occupation on progressing from La_3FeInS_7 to La_3NiInS_7 leads to a significant change in the integrated COHP values (–ICOHP) from 2.0 to 1.6 eV/bond, consistent with the *M*–S bond lengthening noted earlier. In contrast, the La–S and In–S interactions are entirely bonding and located well below the Fermi level, so that they remain invariant (–ICOHP values of 0.8 and 2.0 eV/bond, respectively) in La_3FeInS_7, La_3CoInS_7, and La_3NiInS_7. Within the octahedral chains, the *M*–*M* bonding is rather weak but non-negligible (–ICOHP values of 0.3 to 0.2 eV/bond).

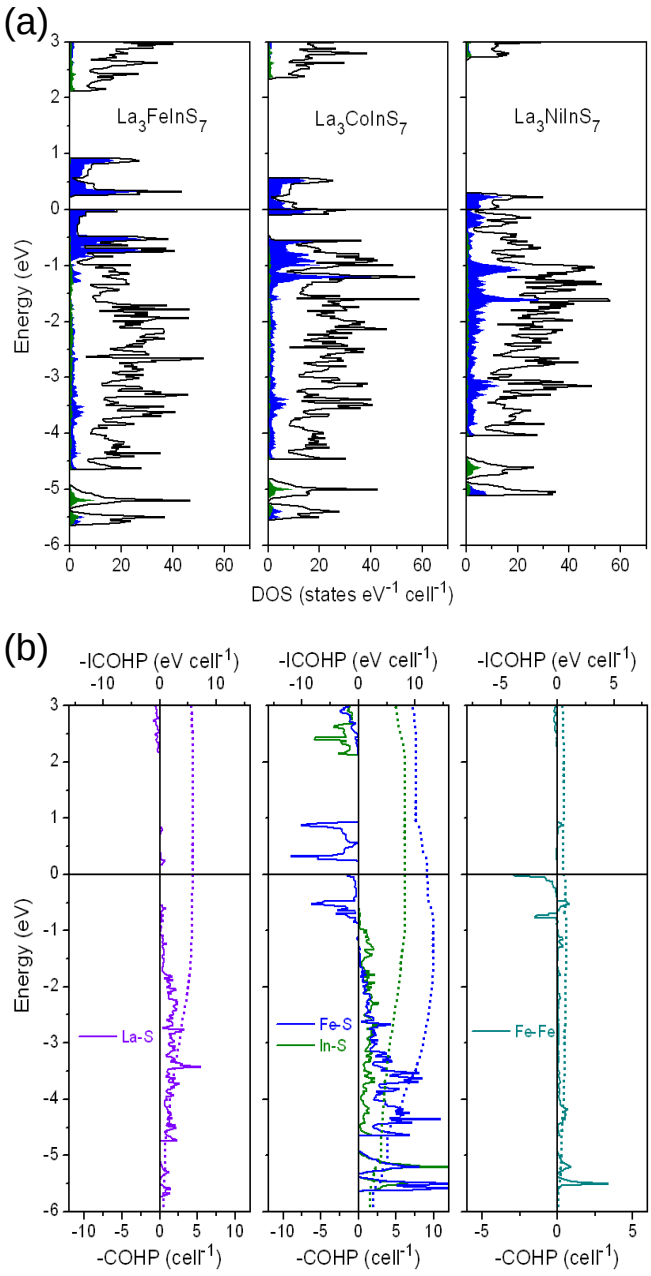

Figure 2-7 (a) Density of states (DOS) for La_3MInS_7 (M = Fe, Co, Ni), with the Fermi level at 0 eV. The atomic projections of the DOS are highlighted in blue for M-based states and green for In-based states; the remainder of the DOS is largely contributed by S-based states below the Fermi level and by La-based states above. (b) Crystal orbital Hamilton population (–COHP) curves (solid lines) and their integrations (dotted lines) for La–S, Fe–S, In–S, and Fe–Fe contacts in La_3FeInS_7.

2.4 Conclusions

Quaternary chalcogenides $RE_3MM'Ch_7$ belonging to the family of noncentrosymmetric La_3CuSiS_7-type compounds have now been extended to include examples in which divalent transition-metal atoms occupy the *M* site and In atoms occupy the *M′* site in the title compounds. The assignment of these valences is supported by the XPS spectra, bond valence sums, and band structure calculations. In contrast to most other La_3CuSiS_7-type compounds, which generally contain species with only closed-shell electron configurations, the magnetic properties of La_3MInS_7 (*M* = Fe, Co, Ni) originate from interactions between moments on the *M* atoms along chains of face-sharing octahedra. More detailed interpretation of these magnetic properties, as well as measurement of the electrical properties with the aim to uncover ferroelectric behaviour, awaits the optimization of larger single crystals. It will also be interesting to extend the substitution of *M* component to a metal that has filled subshells, such as Zn, in hopes of identifying candidates that may have good non-linear optical properties. The extension of this system to other II-III combinations is very important and will be further addressed in Chapter 3.

2.5 References

[1] M. Guittard, M. Julien-Pouzol, P. Laruelle, J. Flahaut, C. R. Acad. Sci., Ser. C 267 (1968) 767–769.

[2] M. Guittard, M. Julien-Pouzol, Bull. Soc. Chim. Fr. (1970) 2467–2469.

[3] G. Collin, J. Flahaut, Bull. Soc. Chim. Fr. (1972) 2207–2209.

[4] G. Collin, J. Étienne, J. Flahaut, M. Guittard, P. Laruelle, Rev. Chim. Miner. 10 (1973) 225–238.

[5] S.-J. Hwu, C.K. Bucher, J.D. Carpenter, S.P. Taylor, Inorg. Chem. 34 (1995) 1979–1980.

[6] S.-H. Lin, J.-G. Mao, G.-C. Guo, J.-S Huang, J. Alloys Compd. 252 (1997) L8–L11.

[7] F.Q. Huang, J.A. Ibers, Acta Crystallogr., Sect. C 55 (1999) 1210–1212.

[8] K.M. Poduska, F.J. DiSalvo, K. Min, P.S. Halasyamani, J. Alloys Compd. 335 (2002) L5–L9.

[9] M. Daszkiewicz, L.D. Gulay, A. Pietraszko, V.Ya. Shemet, J. Solid State Chem. 180 (2007) 2053–2060.

[10] L.D. Gulay, V.Ya. Shemet, I.D. Olekseyuk, J. Alloys Compd. 385 (2004) 160–168.

[11] L.-B. Wu, F.-Q. Huang, Z. Kristallogr. – New Cryst. Struct. 220 (2005) 307–308.

[12] L.D. Gulay, D. Kaczorowski, A. Pietraszko, J. Alloys Compd. 403 (2005) 49–52.

[13] L.D. Gulay, I.D. Olekseyuk, J. Alloys Compd. 388 (2005) 274–278.

[14] L.D. Gulay, O.S. Lychmanyuk, J. Stępień-Damm, A. Pietraszko, I.D. Olekseyuk, J. Alloys Compd. 402 (2005) 201–203.

[15] L.D. Gulay, V.Ya. Shemet, I.D. Olekseyuk, J. Alloys Compd. 388 (2005) 59–64.

[16] L.D. Gulay, I.D. Olekseyuk, M. Wolcyrz, J. Stępień-Damm, Z. Anorg. Allg. Chem. 631 (2005) 1919–1923.

[17] L.D. Gulay, O.S. Lychmanyuk, M. Wolcyrz, A. Pietraszko, I.D. Olekseyuk, J. Alloys Compd. 425 (2006) 159–163.

[18] L.D. Gulay, O.S. Lychmanyuk, I.D. Olekseyuk, A. Pietraszko, J. Alloys Compd. 422 (2006) 203–207.

[19] L.D. Gulay, O.S. Lychmanyuk, J. Stępień-Damm, A. Pietraszko, I.D. Olekseyuk, J. Alloys Compd. 414 (2006) 113–117.

[20] O.S. Lychmanyuk, L.D. Gulay, I.D. Olekseyuk, Pol. J. Chem. 80 (2006) 463–469.

[21] I. Hartenbach, A.C. Müller, T. Schleid, Z. Anorg. Allg. Chem. 632 (2006) 2147.

[22] L.D. Gulay, O.S. Lychmanyuk, I.D. Olekseyuk, M. Daszkiewicz, J. Stępień-Damm, A. Pietraszko, J. Alloys Compd. 431 (2007) 185–190.

[23] O.S. Lychmanyuk, L.D. Gulay, I.D. Olekseyuk, J. Stępień-Damm, M. Daszkiewicz, A. Pietraszko, Pol. J. Chem. 81 (2007) 353–367.

[24] O.M. Strok, M. Daszkiewicz, L.D. Gulay, D. Kaczorowski, J. Alloys Compd. 493 (2010) 47–49.

[25] K.S. Nanjundaswamy, J. Gopalakrishnan, J. Solid State Chem. 49 (1983) 51–58.

[26] P.M. Van Calcar, P.K. Dorhout, Mater. Sci. Forum 315 (1999) 322–330.

[27] L.-B. Wu, F.-Q. Huang, Z. Kristallogr. – New Cryst. Struct. 220 (2005) 305–306.

[28] W. Yin, W. Wang, L. Kang, Z. Lin, K. Feng, Y. Shi, W. Hao, J. Yao, Y. Wu, J. Solid State Chem. 202 (2013) 269–275.

[29] R.L. Gitzendanner, C.M. Spencer, F.J. DiSalvo, M.A. Pell, J.A. Ibers, J. Solid State Chem. 131 (1996) 399–404.

[30] M.R. Huch, L.D. Gulay, I.D. Olekseyuk, J. Alloys Compd. 424 (2006) 114–118.

[31] S.-P. Guo, G.-C. Guo, M.-S. Wang, J.-P. Zou, G. Xu, G.-J. Wang, X.-F. Long, J.-S. Huang, Inorg. Chem. 48 (2009) 7059–7065.

[32] D. de Saint-Giniez, P. Laruelle, J. Flahaut, C. R. Acad. Sci., Ser. C 267 (1968) 1029–1032.

[33] A.M. Mills, M. Ruck, Acta Crystallogr., Sect. C 60 (2004) i71–i72.

[34] A.M. Mills, D. Bräunling, H. Rosner, W. Schnelle, C.P. Sebastian, R. Pöttgen, M. Ruck, J. Solid State Chem. 182 (2009) 1136-1141.

[35] M. Daszkiewicz, O.M. Strok, L.D. Gulay, D. Kaczorowski, J. Alloys Compd. 508 (2010) 258–261.

[36] S.C. Abrahams, Acta Crystallogr., Sect. B 46 (1990) 311–324.

[37] M. Daszkiewicz, L.D. Gulay, Mater. Res. Bull. 47 (2012) 497–499.

[38] I. Hartenbach, T. Nilges, T. Schleid, Z. Anorg. Allg. Chem. 633 (2007) 2445–2452.

[39] G.M. Sheldrick, SHELXTL, version 6.12, Bruker AXS Inc., Madison, WI, 2001.

[40] L.M. Gelato, E. Parthé, J. Appl. Crystallogr. 20 (1987) 139–143.

[41] N. Fairley, CasaXPS, version 2.3.9, Casa Software Ltd., Teighnmouth, Devon, UK, 2003, http://www.casaxps.com.

[42] R. Tank, O. Jepsen, A. Burkhardt, O.K. Andersen, TB-LMTO-ASA Program, version 4.7, Max Planck Institut für Festkörperforschung, Stuttgart, Germany, 1998.

[43] N.E. Brese, M. O'Keeffe, Acta Crystallogr., Sect. B 47 (1991) 192–197.

[44] P.E.R. Blanchard, B.R. Slater, R.G. Cavell, A. Mar, A.P. Grosvenor, Solid State Sci. 12 (2009) 50–58.

[45] A. Novosselov, E. Talik, A. Pajaczkowska, J. Alloys Compd. 351 (2003) 50–53.

[46] E. Talik, A. Novosselov, M. Kulpa, A. Pajaczkowska, J. Alloys Compd. **321** (2001) 24–26.

[47] W. Grünert, U. Sauerlandt, R. Schlögl, H.G. Karge, J. Phys. Chem. 97 (1993) 1413–1419.

[48] S.J. Oh, G.H. Kim, G.A. Sawatzky, H.T. Jonkman, Phys. Rev. B 37 (1988) 6145–6152.

[49] A.J. Signorelli, R.G. Hayes, Phys. Rev. B 8 (1973) 81–86.

[50] G. Crecelius, G.K. Wertheim, D.N.E. Buchanan, Phys. Rev. B 18 (1978) 6519–6524.

[51] H. van der Heide, R. Hemmel, C.F. van Bruggen, C. Haas, J. Solid State Chem. 33 (1980) 17–25.

[52] A.P. Grosvenor, R.G. Cavell, A. Mar, Phys. Rev. B 74 (2006) 125102-1–125102-10.

[53] C.D Wagner, A. V. Naumkin, A. Kraut-Vass, J.W. Allison, C.J. Powell, J. R. Rumble Jr., NIST X-ray Photoelectron Spectroscopy Database, version 3.5 (web version), National Institute of Standards and Technology, Gaithersburg, MD 2003, http://srdata.nist.gov/xps.

[54] R.P. Gupta, S.K. Sen, Phys. Rev. B 10 (1974) 71–77.

[55] R.P. Gupta, S.K. Sen, Phys Rev. B 12 (1975) 15–19.

[56] A.P. Grosvenor, B.A. Kobe, M.C. Biesinger, N.S. McIntyre, Surf. Interface Anal. 36 (2004) 1564-1574.

[57] N.S. McIntyre, D.G. Zetaruk, Anal. Chem. 49 (1977) 1521–1529.

[58] S.P. Kowalczyk, L. Ley, F.R. McFeely, D.A. Shirley, Phys. Rev. B 11 (1975) 1721–1727.

[59] H.W. Nesbitt, M. Scaini, H. Höchst, G.M. Bancroft, A.G. Schaufuss, R. Szargan, Am. Mineral. 85 (2000) 850–857.

[60] P. Rochette, G. Fillion, J.-L. Mattéi, M.J. Dekkers, Earth Planet. Sci. Lett. 98 (1990) 319–328.

[61] S. Emori, M. Inoue, M. Kishita, M. Kubo, Inorg. Chem. 8 (1969) 1385–1388.

[62] M.-H. Whangbo, M.J. Foshee, R. Hoffman, Inorg. Chem. 19 (1980) 1723–1728

Chapter 3

Rare-earth transition-metal gallium chalcogenides RE_3MGaCh_7 (*M* = Fe, Co, Ni; *Ch* = S, Se)[1]

3.1 Introduction

In Chapter 2, the extension of the family of quaternary noncentrosymmetric rare-earth chalcogenide compounds, $RE_3MM'S_7$, adopting the $Ce_3Al_{1.67}S_7$-type structure to In-containing analogues was discussed. The hexagonal crystal structure ($P6_3$), which forms for various M/M' combinations (as long as the valences sum to five), have traditionally been investigated for I-IV combinations,[1-24] but show potentially large versatility with extensions to II-III (including those discussed in Chapter 2),[3,4,25–30] III-II,[3,4] vacancy containing,[31-35] and electron deficient compounds.[36] The properties of these hexagonal quaternary chalcogenides $RE_3MM'Ch_7$ remain largely unexamined. Given their noncentrosymmetric structure, it has been speculated that these compounds should exhibit ferroelectric or nonlinear optical properties.[8,33,37] Recently $Y_3Zn_{0.5}SiS_7$ and related compounds have been reported to exhibit strong second harmonic generation effects.[35] The Ag-deficient derivatives $La_3Ag_{0.82}SnS_7$[36] and $Ce_3Ag_{0.63}SiS_{6.63}Cl_{0.37}$[38] show significantly elongated displacement ellipsoids suggestive of ionic conduction. The presence of transition-metal components *M*

[1] *A version of this chapter has been published. B.W Rudyk, S.S. Stoyko, A.O. Oliynyk, A. Mar, J. Solid State Chem. 210 (2014) 79-88. Copyright (2014) by Elsevier.*

in low-dimensional arrangements may lead to interesting magnetic properties, but few studies have been made on the magnetic behaviour of $RE_3MM'Ch_7$ compounds.[26,29] It is also of interest to examine the magnetic properties as the local environments around magnetic centres change due to changes in lattice parameters and the *c/a* ratio.

A large number of new quaternary rare-earth transition-metal gallium chalcogenides RE_3MGaCh_7 (*M* = Fe, Co, Ni; *Ch* = S, Se) are reported in this chapter. They have been characterized by X-ray diffraction (XRD) studies, including single-crystal structure determinations on five of the quaternary sulphides. Their electronic structures have been analyzed through band structure calculations. Magnetic measurements have been made on many of the compounds prepared here. X-ray absorption near-edge spectroscopy (XANES) has been applied to probe the electronic environment around the Ga atoms in these compounds.

3.2 Experimental

3.2.1 Synthesis

Starting materials were freshly filed *RE* pieces (*RE* = Y, La–Er, 99.9%, Hefa), Fe powder (99.9%, Cerac), Co powder (99.8%, Cerac), Ni powder (99.9%, Cerac), Ga shot (99.99%, Cerac), S flakes (99.998%, Sigma-Aldrich), and Se powder (99.99%, Sigma-Aldrich). The title compounds were prepared from stoichiometric mixtures of the elements in a total mass of 0.200 g which were pressed into pellets (6 mm diameter, 1–3 mm thickness) and loaded into fused-

silica tubes which were evacuated and sealed. For the sulphides RE_3MGaS$_7$, the tubes were heated to 1050 °C, kept there for 2 weeks, and cooled to room temperature over 12 h. For the selenides RE_3MGaSe$_7$, the tubes were heated to 900 °C, kept there for 5 days, and cooled to room temperature over 12 h. The products were characterized by powder X-ray diffraction (XRD) patterns collected on an Inel diffractometer equipped with a curved position-sensitive detector (CPS 120) and a Cu $K\alpha_1$ radiation source operated at 40 kV and 20 mA. Representative powder XRD patterns are shown in Figure 3-1.

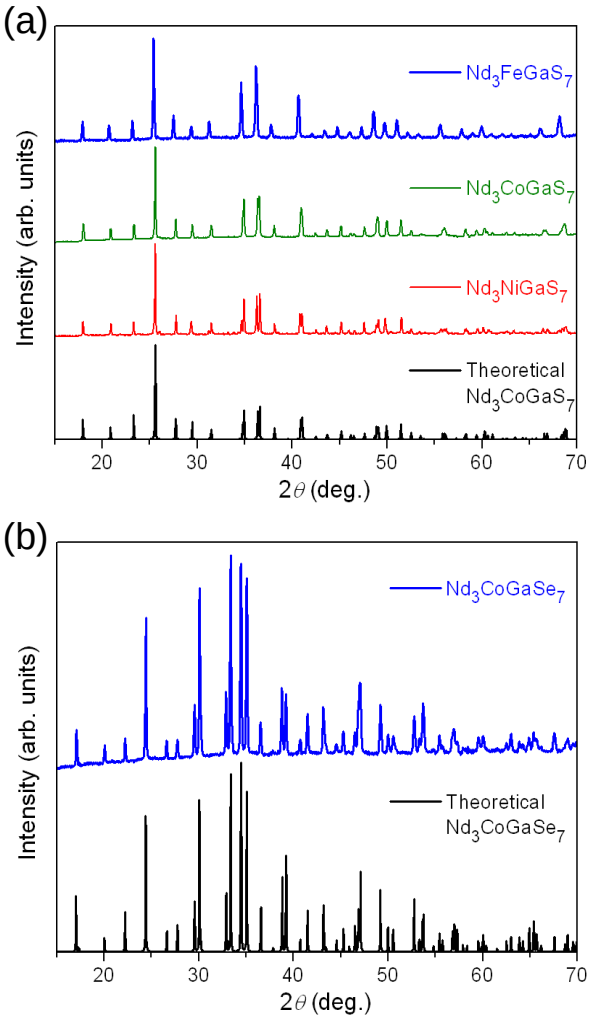

Figure 3-1 Powder XRD patterns for (a) Nd_3MGaS_7 (*M* = Fe, Co, Ni) and (b) $Nd_3CoGaSe_7$.

Of the 33 compounds identified here, the majority were formed nearly quantitatively (95–100%). Only a few samples (Dy_3FeGaS_7, La_3NiGaS_7, Dy_3NiGaS_7, $La_3CoGaSe_7$, $La_3NiGaSe_7$, and $Nd_3NiGaSe_7$) contained more than 5% admixtures of other phases (usually RE_2S_3 or RE_2Se_3). Within the sulphide series RE_3MGaS_7, attempts were made to extend the *RE* substitution to later members (up to Lu) and the *M* substitution to 2nd-row transition metals (*M* = Ru, Rh, Pd), to no avail. Within the selenide series RE_3MGaSe_7, we only attempted

limited experiments on *RE* substitution (*RE* = La, Nd) but suspect that these can be extended further. Cell parameters refined from the powder XRD data are listed in Table 3-1.

Table 3-1 Cell parameters for RE_3MGaQ_7 (*M* = Fe, Co, Ni; *Q* = S, Se). [a]

Compound	*a* (Å)	*c* (Å)	*V* (Å^3)	Reference
***RE*$_3$FeGaS$_7$**				
La_3FeGaS_7	10.1972(2)	6.0376(1)	543.69(2)	This work
Ce_3FeGaS_7	10.0772(2)	6.0181(2)	529.26(2)	This work
Pr_3FeGaS_7	10.0139(2)	6.0489(2)	525.31(2)	This work
Nd_3FeGaS_7	9.9081(4)	6.0709(2)	516.14(3)	This work
Nd_3FeGaS_7	9.9041(2)	6.0722(2)	515.83(2)	[29]
Sm_3FeGaS_7	9.7474(2)	6.0583(2)	498.49(2)	This work
Sm_3FeGaS_7	9.7876(2)	6.0989(2)	505.98(2)	[29]
Gd_3FeGaS_7	9.6519(2)	6.0789(3)	490.44(2)	This work
Gd_3FeGaS_7	9.6933(3)	6.1281(3)	498.65(3)	[29]
Tb_3FeGaS_7	9.6326(2)	6.0902(2)	489.38(2)	This work
Dy_3FeGaS_7	9.6130(2)	6.0866(2)	487.11(2)	This work
Dy_3FeGaS_7	9.5946(2)	6.1114(2)	487.22(2)	[29]
***RE*$_3$CoGaS$_7$**				
Y_3CoGaS_7	9.5470(2)	6.0835(2)	480.20(2)	This work
La_3CoGaS_7	10.1383(2)	6.0073(2)	534.73(2)	This work
Ce_3CoGaS_7	10.0208(2)	6.0113(2)	522.76(3)	This work
Pr_3CoGaS_7	9.9048(2)	6.0354(2)	512.78(3)	This work
Nd_3CoGaS_7	9.8200(2)	6.0603(2)	506.11(3)	This work
Sm_3CoGaS_7	9.7281(2)	6.0819(3)	498.45(3)	This work
Gd_3CoGaS_7	9.6186(3)	6.0922(3)	488.12(3)	This work
Tb_3CoGaS_7	9.5843(3)	6.0789(3)	483.59(3)	This work
Dy_3CoGaS_7	9.5313(2)	6.0733(2)	477.81(2)	This work
Ho_3CoGaS_7	9.5058(2)	6.0718(2)	475.15(2)	This work
Er_3CoGaS_7	9.4706(2)	6.0648(2)	471.08(2)	This work
***RE*$_3$NiGaS$_7$**				
La_3NiGaS_7	10.1155(2)	6.0163(2)	533.13(2)	This work
Ce_3NiGaS_7	9.9814(2)	6.0302(2)	520.29(2)	This work
Pr_3NiGaS_7	9.8784(2)	6.0575(2)	511.91(2)	This work

Nd_3NiGaS_7	9.8086(2)	6.0844(2)	506.95(2)	This work
Sm_3NiGaS_7	9.6795(2)	6.0934(2)	494.42(2)	This work
Gd_3NiGaS_7	9.6046(2)	6.0967(2)	487.06(2)	This work
Tb_3NiGaS_7	9.5667(2)	6.0756(2)	481.56(2)	This work
Dy_3NiGaS_7	9.5234(2)	6.0778(2)	477.37(2)	This work
***RE*$_3$FeGaSe$_7$**				
$La_3FeGaSe_7$	10.5042(2)	6.3496(2)	606.74(2)	This work
$Nd_3FeGaSe_7$	10.2229(2)	6.4059(2)	579.77(2)	This work
$Nd_3FeGaSe_7$	10.2453(3)	6.4076(2)	582.47(3)	[29]
$Gd_3FeGaSe_7$	10.0762(2)	6.4265(2)	565.07(2)	[29]
$Dy_3FeGaSe_7$	9.9956(2)	6.3980(2)	553.60(2)	[29]
***RE*$_3$CoGaSe$_7$**				
$La_3CoGaSe_7$	10.5104(2)	6.3708(2)	609.48(2)	This work
$Nd_3CoGaSe_7$	10.2296(2)	6.4272(2)	582.47(2)	This work
***RE*$_3$NiGaSe$_7$**				
$La_3NiGaSe_7$	10.4826(2)	6.3964(2)	608.71(2)	This work
$Nd_3NiGaSe_7$	10.2117(2)	6.4066(2)	578.57(2)	This work

[a] Cell parameters obtained from samples in this work were refined from powder XRD data, whereas those reported from previous literature were refined from single-crystal XRD data.

3.2.2 Structure determination

Small single crystals were available for five of the sulphide samples: RE_3FeGaS_7 (*RE* = La, Pr, Tb) and RE_3CoGaS_7 (*RE* = La, Tb). The identities of the crystals selected for structure determination were verified by energy-dispersive X-ray (EDX) analysis performed on a JEOL JSM-6010LA scanning electron microscope. The average chemical compositions (26(1)% *RE*, 8(2)% *M*, 8(1)% Ga, 59(1)% S) were in excellent agreement with the expected values (25% *RE*, 8% *M*, 8% Ga, 58% S). These crystals were mounted on a Bruker PLATFORM diffractometer equipped with a SMART APEX II CCD detector and

a graphite-monochromated Mo $K\alpha$ radiation source. Intensity data were collected at 173 K using ω scans at 4–8 different ϕ angles with a frame width of 0.3º and an exposure time of 12 s per frame. Face-indexed absorption corrections were applied. Structure solution and refinement were carried out with use of the SHELXTL (version 6.12) program package.[39] The noncentrosymmetric space group $P6_3$ was chosen by analogy with $RE_3M\mathrm{InS}_7$ and other related hexagonal chalcogenides $RE_3MM'Ch_7$. Initial atomic positions were located by direct methods. Refinements proceeded with little complication. The displacement parameters were unextraordinary and there were no problems arising from partial occupancy or disorder. Atomic positions were generally chosen to conform to standardized values suggested by the program STRUCTURE TIDY,[40] with the *z*-coordinate of the *M* atom fixed at the origin in this polar space group, while ensuring that the absolute configuration was preserved. Table 3-2 lists crystal data and details of the data collection, Table 3-3 lists positional and displacement parameters, and Table 3-4 lists selected interatomic distances. Further data, in CIF format, have been sent to Fachinformationszentrum Karlsruhe, Abt. PROKA, 76344 Eggenstein-Leopoldshafen, Germany, as supplementary material No. CSD-426674 to 426678 and can be obtained by contacting FIZ (quoting the article details and the corresponding CSD numbers).

3.2.3 Magnetic susceptibility measurements

Measurements of dc magnetic susceptibility (χ vs. T) were made on $RE_3\mathrm{FeGaS}_7$ (*RE* = La–Nd, Sm, Gd–Tb), $RE_3\mathrm{CoGaS}_7$ (*RE* = Y, La–Nd, Sm, Gd–

Er), RE_3NiGaS_7 (*RE* = Ce, Tb), and RE_3MGaSe_7 (*RE* = La, Nd; *M* = Fe, Co, Ni) between 2 and 300 K under an applied field of 0.5 T on a Quantum Design 9T-PPMS magnetometer. Susceptibility values were corrected for contributions from the holder and sample diamagnetism. Isothermal magnetization measurements (*M* vs. *H*) were made on several of these samples at 2 K and 100 K, generally when transitions were observed in the susceptibility curves.

Table 3-2 Crystallographic data for RE_3FeGaS_7 and RE_3CoGaS_7.

Formula	La_3FeGaS_7	Pr_3FeGaS_7	Tb_3FeGaS_7	La_3CoGaS_7	Tb_3CoGaS_7
Formula mass (amu)	766.72	772.72	826.75	769.80	829.83
Space group	$P6_3$ (No. 173)	$P6_3$ (No. 173)	$P6_3$ (No. 173)	$P6_3$ (No. 173)	$P6_3$ (No. 173)
a (Å)	10.1795(16)	9.9846(4)	9.6411(13)	10.1691(13)	9.6216(10)
c (Å)	6.0217(10)	6.0303(5)	6.1024(8)	6.0080(8)	6.0972(6)
V (Å^3)	540.38(15)	520.63(5)	491.23(11)	538.05(12)	488.83(9)
Z	2	2	2	2	2
ρ_{calcd} (g cm^{-3})	4.712	4.929	5.589	4.752	5.638
T (K)	173	173	173	173	173
Crystal dimensions (mm)	0.05 × 0.03 × 0.03	0.08 × 0.08 × 0.05	0.05 × 0.04 × 0.03	0.08 × 0.04 × 0.04	0.11 × 0.11 × 0.06
Radiation	Graphite monochromated Mo $K\alpha$, λ = 0.71073 Å				
μ(Mo $K\alpha$) (mm^{-1})	16.66	19.02	26.88	16.92	27.22
Transmission factors	0.565–0.736	0.367–0.536	0.414–0.656	0.427–0.708	0.138–0.322
2θ limits	4.62–66.62°	4.72–66.30°	4.88–66.26°	4.62–66.60°	4.88–66.40°

Data collected	$-15 \le h \le 15$, $-15 \le k \le 15$, $-9 \le l \le 9$	$-15 \le h \le 15$, $-14 \le k \le 15$, $-9 \le l \le 9$	$-14 \le h \le 14$, $-14 \le k \le 14$, $-9 \le l \le 9$	$-15 \le h \le 15$, $-15 \le k \le 15$, $-9 \le l \le 9$	$-14 \le h \le 14$, $-14 \le k \le 14$, $-9 \le l \le 9$
No. of data collected	7861	7175	6929	7815	7073
No. of unique data, including $F_o^2 < 0$	1381 (R_{int} = 0.047)	1308 (R_{int} = 0.031)	1250 (R_{int} = 0.040)	1376 (R_{int} = 0.035)	1248 (R_{int} = 0.021)
No. of unique data, with $F_o^2 > 2\sigma(F_o^2)$	1263	1261	1181	1302	1244
No. of variables	39	39	39	39	39
Flack parameter	0.00(2)	0.00(2)	–0.01(2)	0.01(1)	0.07(5)
$R(F)$ for $F_o^2 > 2\sigma(F_o^2)$ [a]	0.019	0.018	0.018	0.015	0.045
$R_w(F_o^2)$ [b]	0.032	0.043	0.038	0.030	0.125
Goodness of fit	1.05	1.11	1.06	1.06	1.48
$(\Delta\rho)_{max}$, $(\Delta\rho)_{min}$ (e Å^{-3})	0.82, –0.90	1.40, –2.64	1.38, –0.99	0.91, –0.73	3.43, –3.73

[a] $R(F) = \sum||F_o| - |F_c|| / \sum|F_o|$ for $F_o^2 > 2\sigma(F_o^2)$.

[b] $R_w(F_o^2) = [\sum[w(F_o^2 - F_c^2)^2] / \sum wF_o^4]^{1/2}$; $w^{-1} = [\sigma^2(F_o^2) + (Ap)^2 + Bp]$, where $p = [\max(F_o^2,0) + 2F_c^2] / 3$.

Table 3-3 Positional and equivalent isotropic displacement parameters (Å^2) [a] for RE_3FeGaS_7 and RE_3CoGaS_7.

	La_3FeGaS_7	Pr_3FeGaS_7	Tb_3FeGaS_7	La_3CoGaS_7	Tb_3CoGaS_7
RE in 6*c* (*x*, *y*, *z*)					
x	0.37385(2)	0.37444(2)	0.37700(2)	0.37345(2)	0.37662(8)
y	0.23274(2)	0.22998(2)	0.22354(2)	0.23173(2)	0.22246(8)
z	0.28027(5)	0.20817(6)	0.18143(6)	0.22017(4)	0.3179(2)
U_{eq}	0.00783(5)	0.00859(6)	0.00727(6)	0.00727(4)	0.0073(2)
M in 2*a* (0, 0, *z*)					
z	0.0000(2)	0.0000(3)	0.0000(2)	0.00000(14)	0.0000(7)
U_{eq}	0.0121(2)	0.0204(3)	0.0104(2)	0.01002(15)	0.0090(7)
Ga in 2*b* (1/3, 2/3, *z*)					
z	0.36057(12)	0.12879(14)	0.10661(13)	0.13992(10)	0.3914(5)
U_{eq}	0.00791(14)	0.00730(15)	0.00653(16)	0.00738(11)	0.0057(5)
S1 in 6*c* (*x*, *y*, *z*)					
x	0.08860(10)	0.09295(12)	0.10207(12)	0.08846(8)	0.1015(5)

y	0.23305(10)	0.23657(12)	0.24040(12)	0.23069(8)	0.2382(5)
z	0.24431(15)	0.25530(18)	0.2587(2)	0.25830(12)	0.2383(7)
U_{eq}	0.00896(18)	0.0111(2)	0.00761(18)	0.00834(14)	0.0067(6)
S2 in 6*c* (*x*, *y*, *z*)					
x	0.51801(10)	0.51794(12)	0.52000(12)	0.51814(8)	0.5200(5)
y	0.09735(11)	0.09379(12)	0.08834(12)	0.09691(9)	0.0869(5)
z	0.00732(16)	0.47879(18)	0.44994(18)	0.49386(13)	0.0488(6)
U_{eq}	0.00823(17)	0.00806(18)	0.00698(18)	0.00749(13)	0.0056(6)
S3 in 2*b* (1/3, 2/3, *z*)					
z	0.9911(3)	0.4982(3)	0.4736(3)	0.5101(2)	0.0262(11)
U_{eq}	0.0079(3)	0.0070(3)	0.0064(3)	0.0075(2)	0.0061(11)

[a] U_{eq} is defined as one-third of the trace of the orthogonalized U_{ij} tensor.

Table 3-4 Selected interatomic distances (Å) in RE_3FeGaS_7 and RE_3CoGaS_7.

	La_3FeGaS_7	Pr_3FeGaS_7	Tb_3FeGaS_7	La_3CoGaS_7	Tb_3CoGaS_7
RE–S2	2.8649(10)	2.8250(11)	2.7641(11)	2.8674(8)	2.765(4)
RE–S1	2.9134(10)	2.8582(10)	2.7758(11)	2.9019(8)	2.769(4)
RE–S3	2.9143(9)	2.8585(8)	2.7518(9)	2.9103(7)	2.750(3)
RE–S1	2.9260(10)	2.8909(11)	2.8546(11)	2.9201(8)	2.843(4)
RE–S2	2.9625(10)	2.9178(11)	2.8428(11)	2.9607(8)	2.845(4)
RE–S2	3.0241(10)	2.9998(11)	2.9894(11)	3.0253(8)	2.986(4)
RE–S1	3.0630(11)	2.9849(11)	2.8254(13)	3.0519(8)	2.815(5)
RE–S1	3.4626(11)	3.5124(12)	3.7062(14)	3.4739(9)	3.721(5)
M–S1 (×3)	2.5429(12)	2.5350(14)	2.4956(13)	2.5121(9)	2.466(5)
M–S1 (×3)	2.5831(12)	2.5726(14)	2.5595(13)	2.5711(9)	2.552(5)
Ga–S3	2.2246(18)	2.2275(19)	2.239(2)	2.2243(14)	2.226(7)
Ga–S2 (×3)	2.2817(10)	2.2786(11)	2.2700(11)	2.2804(8)	2.278(4)

3.2.4 Ga XANES Analysis

Ga L-edge XANES spectra for a selection of $RE_3M\text{Ga}Ch_7$ compounds were collected on the high-resolution spherical grating monochromator undulator beamline (SGM, 11ID-1) at the Canadian Light Source (CLS) in Saskatoon, Saskatchewan. Finely ground samples were applied in a thin layer on spectroscopic grade carbon tape, mounted on a beamline-specific sample holder, and inserted into the vacuum chamber via a load lock. Spectra were collected from ~50 eV below to ~40 eV above the absorption edge to allow for normalization. Step sizes were 0.5 eV in the pre-edge region, 0.1 eV through the edge, and 0.25 eV in the post-edge region. Spectra were measured in both total fluorescence yield (TFY) and total electron yield (TEY) modes. However, only TFY spectra are presented here because they are less susceptible to surface effects and are significantly more intense than the TEY spectra. The latter advantage is especially important given that the signals were inherently weak, such that only the L_3-edge could be properly analyzed, the L_2-edge being subsumed into the post-edge normalization region. Individual sample plates held four samples and a reference standard of Zn metal, to which the spectra were calibrated with the maximum in the first derivative of its L_3-edge set to 1021.8 eV using the program Hephaestus.[41] All spectra were analyzed with the program Athena in the IFEFFIT software package.[41] On the basis of previous measurements on this beamline, we estimate a precision of 0.1 eV in the absorption edge energies.

3.2.5 Band structure calculations

Tight-binding linear muffin tin orbital band structure calculations were performed on La_3FeGaS_7 within the local density and atomic spheres approximation with use of the Stuttgart TB-LMTO-ASA program (version 4.7).[42] The basis set consisted of La 6s/6p/5d/4f, Fe 4s/4p/3d, Ga 4s/4p/4d, and S 3s/3p/3d orbitals, with the La 6p, Ga 4d, and S 3d orbitals being downfolded. Integrations in reciprocal space were carried out with an improved tetrahedron method over 208 irreducible *k* points within the first Brillouin zone.

3.3 Results and discussion

3.3.1 Structure

Six series of quaternary rare-earth chalcogenides, totalling 33 compounds, have been prepared, as listed in Table 3-1: RE_3FeGaS_7, RE_3CoGaS_7, RE_3NiGaS_7, $RE_3FeGaSe_7$, $RE_3CoGaSe_7$, and $RE_3NiGaSe_7$. Previously reported quaternary chalcogenides RE_3MGaCh_7 were limited to the Mn-containing series RE_3MnGaS_7 (*RE* = La–Nd, Sm, Gd), for which only unit cell parameters were determined for most members[3] and a single-crystal structure determination was performed by photographic methods on the La member,[43] and several members of the two Fe-containing series RE_3FeGaS_7 (*RE* = Nd, Sm, Gd, Dy) and $RE_3FeGaSe_7$ (*RE* = Nd, Gd, Dy).[29] The *RE* substitution has now been fully defined in RE_3FeGaS_7 to encompass a wide range (*RE* = La–Nd, Sm, Gd–Dy) and extended in $RE_3FeGaSe_7$ to the La member. The Co- and Ni-containing series are the newest representatives of quaternary chalcogenides RE_3MGaCh_7. Although the sulphide

series appear to be complete, more remains to be done to fully elucidate the selenide series, which are generally more difficult to prepare and somewhat less air-stable, consistent with past observations.[2]

The hexagonal structure of these compounds can be partitioned into two types of isolated chains, which extend along the *c*-direction, separated by the *RE* atoms (Figure 3-2). First, columns of confacial trigonal antiprisms develop along the 6_3 screw axes (coincident with the *c* axis) by stacking triangles of *Ch* atoms, which alternate in orientation. The *M* atoms reside at the centres of these trigonal antiprisms; the two inequivalent sets of *M*–*Ch* distances (×3) generally differ by less than 0.1 Å (Table 3-4) so that the coordination geometry can be described as more or less octahedral. Second, columns containing pairs of oppositely pointing tetrahedra develop along the threefold rotation axes (⅓, ⅔, *z* and ⅔, ⅓, *z*) by alternately stacking triangles and single atoms of *Ch*. The Ga atoms reside at the centres of every other tetrahedron such that all the filled tetrahedra point in the same direction, giving rise to the prominent feature of polarity in this noncentrosymmetric structure. The *RE* atoms each link three *Ch* atoms from a Ga-centred tetrahedron, three *Ch* atoms from a *M*-centred octahedron, and one *Ch* atom from a further Ga-centred tetrahedron in a monocapped trigonal prismatic geometry (CN7); an eighth *Ch* atom belonging to a *M*-centred octahedron is much farther (by 0.5 Å or more) and too distant to be bonding. The quaternary chalcogenides $RE_3MM'Ch_7$ are marked by considerable flexibility in the occupation of *M* atoms within the trigonal antiprisms. As the location of the *M* atom is displaced from the centre towards the triangular base of these antiprisms,

the coordination geometry can gradually change from octahedral (CN6), as is the case here, to the extreme of trigonal planar (CN3), as in all the Cu-containing representatives.[4] The former is properly designated to be an ordered $Ce_3Al_{1.67}S_7$-type structure, whereas the latter belongs to the La_3CuSiS_7-type structure.

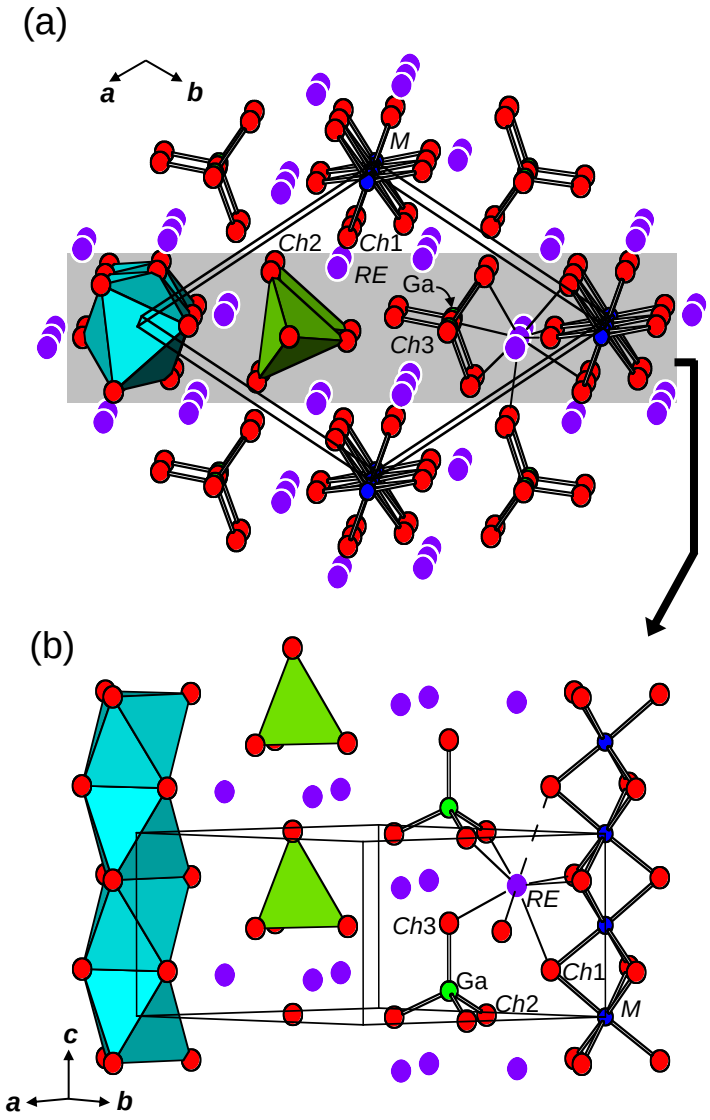

Figure 3-2 (a) Structure of RE_3MGaCh_7 (M = Fe, Co, Ni; Ch = S, Se) viewed along the c-direction. (b) A section viewed perpendicular to the c-direction, highlighting the parallel chains of M-centred octahedra and stacks of Ga-centred tetrahedra, separated by RE atoms.

Structural trends can be easily discerned within the three sulphide series RE_3MGaS$_7$ (M = Fe, Co, Ni), which are relatively extensive, through inspection of their cell parameters alone (Figure 3-3).

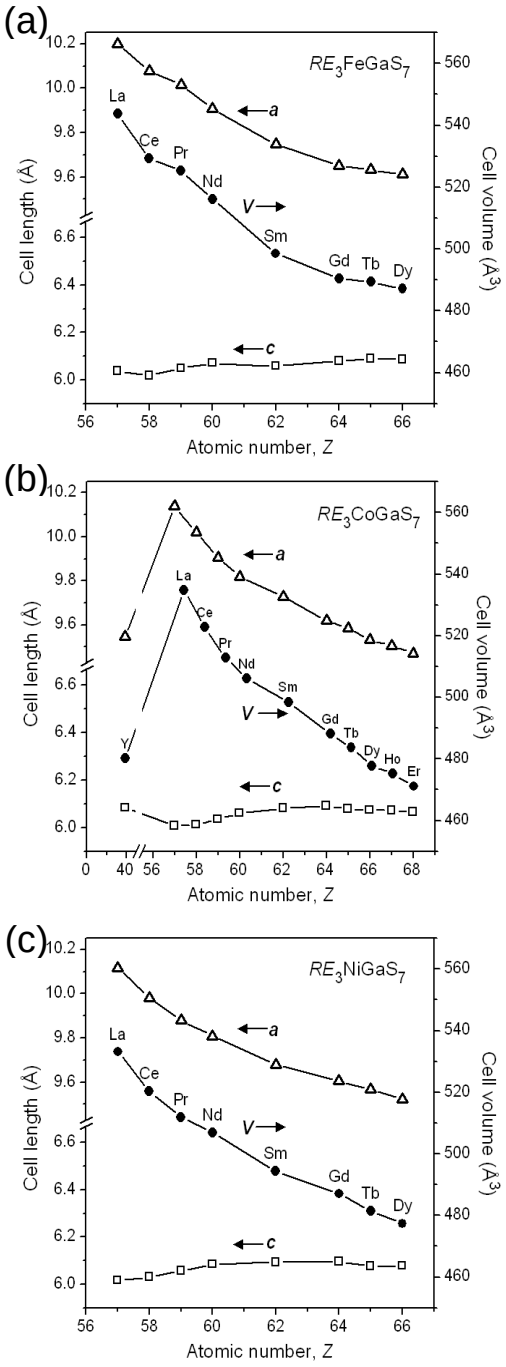

Figure 3-3 Plots of cell lengths and volumes for (a) RE_3FeGaS$_7$, (b) RE_3CoGaS$_7$, and (c) RE_3NiGaS$_7$.

These plots bear out many of the principles that have been developed for hexagonal $RE_3MM'Ch_7$ structures.[4] The most remarkable observation is that the gradual decrease in cell volume as smaller *RE* components are introduced, while itself a banal expectation, is controlled almost entirely by the decrease in the *a*-parameter. On the other hand, the *c*-parameter remains nearly constant; in fact, it tends to increase slightly on proceeding to the later *RE* members. These trends imply a strong anisotropy in which substitution with a smaller *RE* atom contracts the structure mostly within the *ab*-plane while the *c*-parameter is fixed by the choice of the *M′* component. Indeed, the value of the *c*-parameter (6.08±0.05 Å) expected for any Ga-containing sulphide representative of this series[4] matches very well with the observed values (Table 3-1). The combined effect of decreasing *a*-parameter and constant *c*-parameter is to increase the *c*/*a* ratio (Figure 3-4), the most prominent manifestation of which is the lengthening of the eighth *RE*–*Ch* contact noted above, as confirmed by comparing the *RE*–S distances in La_3FeGaS_7 (2.8649(10)–3.0630(11), 3.4626(11) Å) vs. Tb_3FeGaS_7 (2.7641(11)–2.8254(13), 3.7062(14) Å). The effect of substituting later transition-metal components *M* is more subtle. For a fixed *RE* component, the *c/a* ratio increases slightly in the progression *M* = Fe, Co, Ni. This, too, reflects a greater displacement of the *M* atoms away from the centre of the trigonal antiprisms that they occupy so that the coordination geometry becomes slightly more asymmetrical; cf., *M*–S distances in La_3FeGaS_7 (2.5429(12), 2.5831(12) Å) vs. La_3CoGaS_7 (2.5121(9), 2.5711(9) Å).

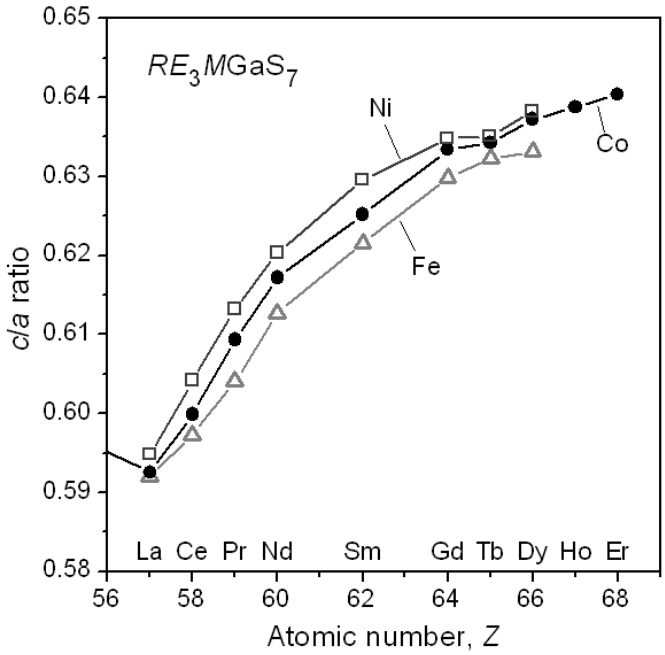

Figure 3-4 Plots of *c*/*a* ratios for RE_3MGaS$_7$ (M = Fe, Co, Ni).

3.3.2. Magnetic properties

These quaternary chalcogenides satisfy charge balance if the formulation $(RE^{3+})_3(M^{2+})(\mathrm{Ga}^{3+})(Ch^{2-})_7$ is accepted. Given the presence of isolated chains of face-sharing *M*-centred octahedra, separated by *RE* atoms, the magnetic properties are of potential interest. Zero-field-cooled magnetic susceptibility measurements were made on nearly all members of the series RE_3FeGaS$_7$ and RE_3CoGaS$_7$, as well as a few representative members of the series RE_3NiGaS$_7$ and RE_3MGaSe$_7$, as summarized in Table 3-5. Where applicable, the inverse magnetic susceptibility was fit to the Curie-Weiss law, $\chi = C / (T - \theta_p)$, in the linear portion of the high-temperature paramagnetic regime. Effective magnetic moments were evaluated from the Curie constant *C* and compared with theoretical values. If the free-ion values for both RE^{3+} and M^{2+} species are assumed, the theoretical

effective magnetic moment is given by $\mu_{eff} = \left(3\mu_{RE}^2 + \mu_M^2\right)^{1/2}$ per formula unit (f.u.). Néel temperatures were determined from plots of d(χT)/dT vs. T.

Table 3-5 Magnetic data for RE_3MGaQ_7 (M = Fe, Co, Ni; Q = S, Se).

Compound	Behaviour	θ_p (K)	$\mu_{eff,\ meas}$ (μ_B/f.u.)	$\mu_{eff,\ theor}$ (RE + M) (μ_B/f.u.)	$\mu_{eff,\ theor}$ (RE only) (μ_B/f.u.)	Remarks
La_3FeGaS_7	non-CW					TIP ~5×10^{-3} emu/mol
Ce_3FeGaS_7	non-CW					strong curvature in χ^{-1} vs. T
Pr_3FeGaS_7	paramagnetic	–24	7.6	7.9	6.2	
Nd_3FeGaS_7	paramagnetic	–42	7.7	8.0	6.3	
Sm_3FeGaS_7	non-CW					transition at 24 K
Gd_3FeGaS_7	paramagnetic	–20	15.2	14.6	13.8	
Tb_3FeGaS_7	antiferromagnetic	2	17.6	17.5	16.8	T_N = 15 K
Y_3CoGaS_7	non-CW					impurity at 120 K?
La_3CoGaS_7	non-CW					impurity at 6 K?
Ce_3CoGaS_7	non-CW	–108	6.5	5.9	4.4	parameters obtained by fitting above 100 K
Pr_3CoGaS_7	antiferromagnetic	–35	7.6	7.3	6.2	T_N < 2 K
Nd_3CoGaS_7	paramagnetic	–52	7.8	7.4	6.3	

Sm_3CoGaS_7	non-CW					impurity at 120 and 12 K?
Gd_3CoGaS_7	paramagnetic	–16	14.7	14.3	13.8	
Tb_3CoGaS_7	antiferromagnetic	–14	18.0	17.3	16.8	T_N = 3 K
Dy_3CoGaS_7	antiferromagnetic	6	19.2	18.8	18.4	T_N = 2 K
Ho_3CoGaS_7	paramagnetic	3	19.0	18.8	18.4	
Er_3CoGaS_7	antiferromagnetic	15	16.8	17.0	16.6	T_N = 3 K
Ce_3NiGaS_7	paramagnetic	–61	5.2	5.2	4.4	slight curvature in χ^{-1} vs. T
Tb_3NiGaS_7	paramagnetic	–15	17.4	17.1	16.8	hysteresis in M vs. H at 2 K; T_N = 4 K.
$Nd_3FeGaSe_7$	paramagnetic	–122	10.6	8.0	6.3	slight curvature in χ^{-1} vs. T
$Nd_3CoGaSe_7$	paramagnetic	–44	8.0	7.4	6.3	

In the series RE_3FeGaS_7, the magnetic properties can be divided into several types (Figure 3-5). The properties of La_3FeGaS_7 should serve as an important reference because it contains a non-magnetic *RE* component and thus any magnetism must originate from the Fe atoms. Surprisingly, its magnetic susceptibility is quite small and nearly temperature-independent, implying the absence of a localized moment on the Fe atoms. This behaviour is similar to La_3FeInS_7,[30] but contrasts with La_3FeAlS_7, which shows long-range

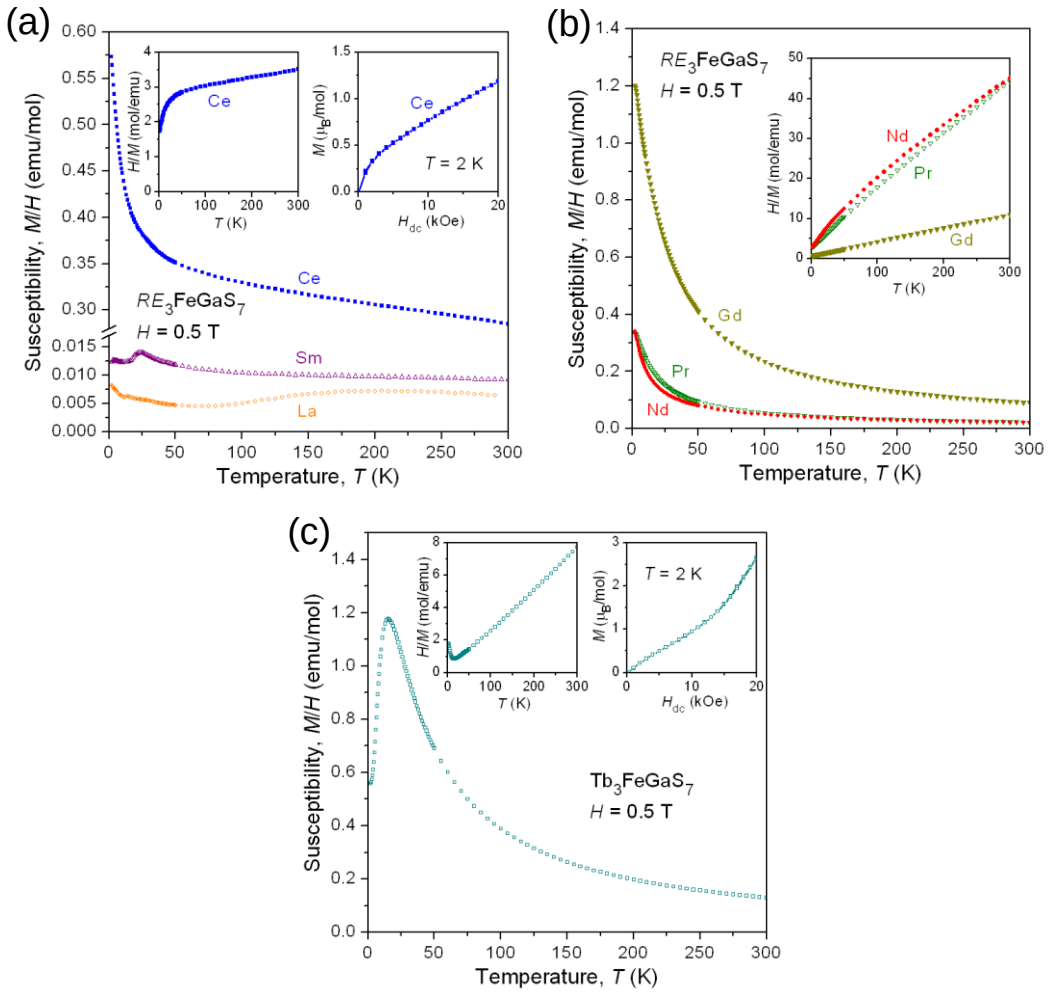

Figure 3-5 Magnetic properties of RE_3FeGaS_7: (a) *RE* = La, Ce, Sm; (b) *RE* = Pr, Nd, Gd; (c) *RE* = Tb.

antiferromagnetic ordering (T_N = 110 K) and a large effective magnetic moment (μ_{eff} = 5.65 μ_B/f.u.).[26] In Ce_3FeGaS_7, the inverse magnetic susceptibility is strongly nonlinear; the magnetization at 2 K shows significant curvature but does not reach saturation up to fields of 20 kOe. In Sm_3FeGaS_7, there appears to be a weak antiferromagnetic transition near 24 K, but the interpretation is made difficult by the presence of low-lying excited states associated with Sm^{3+} species. The Pr, Nd, and Gd members of RE_3FeGaS_7 exhibit normal paramagnetism, as revealed by the linear (or nearly so) behaviour of the inverse magnetic susceptibility over the entire temperature range from 2 to 300 K. Their effective magnetic moments are closer to theoretical values if contributions from both RE^{3+} and Fe^{2+} species are included (Table 3-5). Negative values for the Weiss constant θ_p for these three compounds suggest antiferromagnetic coupling interactions. Yin and co-workers have also previously measured magnetic properties for Gd_3FeGaS_7,[29] reproduced here, as well as Dy_3FeGaS_7; both were reported to exhibit paramagnetism with negative θ_p values and good agreement of the effective magnetic moments with theoretical values derived from RE^{3+} and Fe^{2+}. Tb_3FeGaS_7 clearly shows a downturn in its magnetic susceptibility, signaling long-range antiferromagnetic ordering taking place below a Néel temperature of 15 K. Its effective magnetic moment agrees well with expectations and the Weiss constant is slightly positive, θ_p = 2 K. The magnetization curve at 2 K is not linear but rather shows a kink near 13 kOe. These observations suggest a complicated magnetic ordering arrangement, possibly involving spin canting and field-dependent spin reorientation.

The trends in magnetic properties become more apparent in the RE_3CoGaS_7 series (Figure 3-6). Among the early *RE* members, Ce_3CoGaS_7 again exhibits distinctly nonlinear behaviour in its inverse magnetic susceptibility; fitting to the linear portion (above 100 K) leads to μ_{eff} of 6.5 μ_B/f.u., not too far off from the expected value (5.9 μ_B/f.u.). Paramagnetic Pr_3CoGaS_7 and Nd_3CoGaS_7 behave similarly to each other except that the former shows an incipient downturn in its magnetic susceptibility near 2 K. Their inverse magnetic

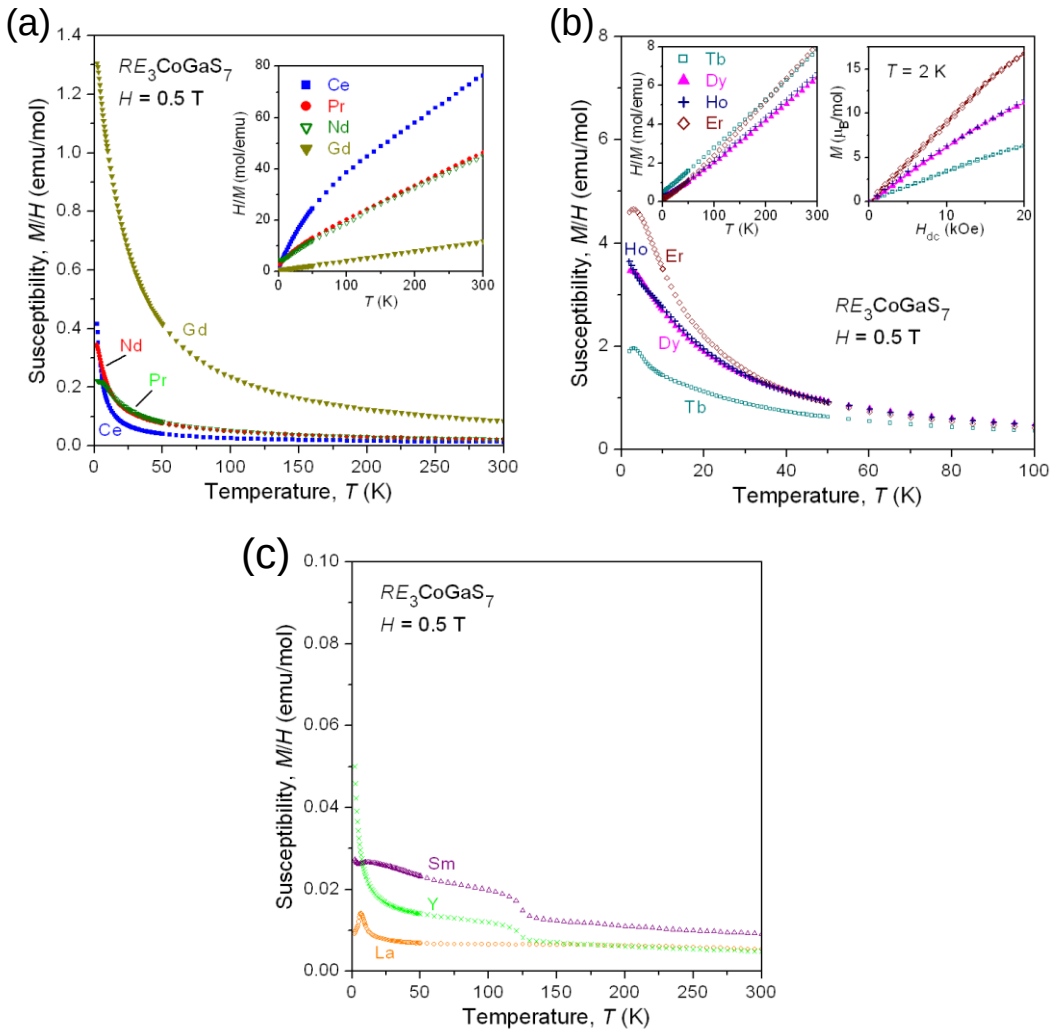

Figure 3-6 Magnetic properties of RE_3CoGaS_7: (a) *RE* = Ce, Pr, Nd, Gd; (b) *RE* = Tb, Dy, Ho, Er; (c) *RE* = Y, La, Sm.

susceptibility curves are strictly linear. On proceeding to the later *RE* members (Gd–Ho), the general trend is that a downturn in the magnetic susceptibility tends to emerge more visibly (T_N = 2–3 K for the Tb, Dy, and Er members) while the Weiss parameter evolves from small negative to small positive values. The Y, La, and Sm members are anomalous and show rather low magnetic susceptibility, much lower than would be expected on the basis of the contributions from Co^{2+} species alone. The kinks in the magnetic susceptibility curves likely originate from unidentified impurities.

The magnetic properties of an early and late *RE* member of the RE_3NiGaS_7 (*RE* = Ce, Tb) were examined (Figure 3-7a). The curvature in the inverse magnetic susceptibility is retained in the Ce member, but it is less pronounced than in Ce_3FeGaS_7 and Ce_3CoGaS_7. Long-range antiferromagnetic ordering is still observed in the Tb member (T_N = 4 K), similar to Tb_3FeGaS_7 and Tb_3CoGaS_7, but a prominent hysteresis in the magnetization curve at 2 K now becomes evident. The behaviour of the two selenides Nd_3MGaSe_7 (*M* = Fe, Co) (Figure 3-7b) does not change drastically from the corresponding sulphides, an observation that was also noted for RE_3FeGaS_7 vs. $RE_3FeGaSe_7$ (*RE* = Gd, Dy).[29] A structural expansion on proceeding from the sulphides to the selenides may be expected to lead to diminished magnetic coupling interactions. Thus, the Weiss parameter is less negative in $Nd_3CoGaSe_7$ (–44 K) than in Nd_3CoGaS_7 (–52 K). However, the trend is reversed for $Nd_3FeGaSe_7$ and Nd_3FeGaS_7, both of which show slight curvatures in their inverse magnetic susceptibility indicating that the Curie-Weiss fit may not be applicable.

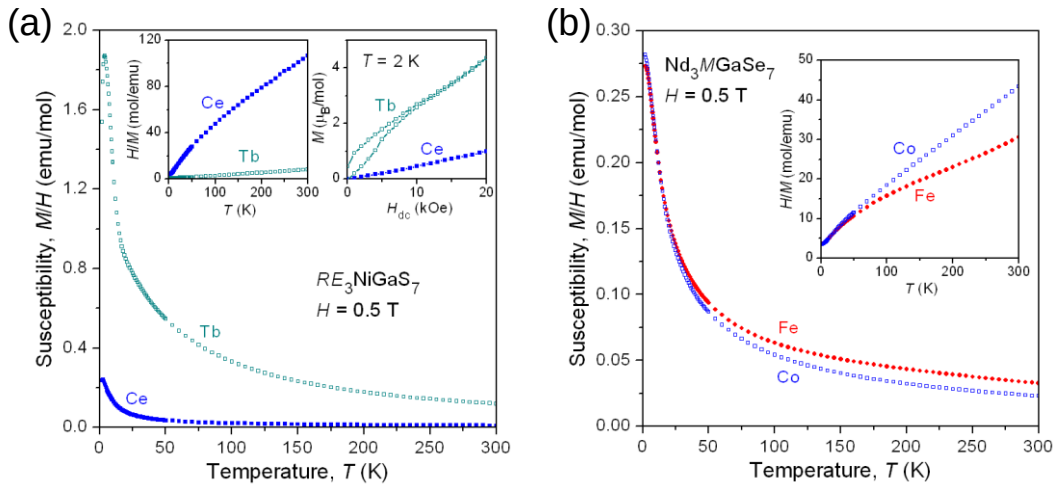

Figure 3-7 Magnetic properties of (a) RE_3NiGaS_7 (*RE* = Ce, Tb) and (b) Nd_3MGaSe_7 (*M* = Fe, Co).

3.3.3. Ga L-edge XANES

The magnetic measurements generally provide support for the presence of trivalent *RE* and divalent *M* atoms in the RE_3MGaCh_7 compounds, but are unable to probe the Ga atoms. It is of interest to examine the local electronic structure around the Ga atoms because the tetrahedra in which they reside are largely responsible for the noncentrosymmetry of the crystal structures. An appropriate technique is X-ray absorption spectroscopy of the Ga L-edge, which results from dipole-allowed electronic transitions from the spin-orbit-split $2p_{3/2}$ (L_3-edge) and $2p_{1/2}$ states (L_2-edge) to unoccupied 4s or 4d states in the conduction band. The absorption edge energies are sensitive to the local environment and can thus potentially give information about the Ga oxidation state.

Spectra of the Ga L-edge X-ray absorption near-edge structure (XANES) are shown for a series of four compounds (Tb_3CoGaS_7, Nd_3CoGaS_7, $Nd_3CoGaSe_7$, and $Nd_3FeGaSe_7$), chosen with the intention to identify any changes

as a result of substitution of the *RE*, *M*, or *Ch* component (Figure 3-8a). Given the low Ga concentrations in these compounds, only the more intense L_3-edge features could be examined here, the L_2-edge features being lost in the background noise at higher energy (beyond the scale shown). Remarkably few Ga L-edge spectra are available in the literature for comparison, and among these, there is disagreement on the assignment of the true absorption edge.[44–48] The two regions in the spectra in which a rapid increase in absorption most likely signals the occurrence of an absorption edge are marked A (1119–1120 eV) and B (1127 eV), while the feature marked A′ probably arises from EXAFS phenomena. Most earlier studies have typically assigned A as the L_3-edge, but this has been questioned in a more recent survey of diverse Ga salts in which A is interpreted instead as a pre-edge peak while B is assigned to be the true L_3-edge;[46] however, it is unclear what transition would then give rise to such a pre-edge peak. Shimizu and co-workers have examined Ga L-edge spectra for α-Ga_2O_3 (containing only octahedral Ga) and β-Ga_2O_3 (containing both octahedral and tetrahedral Ga).[44] They noted that feature A′ is absent and the intensity decreases smoothly to higher energy for α-Ga_2O_3, whereas feature A′ is present and is followed by further subtle undulations (indicative of EXAFS) for β-Ga_2O_3. The profiles in absorption L-edge spectra for Ga^{3+} and isoelectronic Zn^{2+} compounds also resemble each other.[47,48] To help identify the most likely final states in the transitions seen in the spectra for the quaternary chalcogenides, band structure calculations were performed on La_3FeGaS_7 in which the Ga 4d orbitals were not downfolded. Examining the Ga orbital contributions to the conduction band

(Figure 3-8b) reveals that there are unoccupied Ga 4d states found just above the Fermi level, followed by unoccupied Ga 4s states at 7–8 eV higher in energy, which matches the separation between features A and B in the observed spectra. Thus, we propose the interpretation that feature A is the absorption edge arising from the transition $2p_{3/2} \rightarrow 4d$, feature A′ is an EXAFS peak that is diagnostic of tetrahedral Ga species, and feature B is the absorption edge arising from the transition $2p_{3/2} \rightarrow 4s$. Accepting the assignment of feature A as the true absorption L_3-edge, we can now examine more closely how its energy changes among the four compounds Tb_3CoGaS_7, Nd_3CoGaS_7, $Nd_3CoGaSe_7$, and $Nd_3FeGaSe_7$. First, the absorption edge energies in these compounds are considerably higher (1119–1120 eV) than in elemental Ga (1116.4 eV),[41] confirming the presence of positively charged Ga species. The similarity of this energy to that in Ga_2O_3 (1120 eV)[44,46] supports the assignment of Ga^{3+}. Second, there is a resolvable difference in the absorption edge energies for the sulphides (Tb_3CoGaS_7 and Nd_3CoGaS_7, 1119.7–1119.8 eV) vs. the selenides ($Nd_3CoGaSe_7$ and $Nd_3FeGaSe_7$, 1119.2–1119.4 eV). The shift of ~0.4 eV to lower energy for the selenides implies greater covalent character in the *M*–Se bonds than in *M*–S bonds. This would be a reasonable expectation except that S and Se have nearly equal electronegativities in most typically used scales (e.g., 2.58 for S and 2.55 for Se in the Pauling scale;[49] or even reversed in order, 2.44 for S and 2.48 for Se in the Allred-Rochow scale).[50] However, as discussed in forthcoming chapters, other electronegativity scales may be more appropriate for the interpretation of X-ray spectra,[51] such as the spectroscopically derived Allen scale,[52] which places Se

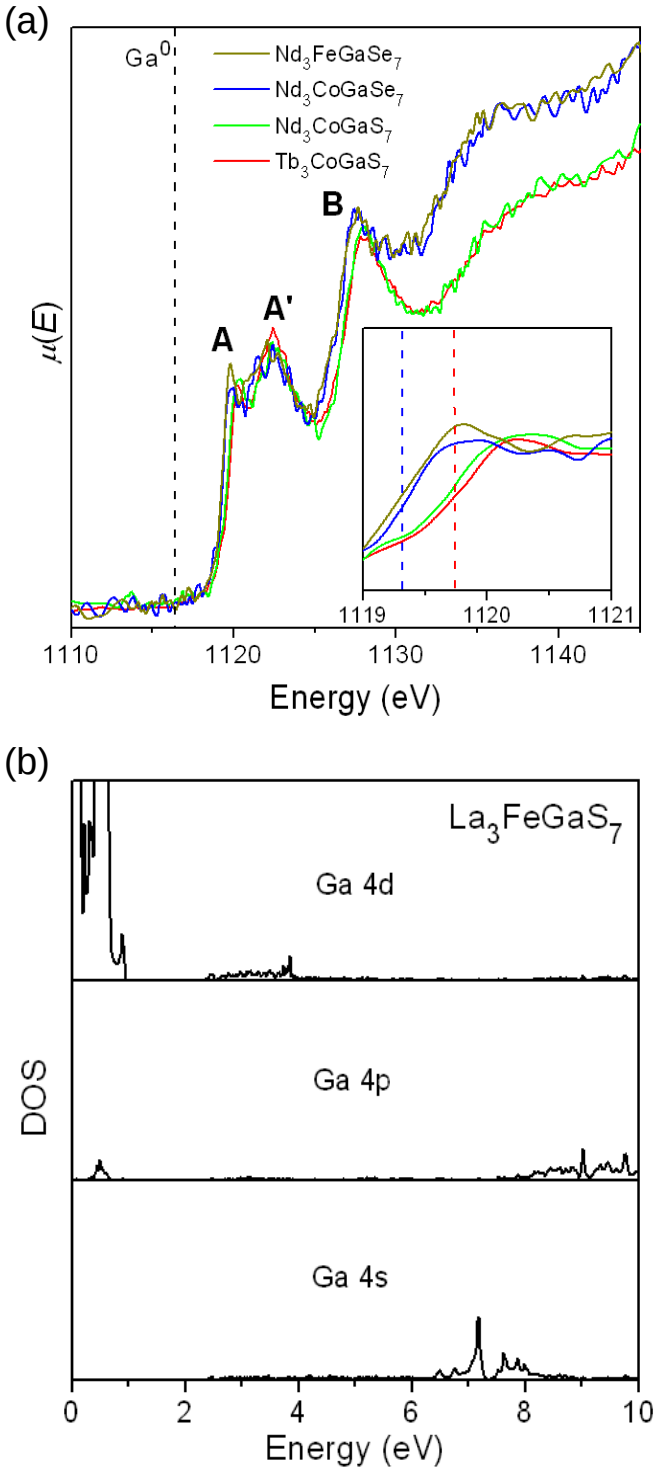

Figure 3-8 Ga L-edge XANES spectra for $Nd_3FeGaSe_7$, $Nd_3CoGaSe_7$, Nd_3CoGaS_7, and Tb_3CoGaS_7. Marked features are discussed in the text. The absorption edge energy for elemental Ga is shown by the vertical dashed line. The inset highlights differences in the absorption edge A for the selenide $Nd_3CoGaSe_7$ (blue dashed line) vs. the sulphide Tb_3CoGaS_7 (red dashed line).

with an intermediate electronegativity between S and Te and thus supports the observed shifts in absorption energy. In contrast to the noticeable effect of changing the *Ch* component on the Ga L-edge spectra, varying the *RE* component (Nd_3CoGaS_7 vs. Tb_3CoGaS_7) or the *M* component ($Nd_3FeGaSe_7$ vs. $Nd_3CoGaSe_7$) has virtually no effect. This is consistent with the crystallographic trends described earlier in which the geometry around the Ga-centred tetrahedra is little influenced by the *RE* or *M* components.

3.3.4. Band structure

The electronic band structure calculated for La_3FeGaS_7 reveals many features similar to that for La_3FeInS_7, discussed in Chapter 2.[30] The density of states (DOS) curve (Figure 3-9a) shows a valence band derived from mostly S 3p states mixing with Ga 4s/4p states from –6 to –1.5 eV and with Fe 3d states upwards to the Fermi level. Empty Fe 3d states are found just above the Fermi level up to 1 eV. There is barely a gap (<0.02 eV) separating the filled and empty Fe 3d states, which follow the pattern expected from a chain of face-sharing octahedra (filled 1a/1e bands and empty 2e bands that are the symmetry-lowered equivalents of the familiar t_{2g} and e_g crystal-field split orbitals for an octahedrally coordinated metal centre).[53] Beyond 1.5 eV above the Fermi level, a broad conduction band based on mostly empty La states is found. These calculations neglect the possibility of on-site electron-electron repulsions (Hubbard *U*); more accurate calculations on the corresponding selenides $RE_3FeGaSe_7$ (*RE* = Gd, Dy)

suggest that spin polarization takes place among the *RE* states and to a lesser extent among the Fe states, so that considerably larger energy gaps develop.[29]

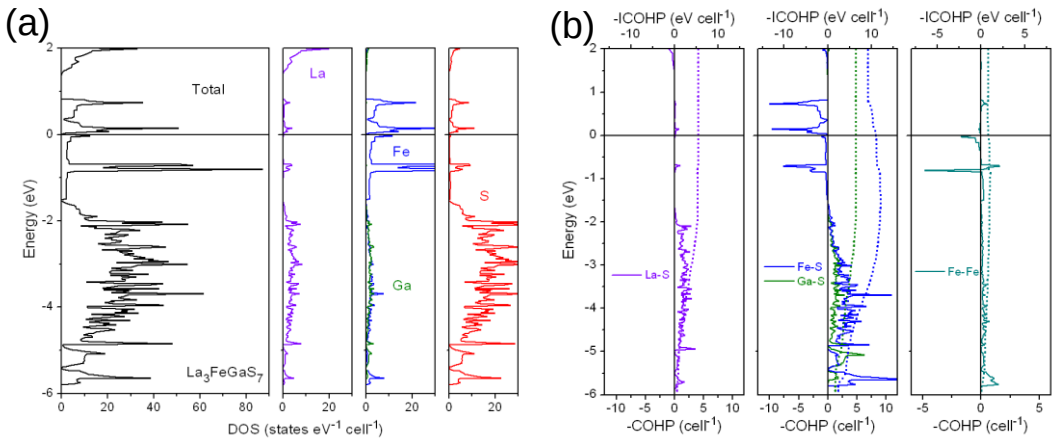

Figure 3-9 (a) Density of states (DOS) for La_3FeGaS_7 and atomic projections. (b) Crystal orbital Hamilton population (–COHP) curves (solid lines) and their integrations (–ICOHP, dotted lines). The Fermi level is at 0 eV.

Bonding interactions are evaluated by inspection of the crystal orbital Hamilton population (COHP) curves (Figure 3-9b). In agreement with the crystal structure description, the dominant contributions are provided by Fe–S (with an integrated COHP, or –ICOHP value of 1.8 eV/bond) and Ga–S (with –ICOHP of 1.6 eV/bond) bonding interactions from –6 to –1.5 eV; together they constitute 74% of the total bonding energy in La_3FeGaS_7. Direct metal-metal interactions within the chains of Fe-centred octahedra are quite small (–ICOHP of 0.4 eV/bond) and barely strengthened relative to the case in La_3FeInS_7 (0.3 eV/bond).[30] La–S interactions are small but non-negligible (–ICOHP of 0.7 eV/bond); the eighth long distance (3.4 Å) in the La coordination environment noted earlier is confirmed to be unimportant (–ICOHP of 0.1 eV/bond).

3.4 Conclusions

The versatility of the hexagonal quaternary chalcogenides $RE_3MM'Ch_7$ can be considerably expanded to many other II–III combinations of *M* and *M′*. The range of *RE* substitution is extensive in the sulphide series $RE_3M\mathrm{GaS}_7$ (*M* = Fe, Co, Ni), and remains to be further elucidated in the selenide series $RE_3M\mathrm{GaSe}_7$. These compounds are highly attractive for exploring structure-property relationships, because the structural features appear to follow predicted trends well (e.g., the *a*-parameter is mostly controlled by the choice of the *RE* component, while the *c*-parameter is largely fixed by the choice of the tetrahedral geometry $M'Ch_4$) and the presence of low-dimensional chains of transition-metal-centred octahedra separated by *RE* atoms may be conducive for understanding magnetic properties. Ga L-edge XANES spectra have been analyzed to confirm the presence of cationic Ga atoms in these compounds. Information presented in this chapter, as well as Chapter 2, suggest that there is little interplay between the cations of these materials, leaving the chains of octahedra and tetrahedra effectively isolated. It is of interest to extend this work to higher dimensional systems such as the 2D oxychalcogenides to investigate the degree of charge transfer between layers.

3.5 References

[1] M. Guittard, M. Julien-Pouzol, P. Laruelle, J. Flahaut, C. R. Acad. Sci., Ser. C 267 (1968) 767–769.

[2] M. Guittard, M. Julien-Pouzol, Bull. Soc. Chim. Fr. (1970) 2467–2469.

[3] G. Collin, J. Flahaut, Bull. Soc. Chim. Fr. (1972) 2207–2209.

[4] G. Collin, J. Étienne, J. Flahaut, M. Guittard, P. Laruelle, Rev. Chim. Miner. 10 (1973) 225–238.

[5] S.-J. Hwu, C.K. Bucher, J.D. Carpenter, S.P. Taylor, Inorg. Chem. 34 (1995) 1979–1980.

[6] S.-H. Lin, J.-G. Mao, G.-C. Guo, J.-S Huang, J. Alloys Compd. 252 (1997) L8–L11.

[7] F.Q. Huang, J.A. Ibers, Acta Crystallogr., Sect. C 55 (1999) 1210–1212.

[8] K.M. Poduska, F.J. DiSalvo, K. Min, P.S. Halasyamani, J. Alloys Compd. 335 (2002) L5–L9.

[9] M. Daszkiewicz, L.D. Gulay, A. Pietraszko, V.Ya. Shemet, J. Solid State Chem. 180 (2007) 2053–2060.

[10] L.D. Gulay, V.Ya. Shemet, I.D. Olekseyuk, J. Alloys Compd. 385 (2004) 160–168.

[11] L.-B. Wu, F.-Q. Huang, Z. Kristallogr. – New Cryst. Struct. 220 (2005) 307–308.

[12] L.D. Gulay, D. Kaczorowski, A. Pietraszko, J. Alloys Compd. 403 (2005) 49–52.

[13] L.D. Gulay, I.D. Olekseyuk, J. Alloys Compd. 388 (2005) 274–278.

[14] L.D. Gulay, O.S. Lychmanyuk, J. Stępień-Damm, A. Pietraszko, I.D. Olekseyuk, J. Alloys Compd. 402 (2005) 201–203.

[15] L.D. Gulay, V.Ya. Shemet, I.D. Olekseyuk, J. Alloys Compd. 388 (2005) 59–64.

[16] L.D. Gulay, I.D. Olekseyuk, M. Wolcyrz, J. Stępień-Damm, Z. Anorg. Allg. Chem. 631 (2005) 1919–1923.

[17] L.D. Gulay, O.S. Lychmanyuk, M. Wolcyrz, A. Pietraszko, I.D. Olekseyuk, J. Alloys Compd. 425 (2006) 159–163.

[18] L.D. Gulay, O.S. Lychmanyuk, I.D. Olekseyuk, A. Pietraszko, J. Alloys Compd. 422 (2006) 203–207.

[19] L.D. Gulay, O.S. Lychmanyuk, J. Stępień-Damm, A. Pietraszko, I.D. Olekseyuk, J. Alloys Compd. 414 (2006) 113–117.

[20] O.S. Lychmanyuk, L.D. Gulay, I.D. Olekseyuk, Pol. J. Chem. 80 (2006) 463–469.

[21] I. Hartenbach, A.C. Müller, T. Schleid, Z. Anorg. Allg. Chem. 632 (2006) 2147.

[22] L.D. Gulay, O.S. Lychmanyuk, I.D. Olekseyuk, M. Daszkiewicz, J. Stępień-Damm, A. Pietraszko, J. Alloys Compd. 431 (2007) 185–190.

[23] O.S. Lychmanyuk, L.D. Gulay, I.D. Olekseyuk, J. Stępień-Damm, M. Daszkiewicz, A. Pietraszko, Pol. J. Chem. 81 (2007) 353–367.

[24] O.M. Strok, M. Daszkiewicz, L.D. Gulay, D. Kaczorowski, J. Alloys Compd. 493 (2010) 47–49.

[25] G. Collin, J. Flahaut, C. R. Acad. Sci., Ser. C 270 (1970) 488–490.

[26] K.S. Nanjundaswamy, J. Gopalakrishnan, J. Solid State Chem. 49 (1983) 51–58.

[27] P.M. Van Calcar, P.K. Dorhout, Mater. Sci. Forum 315 (1999) 322–330.

[28] L.-B. Wu, F.-Q. Huang, Z. Kristallogr. – New Cryst. Struct. 220 (2005) 305–306.

[29] W. Yin, W. Wang, L. Kang, Z. Lin, K. Feng, Y. Shi, W. Hao, J. Yao, Y. Wu, J. Solid State Chem. 202 (2013) 269–275.

[30] B.W. Rudyk, S.S. Stoyko, A. Mar, J. Solid State Chem., submitted.

[31] M. Patrie, M. Guittard, C. R. Acad. Sci., Ser. C 268 (1969) 1136–1138.

[32] G. Collin, P. Laruelle, C. R. Acad. Sci., Ser. C 270 (1970) 410–412.

[33] R.L. Gitzendanner, C.M. Spencer, F.J. DiSalvo, M.A. Pell, J.A. Ibers, J. Solid State Chem. 131 (1996) 399–404.

[34] M.R. Huch, L.D. Gulay, I.D. Olekseyuk, J. Alloys Compd. 424 (2006) 114–118.

[35] S.-P. Guo, G.-C. Guo, M.-S. Wang, J.-P. Zou, G. Xu, G.-J. Wang, X.-F. Long, J.-S. Huang, Inorg. Chem. 48 (2009) 7059–7065.

[36] M. Daszkiewicz, L.D. Gulay, Mater. Res. Bull. 47 (2012) 497–499.

[37] S.C. Abrahams, Acta Crystallogr., Sect. B 46 (1990) 311–324.

[38] I. Hartenbach, T. Nilges, T. Schleid, Z. Anorg. Allg. Chem. 633 (2007) 2445–2452.

[39] G.M. Sheldrick, SHELXTL, version 6.12, Bruker AXS Inc., Madison, WI, 2001.

[40] L.M. Gelato, E. Parthé, J. Appl. Crystallogr. 20 (1987) 139–143.

[41] B. Ravel, M. Newville, J. Synchrotron Radiat. 12 (2005) 537–541.

[42] R. Tank, O. Jepsen, A. Burkhardt, O.K. Andersen, TB-LMTO-ASA Program, version 4.7, Max Planck Institut für Festkörperforschung, Stuttgart, Germany, 1998.

[43] N. Rodier, M. Guittard, J. Flahaut, C. R. Acad. Sci., Ser. 2, 296 (1983) 65–70.

[44] K.-I. Shimizu, M. Takamatsu, K. Nishi, H. Yoshida, A. Satsuma, T. Hattori, Chem. Commun. (1996) 1827–1828.

[45] X.T. Zhou, F. Heigl, J.Y.P. Ko, M.W. Murphy, J.G. Zhou, T. Regier, R.I.R. Blyth, T.K. Sham, Phys. Rev. B 75 (2007) 125303-1–125303-8.

[46] K.R. Ball, P.M. Dowling, T.K. Sham, T. Regier, R.I.R. Blyth, J. Thompson, Canadian Light Source Activity Report (2007) 124–125.

[47] W.-Q. Han, M.J. Ward, T.K. Sham, J. Phys. Chem. C 115 (2011) 3962–3967.

[48] M.J. Ward, W.-Q. Han, T.K. Sham, J. Phys. Chem. C 115 (2011) 20507–20514.

[49] L.R. Murphy, T.L. Meek, A.L. Allred, L.C. Allen, J. Phys. Chem. A 104 (2000) 5867–5871.

[50] A.L. Allred, E.G. Rochow, J. Inorg. Nucl. Chem. 5 (1958) 264–268.

[51] B.W. Rudyk, P.E.R. Blanchard, R.G. Cavell, A. Mar, J. Solid State Chem. 184 (2011) 1649–1654.

[52] L.C. Allen, J. Am. Chem. Soc. 111 (1989) 9003–9014.

[53] M.-H. Whangbo, M.J. Foshee, R. Hoffman, Inorg. Chem. 19 (1980) 1723–1728.

Chapter 4

Electronic structure of lanthanum copper oxychalcogenides LaCuO*Ch* (*Ch* = S, Se, Te) by X-ray photoelectron and absorption spectroscopy[1]

4.1 Introduction

Most representatives of the tetragonal ZrCuSiAs-type structure, discussed in Chapter 1, fall into two categories:[1,2] (i) rare-earth transition-metal oxypnictides *REMPn*O (*Pn* = P, As), which are now zealously investigated as new superconductors,[3–7] and (ii) rare-earth copper oxychalcogenides *RE*CuO*Ch* (*Ch* = S, Se, Te), which have been identified as transparent p-type semiconductors.[8–15] (Here the formulas have been written according to the most common way they are found in the literature, even though the rules for element ordering are inconsistent.) In both cases, the physical properties derive from the partitioning of this structure into conducting [*MPn*] or [Cu*Ch*] layers interleaved with insulating [*RE*O] layers, a configuration that has been aptly described as a "multiple quantum well" (MQW) (Figure 4-1).[13] The electronic interplay between the alternately stacked layers presents attractive opportunities to modify properties, such as the magnitude of the band gap in the oxychalcogenides, through appropriate chemical substitutions. Interestingly, the markedly two-

[1] *A version of this chapter has been published. B.W Rudyk, P.E.R. Blanchard, R.G. Cavell, A. Mar, J. Solid State Chem. 184 (2011) 1649–1654. Copyright (2011) by Elsevier.*

dimensional character of the oxypnictides and oxychalcogenides does not extend to the eponymous compound ZrCuSiAs itself (as well as ZrCuSiP and HfCuSiAs),

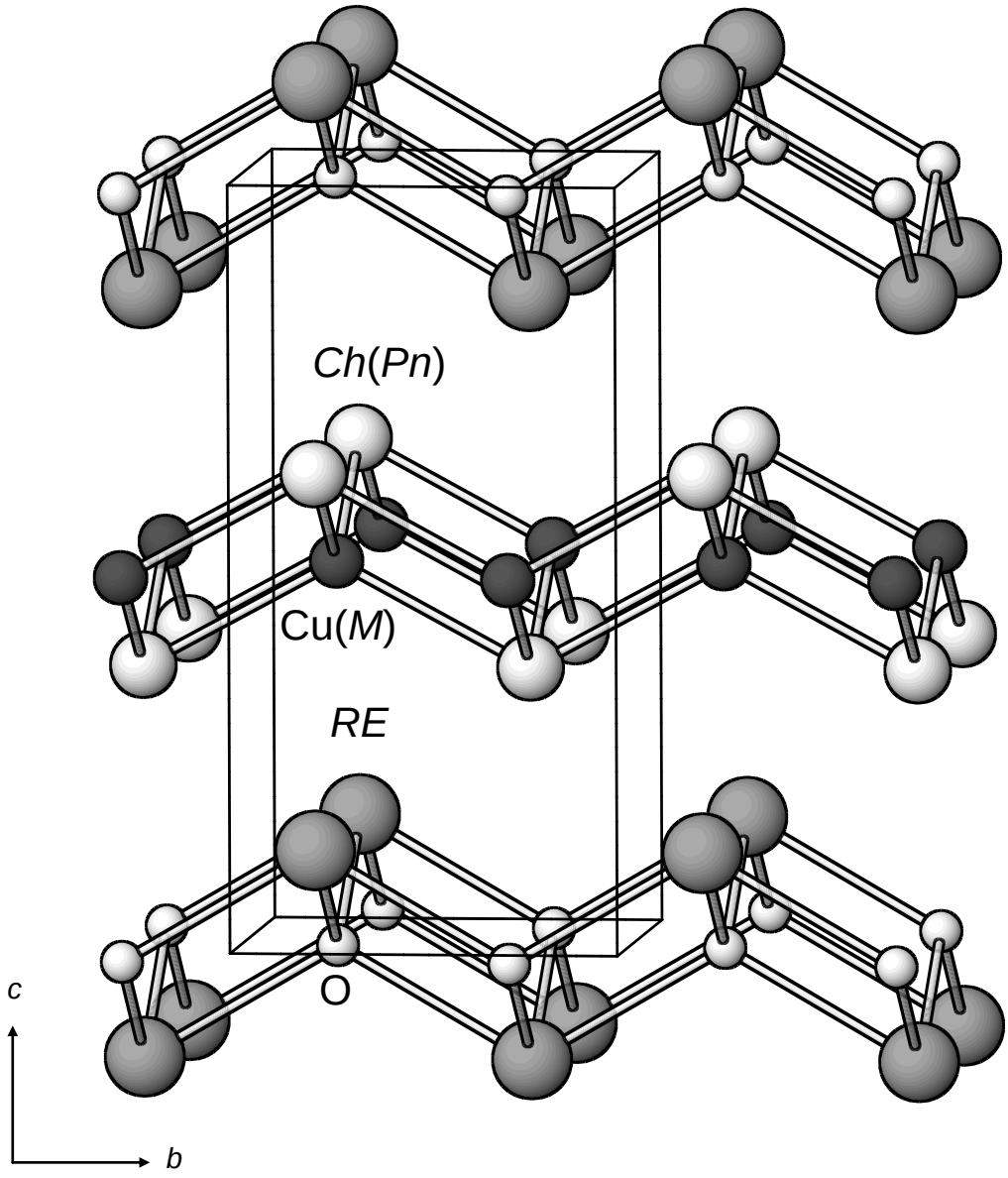

Figure 4-1 Crystal structure of *RE*CuO*Ch* (*Ch* = S, Se, Te) (or *REMPn*O (*Pn* = P, As)) in terms of alternating [*RE*O] and [Cu*Ch*] (or [*MPn*]) layers stacked along the *c* direction.

which exhibits strongly three-dimensional character as covalent Zr–As bonds form between the nominal [ZrSi] and [CuAs] layers.[16,17]

We have previously applied X-ray photoelectron spectroscopy (XPS) and X-ray absorption near-edge spectroscopy (XANES) to monitor the changes in electronic structure upon chemical substitution in *REM*AsO and ZrCuSi*Pn*.[18–20] The small shifts in binding energy (BE) and absorption-edge energy in highly covalent systems such as these can now be routinely detected through the improved resolution available in modern XPS instrumentation and through the high source intensity associated with use of synchrotron radiation. From these studies, we have been able to correlate, for example, trends in the As BE with the difference in electronegativity in *M*–As bonds as *M* is altered in *REM*AsO, and trends in the Zr absorption-edge energy with the Zr-to-*Pn* charge transfer as *Pn* is altered in ZrCuSi*Pn*. In continuation of these studies on the electronic structure of ZrCuSiAs-type compounds, we present here an analysis of the high-resolution XPS core-line spectra and Cu absorption-edge spectra of LaCuO*Ch* (*Ch* = S, Se, Te). These results complement previous measurements of the valence and conduction band spectra of LaCuO*Ch*, obtained by Ueda and co-workers through photoemission and inverse photoemission spectroscopy,[9,10,21] and of the *RE* 4f and O 2p partial densities of states of *RE*CuOS, obtained by Sato and co-workers through resonant photoemission spectroscopy.[22] In particular, the questions that we wish to address include how substitution of *Ch* affects the electronic structure in LaCuO*Ch* and how the BE shifts of the *Ch* atoms relate to the degree of electron transfer experienced within the [Cu*Ch*] layers.

4.2 Experimental

4.2.1 Synthesis

Reagents in the form of pieces (La) or powders (La_2O_3, Cu, S, Se, Te) with purities of 99.5% or better were obtained from Cerac, Aldrich, or Alfa-Aesar. For LaCuOS and LaCuOTe, mixtures of La, La_2O_3, Cu, and *Ch* in a 1:1:3:3 ratio were placed in evacuated fused-silica tubes, which were sealed and heated at 1050 °C for 1–2 weeks, followed by quenching in water. Minor amounts of other phases, such La_2O_2S or La_2O_2Te, were detected after this initial heat treatment, presumably because of incomplete reaction, but they were readily eliminated after regrinding and reheating for an additional week. For LaCuOSe, this procedure could not lead to a sufficiently pure product to our satisfaction; instead, a more effective procedure was to react a mixture of La_2O_3, La_2Se_3 (prepared from stoichiometric reaction of La and Se at 900 °C for 1 week), Cu, and Se in a 2:1:6:3 ratio at 1050 °C for 10 d. All samples used for the spectroscopy measurements were phase-pure according to their powder X-ray diffraction patterns, collected on an Inel powder diffractometer (Figure A2-1 in Appendix 2).

4.2.2 XPS analysis

XPS spectra were measured on a Kratos AXIS 165 spectrometer equipped with a monochromatic Al Kα X-ray source (14 mA, 15 kV) and a hybrid lens with a spot size of 700 × 400 μm^2. The air-stable samples were finely ground, pressed into In foil, mounted on a Cu sample holder with carbon tape, and

transferred in a sealed container to the analysis chamber of the spectrometer. The pressure inside the XPS instrument was maintained between 10^{-7} and 10^{-9} Pa. Samples were sputter-cleaned with an Ar^+ ion beam (4 kV, 10 mA) until no further changes were observed in the peak shoulders associated with surface oxides, which could not be completely removed. Core-line BEs were, within standard uncertainties, the same before and after the sputtering procedure. Survey spectra (collected with pass energy of 160 eV, step size of 0.7 eV, and sweep time of 180 s) in the range of 0 to 1100 eV confirmed the presence of all elements in the expected compositions. High-resolution spectra (collected with pass energy of 20 eV, step size of 0.05 eV, and sweep time of 180 s) were measured in the appropriate BE ranges as determined from the survey scan for the La 3d, Cu 2p, O 1s, and chalcogen (S 2p; Se 3s, 3p, 3d; Te 3p, 3d, 4d) core lines. Additional core-line spectra were measured for elemental Se and Te chosen as standards. Charge neutralization was determined to be unnecessary. The spectra were calibrated to the C 1s line at 284.8 eV arising from adventitious carbon and were analyzed with use of the CasaXPS software package.[23] The background arising from energy loss was removed by applying a Shirley-type function and the peaks were fitted to pseudo-Voigt (70% Gaussian and 30% Lorentzian) line profiles to take into account spectrometer and lifetime broadening effects. On the basis of many previous measurements on this instrument, we estimate a precision of better than ±0.1 eV in the BEs.

4.2.3 Cu XANES analysis

Cu L-edge spectra were measured on the high-resolution spherical grating monochromator undulator beamline (SGM, 11ID-1) and Cu M-edge spectra were measured on the variable line spacing plane grating monochromator beamline (VLS PGM, 11ID-2), both at the Canadian Light Source (CLS) in Saskatoon, Saskatchewan. Finely ground samples were mounted in a thin layer on carbon tape to the sample holder and inserted into the vacuum chamber via a load lock. Spectra were collected from ~15 eV below to ~30–40 eV above the edge to allow for normalization. For the Cu L-edge spectra, the step sizes were 0.5 eV in the pre- and post-edge regions and 0.1 eV through the edge; for the Cu M-edge spectra, the step sizes were decreased to 0.2 eV in the pre- and post-edge regions and 0.05 eV through the edge because of the lower X-ray intensity available in the PGM beamline. Although both total electron yield (TEY) and total X-ray fluorescence yield (TFY) modes were used, we present only the TFY spectra because they suffer less from surface effects and are more intense than the TEY spectra. With use of the program Hephaestus, these spectra were calibrated to Cu metal, with the maxima in the first derivatives set to 932.7 eV (L_3-edge) and 75.1 eV (M_3-edge); these spectra were analyzed with use of the program Athena in the Ifeffit software package.[24] On the basis of previous measurements, we estimate a precision of ±0.1 eV for the absorption edge energies.

4.2.4 Band structure calculations

Although tight-binding linear muffin tin orbital (TB-LMTO) band structure calculations have been previously conducted on LaCuO*Ch* (*Ch* = S, Se, Te), the crystal orbital Hamilton populations (COHP) were not reported.[25] We have repeated these calculations, with integrations carried out over 84 independent *k* points in the first Brillouin zone, to permit comparisons of integrated COHP values (–ICOHP) to LaNiAsO and ZrCuSiAs (Table A2-1 in Appendix 2.[26] The density of states (DOS) and crystal orbital Hamilton population (COHP) curves are provided in Figure A4-2 in Appendix 2.

4.3 Results and discussion

4.3.1 [LaO] layer

The La 3d spectra are similar for all members of LaCuO*Ch* (*Ch* = S, Se, Te), with essentially identical BEs of 834.3 eV for the $3d_{5/2}$ core line (Figure 4-2) and 851.1 eV for the $3d_{3/2}$ core line (not shown). Although the La $3d_{5/2}$ BE is higher than in La_2O_3 (831.9 eV) and close to those in La*M*AsO (*M* = Fe, Co, Ni; 834.8 eV),[18] BE shifts of lanthanide atoms are not straightforward to interpret because they are quite sensitive to final-state effects and coordination environments.[27–29] The appearance of satellite peaks at 4 eV to the higher energy side of each of the core-line peaks is a diagnostic feature for La^{3+} species coordinated by other ligands (in contrast to the spectrum of La metal, which lacks these satellites) and is generally attributed to a ligand-to-metal shake-up process.[30–32] (Similar satellites are found

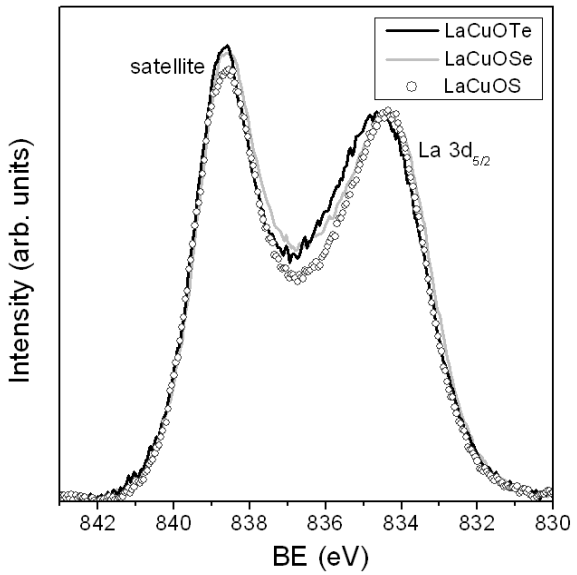

Figure 4-2 La $3d_{5/2}$ XPS spectra for LaCuO*Ch* (*Ch* = S, Se, Te) normalized to the core-line peak to highlight intensity changes in the satellite peak.

in La_2O_3,[18] but for the same reasons as above, i.e., different coordination environments and final state effects, they cannot be directly compared to those found in LaCuO*Ch*.) When an electron is ejected after photoexcitation takes place, ligand-based valence electrons are promoted into La-based conduction states that are drawn lower in energy (below the Fermi level) by the core-hole. Although these satellites, induced by final-state effects, might be considered a nuisance, they do provide useful information. Their relative intensities depend on the degree of overlap between orbitals on the metal (La) and ligand atoms (O and *Ch*, at distances of 2.36–2.40 Å and 3.26–3.49 Å, respectively).[27–29] When the spectra for LaCuO*Ch* are normalized to the La $3d_{5/2}$ core-line peak, the satellite peak becomes slightly more intense on progressing from LaCuOS to LaCuOSe and LaCuOTe (Figure 4-2). Given that the O 1s spectra are invariant in this series

(as presented shortly below), the change in the satellite intensity may be attributed to weak interactions of the La atoms in the [LaO] layer with more distant *Ch* atoms in the adjacent [Cu*Ch*] layer. The trend suggests that orbital overlap is more effective between La atoms and larger *Ch* atoms. LMTO calculations support this proposal, as seen in –ICOHP values for the La–*Ch* contacts of 0.11 eV/bond (3.26 Å) in LaCuOS, 0.13 eV/bond (3.33 Å) in LaCuOSe, and 0.17 eV bond (3.48 Å) in LaCuOTe. Of the competing factors that affect the degree of orbital overlap, the better matching of size and energy between La and larger *Ch* atoms overcomes their greater separation. The enhanced screening brought on by this more effective orbital overlap favours the promotion of *Ch*-based valence electrons to La-based conduction states in the ligand-to-metal shake-up process, increasing the cross-section and thus the intensity of the satellite peak.[33,34]

The O 1s spectra have similar lineshapes and BEs in LaCuO*Ch* (Figure 4-3). (The Ar^+ sputtering procedure reduced but could not remove all the surface oxides responsible for the peaks at higher BE; it did not affect the position and lineshape of the core-line peaks, which have a FWHM of 1.2–1.3 eV.) The O 1s BEs (529.5 eV for LaCuOS and LaCuOSe; 529.7 eV for LaCuOTe) are higher than in La_2O_3 (528.8 eV)[27] but slightly lower than in La*M*AsO (529.9 eV),[18] indicating that the degree of ionic character in the La–O bonds in LaCuO*Ch* is intermediate between "very ionic" in La_2O_3 and "normal ionic" in La*M*AsO, if Barr's classification scheme is accepted.[35,36] The combined analysis of the La 3d

and O 1s spectra provides evidence that weak La–*Ch* interactions exist between the nominally isolated [LaO] and [Cu*Ch*] layers, but they have little influence on the O atoms.

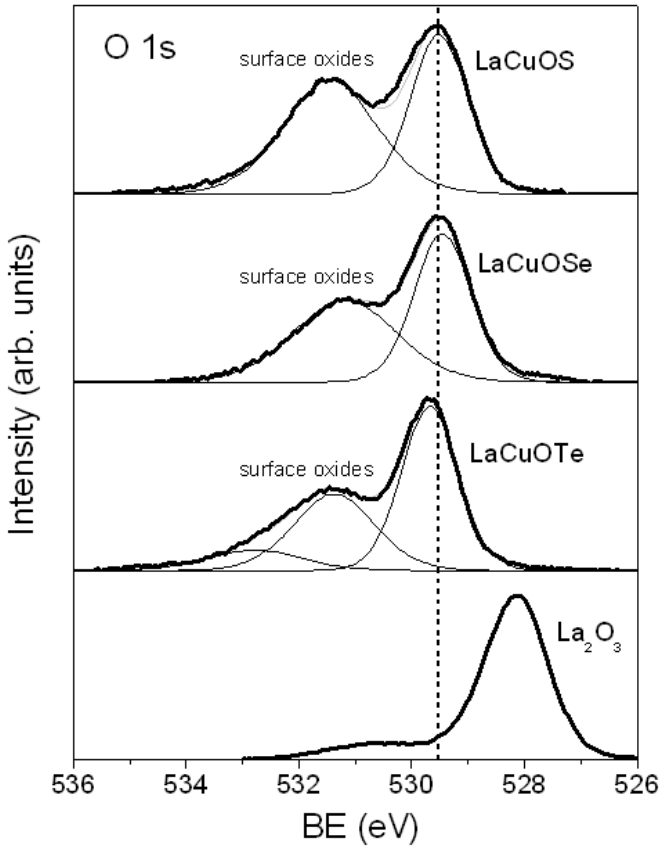

Figure 4-3 Comparison of O 1s XPS spectra for LaCuO*Ch* (*Ch* = S, Se, Te), with the BE of 529.5–529.7 eV marked by the dashed vertical line, and La_2O_3.

4.3.2 [Cu*Ch*] layer

Although the [Cu*Ch*] layer may be expected to be more sensitive to changes in *Ch*, the Cu 2p spectra are essentially identical for all members of the LaCuO*Ch* series (Figure 4-4). No significant shifts are observed in the Cu $2p_{3/2}$ core-line peaks, for which the BEs of 932.7–932.9 eV are typical for Cu^{1+} and are

lower than for most Cu^{2+} systems (>933.5 eV).[37–39] However, the Cu $2p_{3/2}$ BE is not a reliable diagnostic for the Cu oxidation state; there are many compounds that cannot be distinguished this way (e.g., CuS and Cu_2S have identical BEs) [40] and, in fact, Cu metal has a similar BE of 932.7 eV.[41] Stronger evidence for the presence of Cu^+ is gained from the FWHM of 1.0–1.2 eV (similar to that in CuBr and CuI,[42,43] but smaller than ~3 eV in CuO[39]) and the absence of a shake-up or shake-down satellite peak at the high-energy side of the $2p_{3/2}$ core-line that is characteristic of Cu^{2+} systems,[44–47] as seen in CuO, for example (Figure 4-4). The symmetric lineshape of the Cu $2p_{3/2}$ core-line peaks is consistent with the semiconducting behaviour of these compounds. It has also been well-established that examination of the absolute shifts in the Cu $L_3M_{4,5}M_{4,5}$ Auger peak as well as the relative differences between this peak and the Cu $2p_{3/2}$ peak provides a reliable method to distinguish between Cu^{1+} and Cu^0.[48,49] This Auger peak is shifted to slightly higher BE, by ~0.4 eV, in LaCuOSe relative to that in Cu metal (Figure A4-3 in Appendix 2), consistent with the assignment of Cu^{1+}.

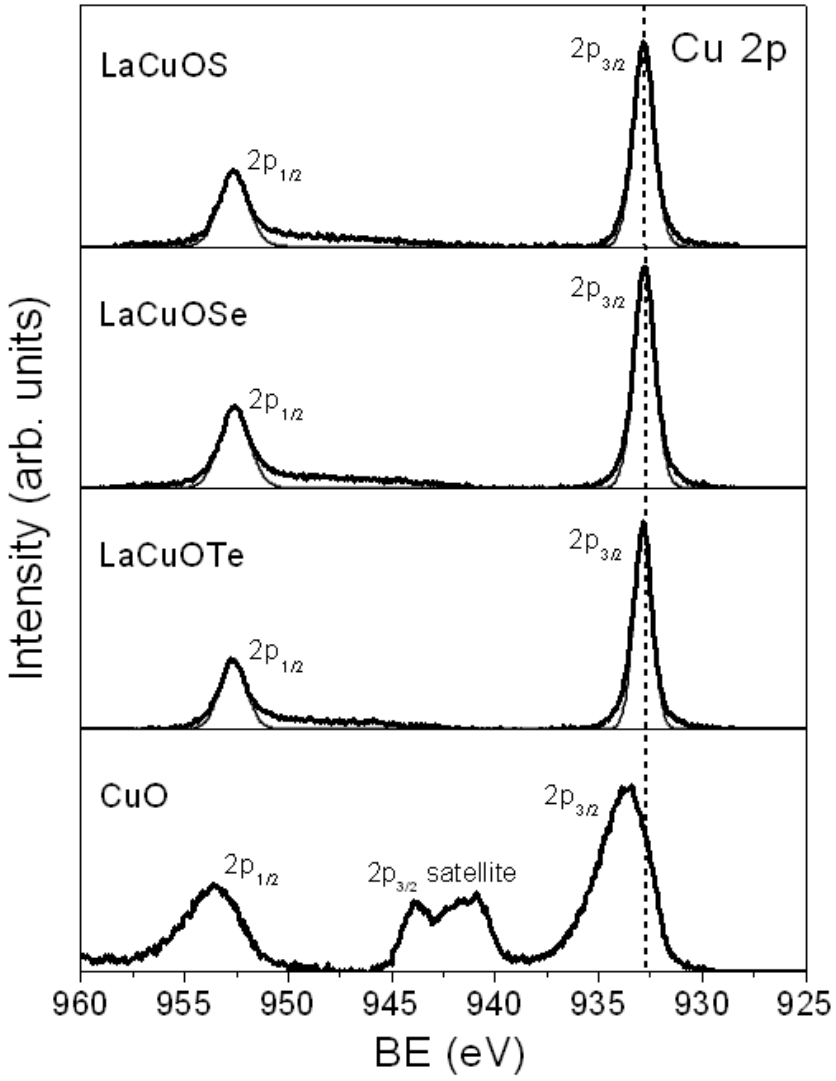

Figure 4-4 Cu 2p XPS spectra for LaCuO*Ch* (*Ch* = S, Se, Te), with the $2p_{3/2}$ BE of 932.7–932.9 eV marked by the dashed vertical line. The spectrum for CuO is included to highlight the satellite peaks that would be characteristic for Cu^{2+} species.

Further support for Cu^{1+} comes from analysis of the Cu XANES spectra (Figure 4-5). In accordance with the selection rule $\Delta l = \pm 1$, the Cu L-edge spectra reveal transitions of electrons from the spin-orbit-split $2p_{3/2}$ (L_3-edge) or $2p_{1/2}$ (L_2-edge) states to available 3d (in the case of Cu^{2+}) or, with lower probability, 4s states (in the case of Cu^{1+} or Cu^0).[50] Consistent with the assignment of Cu^{1+}, the

absorption edges in LaCuO*Ch* show significant fine structure which originates from multiple excitations because the 4s states are hybridized with other states, and the L_3-edge energy (934.7–934.9 eV) is higher than in Cu metal (932.7 eV).[20,50] Similarly, the Cu M-edge spectra reveal transitions from the spin-orbit-split $3p_{3/2}$ (M_3-edge) or $3p_{1/2}$ (M_2-edge) states to 3d or 4s states. These spectra are less intense and show the presence of surface oxides, but it is clear that the absorption edges in LaCuO*Ch* also shift to higher energies, relative to CuO and Cu metal standards.

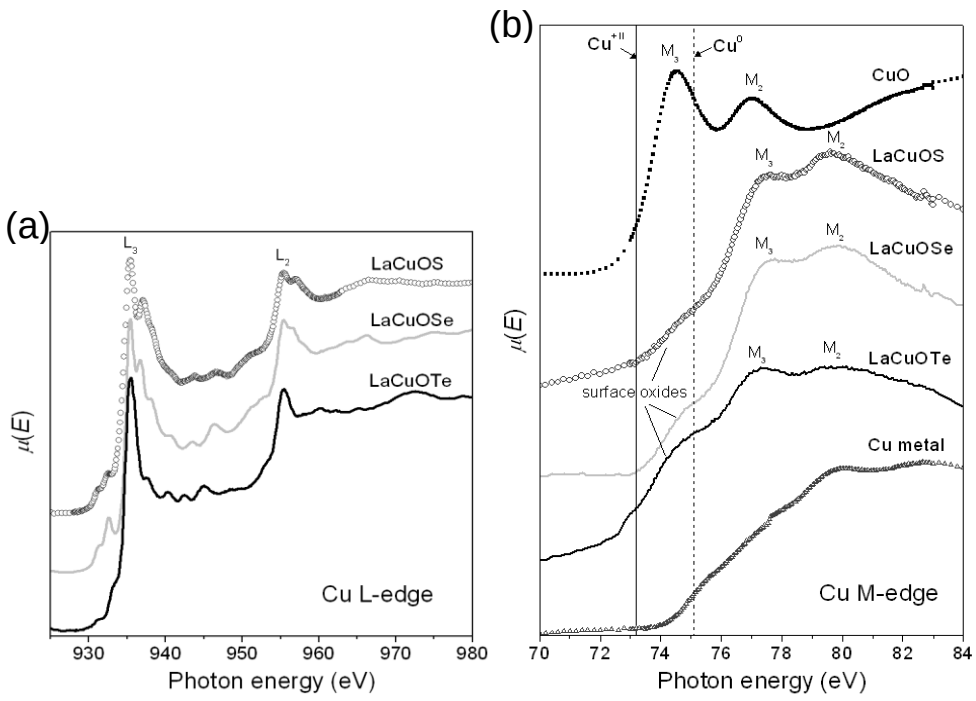

Figure 4-5 (a) Cu L-edge and (b) Cu M-edge XANES spectra for LaCuO*Ch* (*Ch* = S, Se, Te), both measured in transmission mode. The spectra are offset for clarity. In (b), additional Cu M-edge spectra for CuO (with absorption edge at 73.2 eV marked by the solid vertical line) and Cu metal (with absorption edge at 75.1 eV marked by the dashed vertical line) are shown.

The *Ch* XPS spectra reveal shifts to lower BEs for all core-line peaks relative to the element, indicative of anionic species (Figure A4-4 in Appendix 2, with selected spectra in Figure 4-6; BEs for the elements are averaged values taken from the NIST database).[51] The magnitude of these negative BE shifts

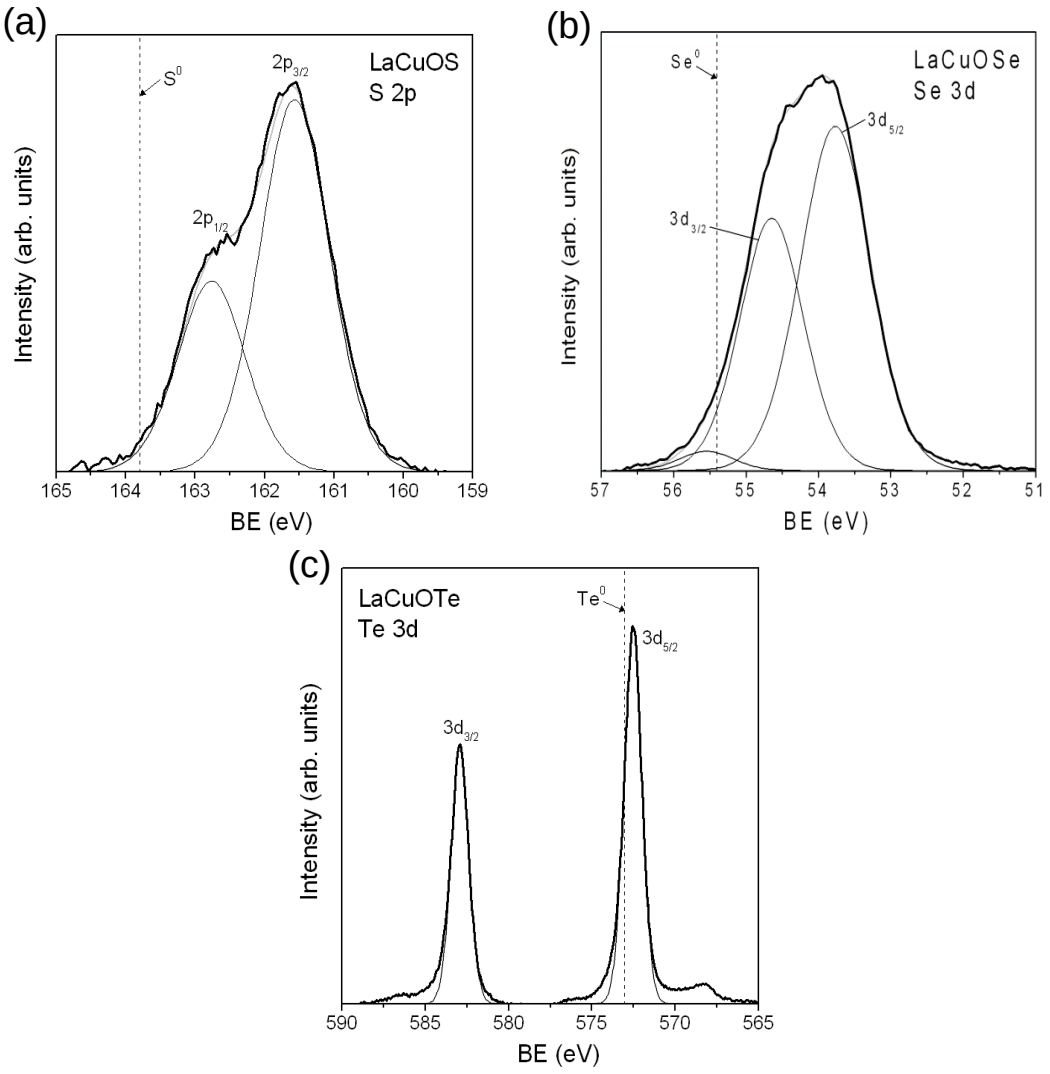

Figure 4-6 Selected *Ch* core-line XPS spectra for LaCuO*Ch* (*Ch* = S, Se, Te). The BEs for the elemental chalcogens (163.8 eV for S $2p_{3/2}$; 55.4 eV for Se $3d_{5/2}$; 573.0 eV for Te $3d_{5/2}$) are marked by dashed vertical lines. (A small Cu LMM Auger peak appears at 567 eV in the spectrum for LaCuOTe.)

follows a clear trend of 0.6–0.8 eV in LaCuOTe, 1.3–1.4 eV in LaCuOSe, and 2.2 eV in LaCuOS. Because the *Ch* atoms are in identical environments in all compounds, the dominant effect must be a ground-state, intraatomic one in which there is an inherent difference in their charge. The BE shifts may be expected to be more pronounced as the electron transfer from Cu to *Ch* atoms (in the Cu–*Ch* bonds) is enhanced with greater electronegativity of the *Ch* atom. However, conventional electronegativity definitions tend to place Se much closer to S than Te, as in the Pauling scale (S, 2.58; Se, 2.55; Te, 2.10),[52,53] or even in a reversed order, as in the Allred-Rochow scale (S, 2.44; Se, 2.48; Te, 2.01).[54] A sensible correlation between the BE shift and the difference in electronegativity ($\Delta\chi = \chi_{Ch} - \chi_{Cu}$) can be achieved only if an intermediate value is chosen for Se. In fact, if a corrected electronegativity for Se is taken simply as the average of that of S and Te in the Allred-Rochow scale, a plot of BE shift vs. $\Delta\chi$ is roughly linear (Figure 4-7). This result lends merit to other scales that place Se at an intermediate value, such as the Allen scale, for which "spectroscopic electronegativities" are defined on the basis of average one-electron energies in a singly-ionized atom.[55] For a given compound LaCuO*Ch*, peaks derived from deeper core levels tend to experience slightly greater BE shifts than those from shallower core levels (cf., 0.80 eV ($3p_{3/2}$), 0.64 eV ($3d_{5/2}$), 0.60 eV ($4d_{5/2}$) for the Te atoms in LaCuOTe).

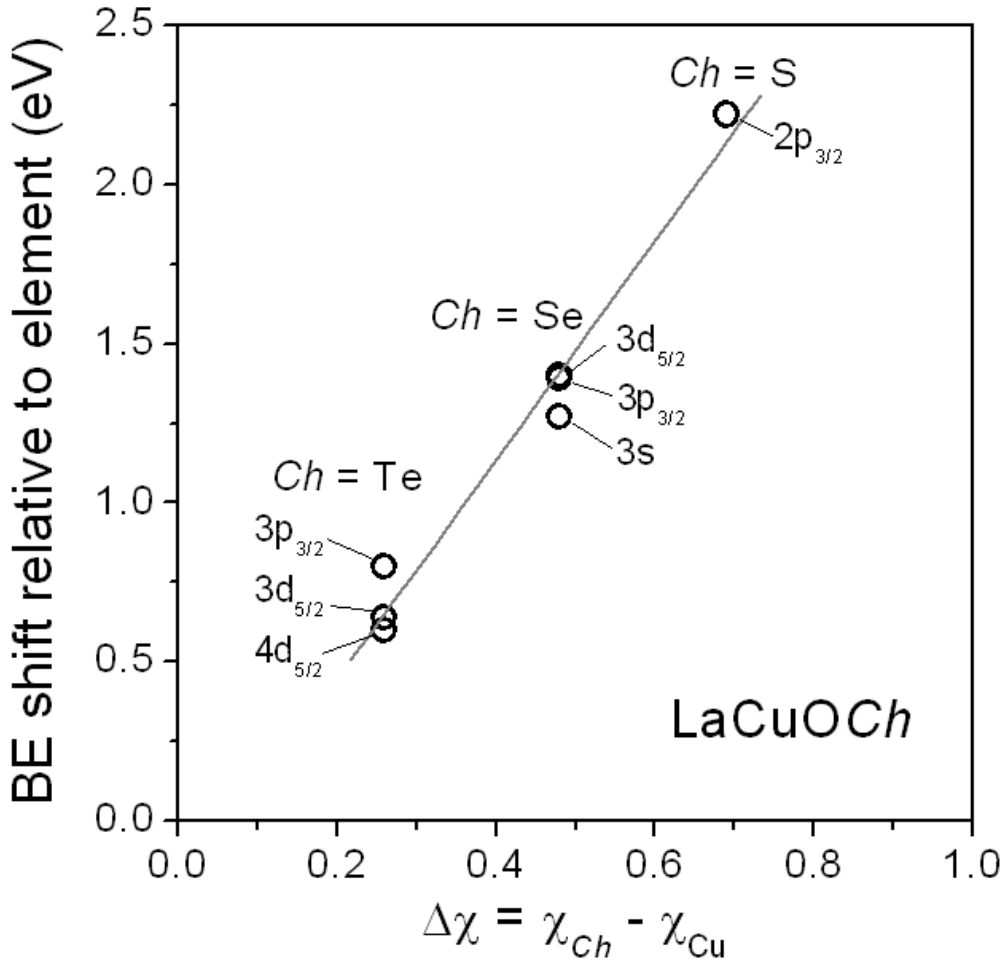

Figure 4-7 Plot of *Ch* BE shifts (negative) for LaCuO*Ch* (*Ch* = S, Se, Te) relative to the elemental chalcogens vs difference in electronegativity between *Ch* and Cu.

4.4 Conclusions

It is instructive to compare the XPS and XANES analyses for LaCuO*Ch* with the isostructural compounds *REM*AsO and ZrCuSi*Pn*.[18–20] The [LaO] layers common to both La*M*AsO and LaCuO*Ch* are essentially identical, as indicated by the similar BE shifts and lineshapes for the La and O core-line peaks. Within the [*M*As] layer of the La*M*AsO series, there are discernable shifts in the As BE,

attributed to ground-state effects, as the *M*-to-As charge transfer is enhanced in the progression of *M* from Ni to Fe. Within the analogous [Cu*Ch*] layer of the LaCuO*Ch* series, it might be anticipated that corresponding shifts in the Cu XPS spectra would reflect the degree of Cu-to-*Ch* charge transfer as *Ch* is changed, but none is observed because of the insensitivity of the Cu $2p_{3/2}$ BE, probably because of final-state effects[56] facilitated, in part, by the presence of weak Cu–Cu bonding (2.8–3.0 Å). However, clear evidence for this charge transfer is provided by the *Ch* core-line peaks, which undergo negative BE shifts (relative to the elemental chalcogen) that become more pronounced with a greater difference in electronegativity ($\chi_{Ch} - \chi_{Cu}$). Both *REM*AsO and LaCuO*Ch* have been typically portrayed as highly two-dimensional structures consisting of independent [*RE*O] layers interleaved with [*M*As] or [Cu*Ch*] layers, respectively. In large measure, this is a reasonably accurate picture: analysis of –ICOHP values obtained from band structure calculations suggests that interlayer bonding accounts for only 4% of the (covalent) bonding energy in LaNiAsO (as evaluated from the La–As interactions of 3.4 Å between the [LaO] and [NiAs] layers) and between 4 to 6% in LaCuO*Ch* (as evaluated from the La–*Ch* interactions of 3.3–3.5 Å between the [LaO] and [Cu*Ch*] layers). Small differences in the satellite intensity of the La 3d XPS spectra in LaCuO*Ch* are suggestive of these weak La–*Ch* interactions. In contrast, ZrCuSi*Pn* exhibits three-dimensional bonding character in ZrCuSi*Pn* (e.g., interlayer Zr–As bonding between the nominal [ZrSi] and [CuAs] layers

accounts for 26% of the covalent bonding energy in ZrCuSiAs), which is manifested by significant shifts in the Zr K-edge absorption energy when *Pn* is changed from As to P.

The XPS analysis of the chalcogen and pnicogen atoms in these compounds deserves further comment. Although they are not yet well-systematized, core-line BE shifts for the anionic species of the heavier p-block elements generally become less pronounced on proceeding from the chalcogens to the pnicogens, in accordance with expectations. These shifts correlate well with differences in electronegativity, provided that they are revised to more intermediate values for the fourth-period elements (Se, 2.22; As, 1.94) if the Allred-Rochow scale is chosen.[57] Thus, for example, the shifts in the Se core-line BEs are much larger in LaCuOSe (1.3–1.4 eV; $\chi_{Se} - \chi_{Cu} = 2.22 - 1.75 = 0.47$) than in the As core-line BEs in LaNiAsO (0.3 eV; $\chi_{As} - \chi_{Ni} = 1.94 - 1.75 = 0.19$) and ZrCuSiAs (0.6 eV; $\chi_{As} - \chi_{Cu} = 1.94 - 1.75 = 0.19$).[18,20] Because LaCuO*Ch* and La*M*AsO are isostructural, it would be interesting to attempt to prepare mixed-anion derivatives such as LaCuO(*Ch*,As), for which the properties could be tuned from a semiconductor to a metal through a change in the electron count. An understanding of these BE shifts will be useful in the eventual analysis of these more complicated systems.

4.5 References

[1] R. Pöttgen, D. Johrendt, Z. Naturforsch. B 63 (2008) 1135–1148.

[2] S.J. Clarke, P. Adamson, S.J.C. Herkelrath, O.J. Rutt, D.R. Parker, M.J. Pitcher, C.F. Smura, Inorg. Chem. 47 (2008) 8473–8486.

[3] B.I. Zimmer, W. Jeitschko, J.H. Albering, R. Glaum, M. Reehuis, J. Alloys Compd. 229 (1995) 238–242.

[4] P. Quebe, L.J. Terbüchte, W. Jeitschko, J. Alloys Compd. 302 (2000) 70–74.

[5] Y. Kamihara, H. Hiramatsu, M. Hirano, R. Kawamura, H. Yanagi, T. Kamiya, H. Hosono, J. Am. Chem. Soc. 128 (2006) 10012–10013.

[6] H. Takahashi, K. Igawa, K. Arii, Y. Kamihara, M. Hirano, H. Hosono, Nature 453 (2008) 376–378.

[7] Y.-W. Ma, Z.-S. Gao, L. Wang. Y.-P. Qi, D.-L. Wang, X.-P. Zhang, Chin. Phys. Lett. 26 (2009) 037401-1–037401-4.

[8] M. Palazzi, C. Carcaly, J. Flahaut, J. Solid State Chem. 35 (1980) 150–155.

[9] S. Inoue, K. Ueda, H. Hosono, N. Hamada, Phys. Rev. B 64 (2001) 245211-1–245211-5.

[10] K. Ueda, K. Takafuji, H. Hiramatsu, H. Ohta, T. Kamiya, M. Hirano, H. Hosono, Chem. Mater. 15 (2003) 3692–3695.

[11] H. Hiramatsu, H. Kamioka, K. Ueda, M. Hirano, H. Hosono, J. Ceram. Soc. Jpn. 113 (2005) 10–16.

[12] H. Hiramatsu, K. Ueda, H. Ohta, T. Kamiya, M. Hirano, H. Hosono, Appl. Phys. Lett. 87 (2005) 211107-1–211107-3.

[13] K. Ueda, H. Hiramatsu, M. Hirano, T. Kamiya, H. Hosono, Thin Solid Films 496 (2006) 8–15.

[14] H. Hiramatsu, H. Kamioka, K. Ueda, H. Ohta, T. Kamiya, M. Hirano, H. Hosono, Phys. Status Solidi A 203 (2006) 2800–2811.

[15] H. Hiramatsu, H. Yanagi, T. Kamiya, K. Ueda, M. Hirano, H. Hosono, Chem. Mater. 20 (2008) 326–334.

[16] V. Johnson, W. Jeitschko, J. Solid State Chem. 11 (1974) 161–166.

[17] H. Abe, K. Yoshii, J. Solid State Chem. 165 (2002) 372–374.

[18] P.E.R. Blanchard, B.R. Slater, R.G. Cavell, A. Mar, A.P. Grosvenor, Solid State Sci. 12 (2010) 50–58.

[19] P.E.R. Blanchard, R.G. Cavell, A. Mar, J. Solid State Chem. 183 (2010) 1477–1483.

[20] P.E.R. Blanchard, R.G. Cavell, A. Mar, J. Solid State Chem. 183 (2010) 1536–1544.

[21] K. Ueda, H. Hosono, N. Hamada, J. Appl. Phys. 98 (2005) 043506-1–043506-7.

[22] H. Sato, S. Nishimoto, K. Tsuji, K. Takase, H. Nakao, Y. Takahashi, T. Takano, K. Sekizawa, H. Negishi, S. Negishi, M. Nakatake, H. Namatame, M. Taniguchi, J. Alloys Compd. 408–412 (2006) 746–749.

[23] N. Fairley, CasaXPS, version 2.3.9, Casa Software Ltd., Teighnmouth, Devon, UK, 2003, <www.casaxps.com>.

[24] B. Ravel, M. Newville, J. Synchrotron Radiat. 12 (2005) 537–541.

[25] M.L. Liu, L.B. Wu, F.Q. Huang, L.D. Chen, J.A. Ibers, J. Solid State Chem. 180 (2007) 62–69.

[26] R. Tank, O. Jepsen, A. Burkhardt, O.K. Andersen, TB-LMTO-ASA Program, Version 4.7, Max Planck Institut für Festkörperforschung, Stuttgart, Germany, 1998.

[27] W. Grünert, U. Sauerlandt, R. Schlögl, H.G. Karge, J. Phys. Chem. 97 (1993) 1413–1419.

[28] E. Talik, A. Novosselov, M. Kulpa, A. Pajaczkowska, J. Alloys Compd. 321 (2001) 24–26.

[29] A. Novosselov, E. Talik, A. Pajaczkowska, J. Alloys Compd. 351 (2003) 50–53.

[30] A.J. Signorelli, R.G. Hayes, Phys. Rev. B 8 (1973) 81–86.

[31] G. Crecelius, G.K. Wertheim, D.N.E. Buchanan, Phys. Rev. B 18 (1978) 6519–6524.

[32] S.-J. Oh, G.-H. Kim, G.A. Sawatzky, H.T. Jonkman, Phys. Rev. B 37 (1988) 6145–6152.

[33] J.H. Scofield, J. Electron Spectrosc. Relat. Phenom. 8 (1976) 129–137.

[34] J.J. Yeh, I. Lindau, At. Data Nucl. Data Tables 32 (1985) 1–155.

[35] T.L. Barr, Modern ESCA: The Principles and Practice of X-Ray Photoelectron Spectroscopy, CRC Press, Boca Raton, FL, 1994.

[36] V. Dimitrov, T. Komatsu, J. Solid State Chem. 163 (2002) 100–112.

[37] D.C. Frost, A. Ishitani, C.A. McDowell, Mol. Phys. 24 (1972) 861–877.

[38] R.P. Vasquez, Surf. Sci. Spectra 5 (1998) 257–261.

[39] R.P. Vasquez, Surf. Sci. Spectra 5 (1998) 262–266.

[40] S.K. Chawla, N. Sankarraman, J.H. Payer, J. Electron Spectrosc. Relat. Phenom. 61 (1992) 1–18.

[41] A.C. Miller, G.W. Simmons, Surf. Sci. Spectra 2 (1993) 55–60.

[42] R.P. Vasquez, Surf. Sci. Spectra 2 (1993) 144–148.

[43] R.P. Vasquez, Surf. Sci. Spectra 2 (1993) 149–154.

[44] A. Rosencwaig, G.K. Wertheim, J. Electron Spectrosc. Relat. Phenom. 1 (1972/73) 493–496.

[45] F. Werfel, M. Heinonen, E. Suoninen, Z. Phys. B: Condens. Matter 70 (1988) 317–322.

[46] A. Roberts, D. Engelberg, Y. Liu, G.E. Thompson, M.R. Alexander, Surf. Interface Anal. 33 (2002) 697–703.

[47] T. Ghodselahi, M.A. Vesaghi, A. Shafiekhani, A. Baghizadeh, M. Lameii, Appl. Surf. Sci. 255 (2008) 2730–2734.

[48] T.H. Fleisch, G.J. Mains, Appl. Surf. Sci. 10 (1992) 51–62.

[49] J.P. Espinós, J. Morales, A. Barranco, A. Caballero, J.P. Holgado, A.R. González-Elipe, J. Phys. Chem. B 106 (2002) 6921–6929.

[50] R.A.D. Pattrick, G. van der Laan, J.M. Charnock, B.A. Grguric, Am. Mineral. 89 (2004) 541–546.

[51] C.D Wagner, A. V. Naumkin, A. Kraut-Vass, J.W. Allison, C.J. Powell, J. R. Rumble Jr., NIST X-ray Photoelectron Spectroscopy Database, version 3.5 (web version), National Institute of Standards and Technology, Gaithersburg, MD 2003, <srdata.nist.gov/xps>.

[52] A.L. Allred, J. Inorg. Nucl. Chem. 17 (1961) 215–221.

[53] L.R. Murphy, T.L. Meek, A.L. Allred, L.C. Allen, J. Phys. Chem. A 104 (2000) 5867–5871.

[54] A.L. Allred, E.G. Rochow, J. Inorg. Nucl. Chem. 5 (1958) 264–268.

[55] L.C. Allen, J. Am. Chem. Soc. 111 (1989) 9003–9014.

[56] P.A.W. van der Heide, J. Electron Spectrosc. Relat. Phenom. 151 (2006) 79–91.

[57] A.P. Grosvenor, R.G. Cavell, A. Mar, J. Solid State Chem. 181 (2008) 2549–2558.

Chapter 5

X-ray photoelectron and absorption spectroscopy of mixed lanthanum copper oxychalcogenides $LaCuOSe_{1-x}Te_x$ $(0 \leq x \leq 1)$[1]

5.1 Introduction

The quaternary rare-earth copper oxychalcogenides *RE*CuO*Ch* (*Ch* = S, Se, Te) have been explored for potential applications in optoelectronic devices as transparent p-type semiconductors,[1–7] and the properties are thought to depend on the complex interplay of electronic interactions between the covalent, conducting [Cu*Ch*] or [*MPn*] layers and the ionic, insulating [*RE*O] layers which are alternately stacked along the c-direction in their tetragonal structures (inset of Figure 5-1),[8,9] thus further exploration into the strength and tunability of inter- and intralayer interactions is important. They belong to the large family of tetragonal ZrCuSiAs-type materials, which include the rare-earth transition-metal oxypnictides *REMPn*O (*P* = P, As), now in vogue owing to their high-temperature superconducting behaviour.[10–14] Evaluating the degree of charge transfer within and between these layers is important for understanding how these properties can be modified. Previous analyses of X-ray photoelectron (XPS) and X-ray absorption near-edge spectra (XANES) support the picture of a highly two-dimensional layered structure for *RE*CuO*Ch* and *REMPn*O,[15–17] in contrast to

[1] *A version of this chapter has been published. B.W Rudyk, P.E.R. Blanchard, R.G. Cavell, A. Mar, J. Alloys Compd. 514 (2012) 199–204. Copyright (2012) by Elsevier.*

tetrelide pnictides like ZrCuSiAs itself, which shows three-dimensional bonding character.[18,19] However, in the LaCuO*Ch* (*Ch* = S, Se, Te) series discussed in Chapter 4, there is evidence for the occurrence of weak interlayer La–*Ch* interactions between the [LaO] and [Cu*Ch*] layers that become enhanced with larger *Ch* atoms, through the observation of changes in the intensity of a satellite feature in the La 3d XPS spectra.[17] Intralayer Cu–*Ch* interactions would also be expected within the [Cu*Ch*] layers, but these were more problematic to detect because of final-state effects in the Cu 2p XPS spectra.

The mixed-chalcogenide solid solution $LaCuOSe_{1-x}Te_x$ ($0 \leq x \leq 1$) presents an attractive opportunity to analyze these electronic interactions in more detail. Herein, firmer evidence for interlayer interactions between the [LaO] and [Cu*Ch*] layers, as manifested by shifts in binding energies (BEs) in the O and *Ch* XPS spectra that are influenced by the chemical environment is presented. The nature of the intralayer Cu–*Ch* interactions within the [Cu*Ch*] layers by examining changes in the Cu K-edge and Se K-edge XANES spectra, which are less sensitive to final-state effects, is also probed.

5.2 Experimental

5.2.1 Synthesis

Reagents in the form of pieces (La) or powders (La_2O_3, Cu, Se, and Te) with purities of 99.5% or better were obtained from Cerac, Aldrich, or Alfa-Aesar. La_2Se_3 was obtained by stoichiometric reaction of La and Se at 900 °C for 1 week.

LaCuOSe was prepared by heating a mixture of La_2O_3, La_2Se_3, Cu, and Se in a 2:1:6:3 ratio in an evacuated and sealed fused-silica tube at 1050 °C for 10 days. LaCuOTe was prepared by heating a mixture of La, La_2O_3, Cu, and Te in a 1:1:3:3 ratio in an evacuated and sealed fused-silica tube at 1050 °C for 1–2 weeks; regrinding the quenched product and reheating for an additional week was required for complete reaction. Members of the solid solution $LaCuOSe_{1-x}Te_x$ (x = 0.2, 0.3, 0.4, 0.6, 0.8) were prepared by heating mixtures of the end-members LaCuOSe and LaCuOTe in appropriate ratios at 1050 °C in three cycles of 4 days each, with intermediate grindings. All compounds were found to be >98% pure, as determined by comparing the intensities of the strongest peaks relative to those for impurity phases in their powder X-ray diffraction (XRD) patterns (Figure A3-1 in Appendix 3) collected on an Inel diffractometer equipped with a CPS 120 detector. The cell parameters (Table 5-1) for this complete solid solution increase regularly as x increases in $LaCuOSe_{1-x}Te_x$, consistent with the substitution of larger Te for Se atoms (Figure 5-1). The cell volume exhibits a small negative deviation from a strictly linear Vegard's law dependence, suggesting that there may be slight local ordering of the chalcogen atoms when the concentrations of Se and Te are similar. A similar behaviour was previously observed for the $LaCuOS_{1-x}Se_x$ solid solution.[20]

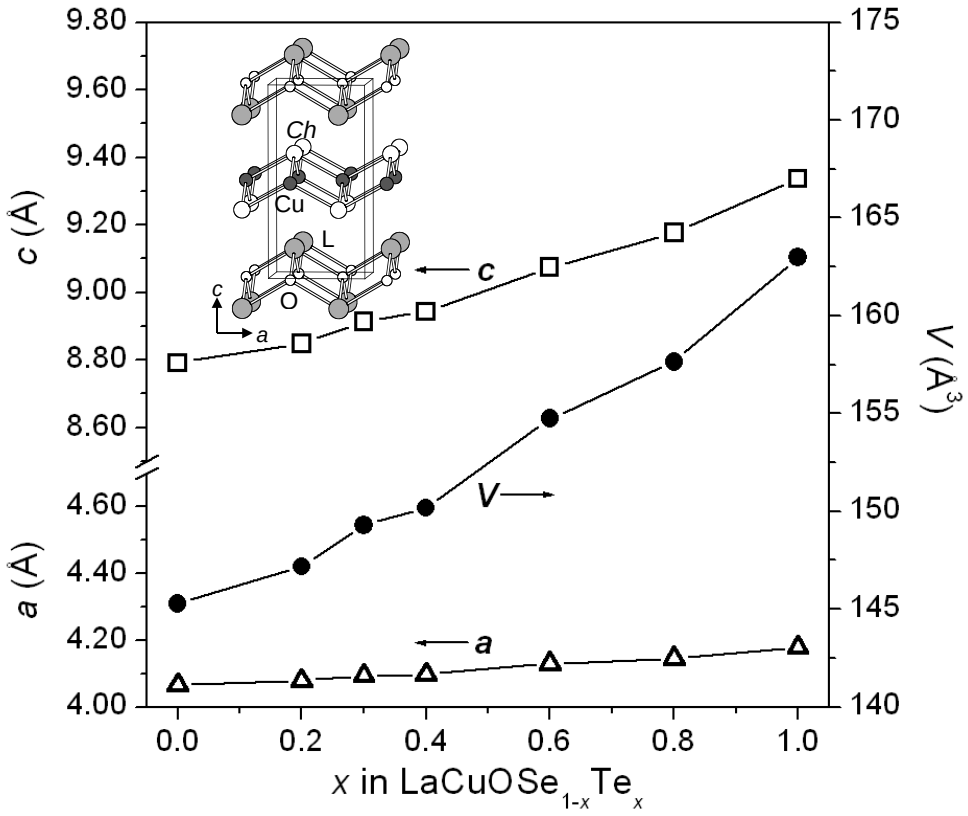

Figure 5-1 Plot of cell parameters vs *x* for $LaCuOSe_{1-x}Te_x$ forming the tetragonal ZrCuSiAs-type structure (inset). The lines are shown only to guide the eye.

Table 5-1 Cell parameters for $LaCuOSe_{1-x}Te_x$.

Compound	*a* (Å)	*c* (Å)	*V* (Å^3)
LaCuOSe	4.0651(1)	8.7914(2)	145.28(1)
$LaCuOSe_{0.8}Te_{0.2}$	4.0784(1)	8.8485(3)	147.18(1)
$LaCuOSe_{0.7}Te_{0.3}$	4.0927(1)	8.9128(2)	149.29(1)
$LaCuOSe_{0.6}Te_{0.4}$	4.0976(1)	8.9434(3)	150.16(1)
$LaCuOSe_{0.4}Te_{0.6}$	4.1294(1)	9.0748(2)	154.74(1)
$LaCuOSe_{0.2}Te_{0.8}$	4.1447(1)	9.1768(2)	157.64(1)
LaCuOTe	4.1783(1)	9.3363(3)	163.00(1)

5.2.2 XPS analysis

XPS spectra were measured on a Kratos AXIS 165 spectrometer equipped with a monochromatic Al Kα X-ray source (15 kV, 14 mA) and a hybrid lens with a spot size of 700 μm × 400 μm. The air-stable samples were finely ground, pressed onto In foil, mounted on a Cu sample stage with carbon tape, and transferred to the spectrometer chamber in which the pressure was maintained between 10^{-7} and 10^{-9} Pa. The samples were sputter-cleaned with an Ar^+ beam (4 kV, 10 mA) to remove surface oxides as much as possible until no further changes were observed in the survey spectra. No visible chemical reduction occurred as a result of this sputtering procedure. Charge neutralization was attempted but was concluded to be unnecessary.

Survey spectra (collected with a BE range of 0–1100 eV, a pass energy of 160 eV, a step size of 0.7 eV, and a sweep time of 180 s) confirmed the presence of all elements in the expected compositions. High-resolution La 3d, Cu 2p, O 1s, Se 3p, Se 3d, Te 3d, and Te 4d core-line spectra (collected with a BE range appropriate for each element as determined from the survey spectra, a pass energy of 20 eV, a step size of 0.05 eV, and a sweep time of 180 s) were calibrated to the C 1s line at 284.8 eV arising from adventitious carbon. These spectra were analyzed with use of the CasaXPS software package.[21] The background arising from energy loss was removed by applying a Shirley-type function and the peaks were fitted to pseudo-Voigt (70% Gaussian and 30% Lorentzian) line profiles to take into account spectrometer and lifetime broadening effects. Table 5-2 lists the observed BE values, with uncertainties estimated to be better than ±0.1 eV

obtained from singly measured spectra, on the basis of previous measurements on this instrument. Because small shifts in the O 1s and Se 3d BEs were noted, these spectra were re-collected for all members of the solid solution (including the previously measured end-members LaCuOSe and LaCuOTe)[17] to obtain more precise values. For each member, two or three samples from the same synthesis batch were separately ground, sputter-cleaned, and examined individually (Table A3-1 in Appendix 3). On the basis of these multiply measured spectra, the O 1s and Se 3d BEs were averaged and expressed to two decimal places in Table 5-2. Their uncertainties evaluated from $(ts)/\sqrt{n}$, where *t* values were taken at a 95% confidence interval, *s* is the standard deviation, and *n* is the number of measurements, were generally better than ±0.05 eV.

Table 5-2 XPS binding energies (eV) and XANES absorption edge energies (eV) for members of the solid solution $LaCuOSe_{1-x}Te_x$.

Compound	LaCuOSe	$LaCuOSe_{0.8}Te_{0.2}$	$LaCuOSe_{0.7}Te_{0.3}$	$LaCuOSe_{0.6}Te_{0.4}$	$LaCuOSe_{0.4}Te_{0.6}$	$LaCuOSe_{0.2}Te_{0.8}$	LaCuOTe [a]
La $3d_{5/2}$	834.3(1) [a]	834.4(1)	834.4(1)	834.5(1)	834.4(1)	834.4(1)	834.5(1) [a]
La $3d_{3/2}$	851.1(1) [a]	851.2(1)	851.2(1)	851.4(1)	851.3(1)	851.2(1)	851.2(1) [a]
Cu $2p_{3/2}$	932.8(1) [a]	932.8(1)	932.9(1)	932.9(1)	932.8(1)	932.9(1)	932.9(1) [a]
Cu $2p_{1/2}$	952.6(1) [a]	952.6(1)	952.7(1)	952.8(1)	952.6(1)	952.7(1)	952.7(1) [a]
Cu K-edge [b]	8986.1(1)	8986.0(1)	8985.8(1)	8985.8(1)	8985.7(1)	8985.6(1)	8985.3(1)
O 1s [c]	529.77(5)	529.63(5)	529.61(10)	529.58(2)	529.51(5)	529.42(5)	529.74(3)
Se $3d_{5/2}$ [c]	53.93(3)	53.86(3)	53.85(3)	53.85(3)	53.83(3)	53.78(3)	
Se $3d_{3/2}$ [c]	53.78(3)	54.71(3)	54.70(3)	54.70(3)	54.68(3)	54.63(3)	
Se $3p_{3/2}$	160.1(1) [a]	160.2(1)	160.2(1)	160.2(1)	160.1(1)	160.3(1)	
Se $3p_{1/2}$	165.9(1) [a]	166.0(1)	166.0(1)	166.0(1)	165.8(1)	165.9(1)	
Se L-edge	1429.6(1)	1429.4(1)	1429.4(1)	1429.5(1)	1429.5(1)	1429.4(1)	
Se K-edge	12658.2(1)	12658.3(1)	12658.3(1)	12658.3(1)	12658.3(1)	12658.4(1)	
Te $4d_{5/2}$		40.2(1)	40.3(1)	40.3(1)	40.2(1)	40.2(1)	40.2(1) [a]
Te $4d_{3/2}$		41.7(1)	41.7(1)	41.7(1)	41.6(1)	41.6(1)	41.7(1) [a]
Te $3d_{5/2}$		572.7(1)	572.7(1)	572.7(1)	572.6(1)	572.6(1)	572.6(1) [a]
Te $3d_{3/2}$		583.1(1)	583.1(1)	583.1(1)	583.0(1)	583.0(1)	582.9(1) [a]

[a] Taken from Ref. 17. [b] Cu K-pre-edge located at 8980.6(1) eV for all samples. [c] O 1s and Se 3d BEs were averaged from multiply measured spectra, with uncertainties quoted at a 95% confidence interval

5.2.3 Cu K- and Se K-edge XANES analyses

Cu K- and Se K-edge XANES spectra were measured on the bending magnet beamline (20BM) at the Advanced Photon Source (APS) accessed through the Pacific Northwest Consortium / X-ray Operations and Research Collaborative Access Team (PNC/XOR-CAT), Sector 20, at Argonne National Laboratory. Finely ground samples were sandwiched between Kapton tape and positioned at 45° to the X-ray beam, which has a resolution of 1.4 eV at 10 keV, a spot size of 1 mm × 4.5 mm, and a photon flux of ~10^{11} photons/s provided by a silicon (111) double crystal monochromator. Spectra were collected in both transmission mode (through an ionization detector filled with a 60:40 mixture of He and N_2) and fluorescence mode (through a 4-element Vortex detector for the Cu K-edge and a 13-element Canberra detector for the Se K-edge). The step size through the absorption edge was 0.25 eV. Standards of elemental Cu and Se were placed behind the sample and measured simultaneously, with the maxima in the first derivatives set to 8979 eV for the Cu K-edge and 12658 eV for the Se K-edge. Calibration values were obtained from the program Hephaestus and the spectra were analyzed with the program Athena, both in the Ifeffit software package.[22] Uncertainties in the absorption energies are estimated to be better than ±0.1 eV on the basis of multiple scans. All observed absorption edge energies are listed in Table 5-2.

5.2.4 Band structure calculations

The interpretation of XANES spectra was facilitated by evaluating the character of empty conduction states in LaCuOSe and LaCuOTe determined by tight-binding linear muffin tin orbital (TB-LMTO) band structure calculations performed within the local density and atomic spheres approximation with use of the Stuttgart TB-LMTO-ASA program (version 4.7).[23] Integrations were carried out over 84 independent *k* points within the first Brillouin zone.

5.3 Results and discussion

5.3.1 XPS spectra

An initial examination of the core-line XPS spectra for the solid solution $LaCuOSe_{1-x}Te_x$ ($0 \leq x \leq 1$) revealed no prominent differences. Although the *Ch* atoms are closest to the La and Cu atoms, the gradual substitution of Se with Te is not reflected in any detectable changes in the La 3d and Cu 2p spectra, which are strongly influenced by final state effects (Figure A3-2 in Appendix 3).[24–29] The La 3d spectra contain a satellite peak which was previously attributed to a ligand-to-metal shake-up process and which serves to measure the degree of orbital overlap between La and *Ch* atoms,[17, 27–29] but the differences are too small between the end-members LaCuOSe and LaCuOTe for this feature to be helpful to monitor. Similarly, the Cu 2p spectra are invariant, and in any case, the Cu $2p_{3/2}$ BE cannot be probed reliably to obtain information about oxidation state.[30,31] Final state effects are quite prominent in Cu XPS spectra, as have been noted previously.[32] When a core-hole is generated upon photoionization, interatomic

relaxation can take place whereby electron density from surrounding atoms flows towards it, enhancing the screening so that the final state energy is decreased and the BE is apparently lowered. This relaxation becomes more pronounced with higher oxidation state of the Cu atom, and it becomes difficult to separate ground-state from final-state effects in Cu XPS spectra.[32]

Each of the O 1s XPS spectra reveals a main core-line peak inherent to the oxychalcogenide at lower BE and a second peak attributed to surface oxides that is typically found at higher BE (Figure 5-2a).[15,16] Although surface oxides are normally difficult to eliminate entirely, they were minimized through sputter-cleaning for a duration that does not risk damaging the sample. In the course of this sputtering procedure, the intensity of the peak arising from surface oxides diminished while the position of the main core-line peak for the oxychalcogenide remained invariant. Surprisingly, we noted subtle changes in the O 1s XPS

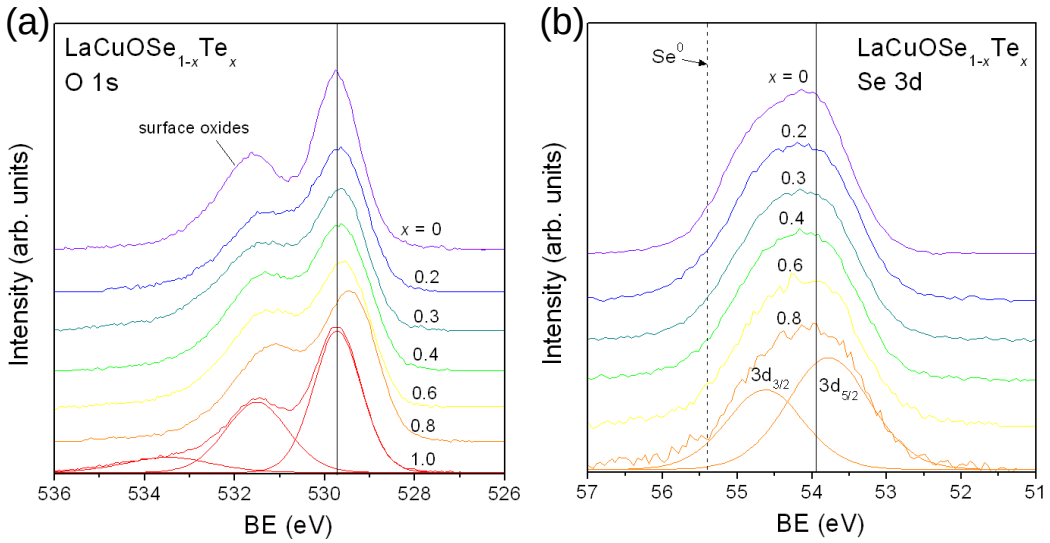

Figure 5-2 (a) O 1s and (b) Se 3d XPS spectra for $LaCuOSe_{1-x}Te_x$. The solid vertical lines locate the O 1s and Se $3d_{5/2}$ peaks in LaCuOSe. For reference, the dashed vertical line in (b) marks the Se $3d_{5/2}$ BE in elemental Se.

spectra in which there were small BE shifts of up to ~0.2 eV, just above the limits of uncertainty (±0.1 eV). These spectra were recollected multiple times to improve statistics, confirming a real trend in the O 1s BEs (Table 5-2 and Figure 5-2a). As Se is substituted with Te, the O 1s BE gradually decreases from 529.77(2) eV in LaCuOSe to 529.42(2) eV in $LaCuOSe_{0.2}Te_{0.8}$, but then it abruptly returns to 529.74(1) eV in LaCuOTe. Differences in the *Ch* XPS spectra were more difficult to detect. Multiply measured Se 3d spectra suggest a gradual decrease in the Se $3d_{5/2}$ BE from 53.93(1) eV in LaCuOSe to 53.78(1) eV in $LaCuOSe_{0.2}Te_{0.8}$, with the spectra of the Se-poorer samples suffering from greater background noise because of the lower Se concentration (Figure 5-2b). The remaining *Ch* XPS spectra (Se 3p, Te 4d, Te 3d) are nearly indistinguishable (Figure A3-2 in Appendix 3).

Although BE shifts in the La 3d and Cu 2p spectra cannot be used to extract information about charges, we make the assumption that these atoms are positively charged, with formal oxidation states of La^{3+} and Cu^{+}. The BEs in the O 1s and *Ch* (Se 3d, 3p; Te 4d, 3d) spectra are lower relative to the elements (dashed vertical lines in the spectra),[33] indicating that these atoms are negatively charged. However, the trends in the O 1s and Se 3d BEs with greater substitution *x* in the solid solution $LaCuOSe_{1-x}Te_x$ (Figure 5-3a) require different explanations. The decrease in Se 3d BE suggests that the Se atoms, which are more electronegative than Te atoms, must accept a greater burden of the charge transferred in the Cu–*Ch* bonds; each of the diminishing number of Se atoms carries a more negative charge. The occurrence of BE shifts, albeit small, in the

O 1s peak is puzzling because the O atoms are not directly bonded to the *Ch* atoms. However, weak La–*Ch* interactions between the ostensibly independent [LaO] and [Cu*Ch*] layers have been implicated previously.[17] We propose that the O 1s BE shifts are not caused by changes in the charge of the O atoms (an intraatomic effect), but rather by changes in their coordination environment, which modifies the Madelung potential (an interatomic effect). When the charge potential model is applied,[34–37] the O 1s BE shifts can be described as:

$$\Delta E_{\mathrm{O1s}} = k\Delta q_{\mathrm{O}} + 4\Delta\left(q_{\mathrm{La}}/d_{\mathrm{O-La}}\right) + 4\Delta\left(q_{\mathrm{O}}/d_{\mathrm{O-O}}\right) + 4\Delta\left(q_{Ch}/d_{\mathrm{O-}Ch}\right) + \ldots \quad \text{(Equation 5-1)}$$

in which the first term represents any inherent changes in the O charge and the subsequent terms represent the contributions of the first, second, and third coordination spheres (CS) around the O atom to the Madelung potential. As more Se is substituted by Te atoms (increasing x in $LaCuOSe_{1-x}Te_x$), the La atoms become less positively charged (if the occurrence of La–*Ch* interactions is

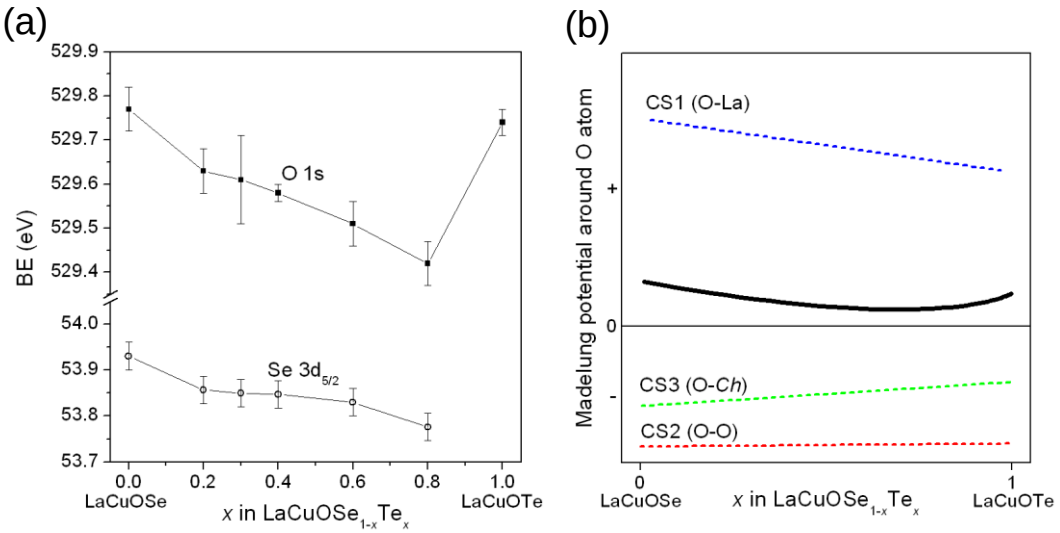

Figure 5-3 (a) Plot of O 1s and Se $3d_{5/2}$ BEs vs. x in $LaCuOSe_{1-x}Te_x$. (b) Schematic representation of the contributions (dashed lines) of the first, second, and third coordination spheres (CS) to the Madelung potential (solid line) experienced by the O atom in $LaCuOSe_{1-x}Te_x$.

accepted); that is, the $\Delta(q_{La}/d_{O–La})$ term becomes less positive. Meanwhile, the *Ch* atoms become less negatively charged and more distant (from 3.5 to at 3.7 Å), on average; that is, the $\Delta(q_{Ch}/d_{O–Ch})$ term becomes less negative. Thus, the evolution of these contributions to the Madelung potential from the first and third CS, respectively, follows opposing trends, as qualitatively shown in Figure 5-3b. The summation of these two oppositely sloped lines leads to a minimum in the Madelung potential at some intermediate value of *x*, as shown by the solid black line in the figure. Because the neighbouring La atoms in the first CS dominate the Madelung potential, the O 1s BE tends to decrease gradually with increasing *x*. However, at sufficiently high substitution levels, the contribution from the third CS eventually reverses the trend, such that in the end-member LaCuOTe ($x = 1$), the O 1s BE is essentially the same as in LaCuOSe ($x = 0$).

The analysis of the O 1s BE shifts above rests on the assumption that they depend mainly on ground-state effects, but it is worthwhile considering if final-state effects could also account for the observed trends in which the BE is apparently lowered because of interatomic relaxation, as described earlier.[32] Because the immediate environment around each O atom is a tetrahedron of four La atoms, the highly ionic nature of the La–O interactions implies that such relaxation processes are unlikely. However, it is conceivable that as the more distant *Ch* atoms in the third CS become increasingly substituted with less electronegative Te atoms, the La atoms gain more electron density so that this relaxation becomes enhanced. If so, the O 1s BE would decrease monotonically and reach its lowest value at LaCuOTe. As discussed above, the reversal of the

trend actually seen at LaCuOTe can be traced to a ground-state effect involving the Madelung potential, implying these final-state effects are less important.

5.3.2 XANES spectra

Information about the Cu atoms is best extracted through analysis of the Cu K-edge absorption spectra. These spectra are much less influenced by final state effects than the Cu 2p XPS spectra because electrons are excited into bound (or continuum) states, providing partial screening which in turn minimizes relaxation processes. In accordance with the selection rule $\Delta l = \pm 1$, the most prominent feature in the Cu K-edge spectra of $LaCuOSe_{1-x}Te_x$ is assigned to the excitation of Cu 1s electrons to unoccupied 4p states, marked as A in Figure 5-4a. This main edge-feature is prominent in other compounds containing tetrahedrally coordinated Cu^{1+} species, such as Cu(I) halides, and is unaffected by multiscattering resonance within the EXAFS region.[38] The absorption-edge

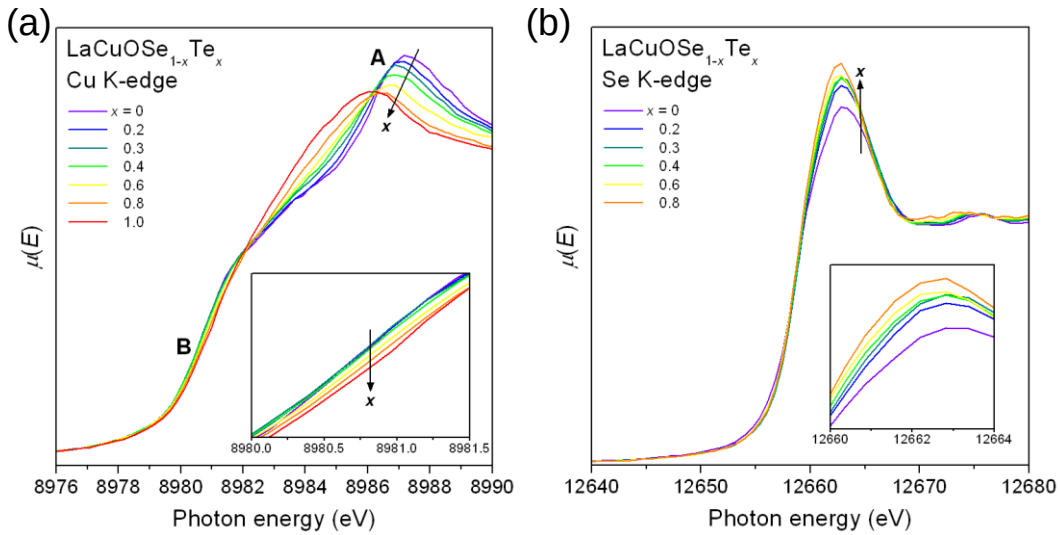

Figure 5-4 (a) Cu K-edge and (b) Se K-edge XANES spectra for $LaCuOSe_{1-x}Te_x$.

energy gradually decreases from 8986.1(1) eV in LaCuOSe to 8985.3(1) eV in LaCuOTe, indicating that the Cu atoms become less positively charged and consistent with diminished Cu-to-*Ch* electron transfer when Se atoms are successively substituted by less electronegative Te atoms. The shift in the absorption edge to lower energy also agrees with the location of empty Cu-4p-based conduction levels in the density of states for LaCuOSe vs. LaCuOTe (Figure A3-3 in Appendix 3). There is a second, weaker pre-edge feature, marked as B in the spectra, that appears to be fixed in energy (as confirmed by noting the invariance in the maximum of the first derivative in the spectra) but instead becomes slightly less intense on proceeding from LaCuOSe to LaCuOTe. Such a feature is normally assigned as a dipole-forbidden 1s-to-3d transition in Cu^{2+}-containing compounds.[39] Although XPS and Auger spectroscopy indicate that the present compounds contain Cu^{1+} species,[17] which have no available empty 3d states, we propose that the transition becomes allowed through mixing of 3d and empty 4p states in the tetrahedrally coordinated Cu atoms (which lack an inversion centre).[16,38] Cu(I) halides exhibit similar 1s-to-3d/4p pre-edge features, with significant intensity because of the mixing with empty 4p states[38] The diminished Cu-to-*Ch* charge transfer leads to fewer available empty hybridized 3d/4p-based Cu states to which electrons can be excited and thus lower probability for the absorption process to take place. For comparison at the other extreme, the pre-edge is most intense in LaCuOS (Figure A3-4 in Appendix 3).

The Se K-edge spectra probes transitions from filled Se 1s to empty Se 4p states, as manifested by an absorption edge energy of 12658.2(1)–12658.4(1) eV

that is nearly constant, within error, for all members of $LaCuOSe_{1-x}Te_x$ (Figure 5-4b). (These spectra are shown in fluoresence mode, providing a smoother background than in the more usually preferred transmission mode, which gave poorer signal-to-noise ratios, especially for samples with low Se concentrations.) Interestingly, the absorption edge signal strengthens in intensity on proceeding from LaCuOSe to $LaCuOSe_{0.2}Te_{0.8}$. This trend runs counter to expectations based on decreasing Se concentration, as has been seen, for instance, in Se K-edge spectra for $FeSe_{1-x}Te_x$, where strong chalcogen-chalcogen bonds (~2.7 Å) are present.[40–42] Although absorption spectra measured in fluorescence mode commonly suffer from self-absorption effects, we consider such effects to be unlikely here because the X-ray energy is quite high (12 keV), which reduces photoionization cross-sections,[43] the samples analyzed are thin,[44–46] and the Se concentrations are low. Instead, we propose that the La–*Ch* interactions described earlier between the [LaO] and [Cu*Ch*] layers provide a mechanism for hybridization of La- and *Ch*-based conduction states, as confirmed by inspection of the DOS curves in the calculated band structures (Figure A3-3 in Appendix 3). The energy dispersion of these conduction states widens by 0.5 eV on proceeding from LaCuOSe to LaCuOTe, leading to greater probability for absorption from the Se 1s states and thus a more intense absorption edge signal.

5.4 Conclusions

Further evidence for the occurrence of weak La–*Ch* interactions between the [LaO] and [Cu*Ch*] layers in LaCuO*Ch* has been provided by two major

observations. First, the O 1s BEs experience small shifts on proceeding from LaCuOSe to LaCuOTe, not because of inherent changes in the charge of the O atoms, but rather because of changes in the Madelung potential dominated by the diminishing charge of surrounding La atoms as the La–*Ch* interactions strengthen with greater substitution of Se by Te. Second, the trend in the intensity of the Se K-edge can be rationalized through hybridization of La- and *Ch*-based conduction states. Direct evidence for Cu–to–*Ch* charge transfer within the [Cu*Ch*] layers has now also been obtained through the observation of absorption-edge energy shifts and intensity changes in a pre-edge feature in the Cu K-edge spectra, as well as small shifts in the Se 3d BEs. The gradual nature of these BE and absorption edge shifts suggests that the electronic structure can be progressively tuned in these oxychalcogenides.

5.5 References

[1] S. Inoue, K. Ueda, H. Hosono, N. Hamada, Phys. Rev. B 64 (2001) 245211-1–245211-5.

[2] K. Ueda, K. Takafuji, H. Hiramatsu, H. Ohta, T. Kamiya, M. Hirano, H. Hosono, Chem. Mater. 15 (2003) 3692–3695.

[3] H. Hiramatsu, H. Kamioka, K. Ueda, M. Hirano, H. Hosono, J. Ceram. Soc. Jpn. 113 (2005) 10–16.

[4] H. Hiramatsu, K. Ueda, H. Ohta, T. Kamiya, M. Hirano, H. Hosono, Appl. Phys. Lett. 87 (2005) 211107-1–211107-3.

[5] K. Ueda, H. Hiramatsu, M. Hirano, T. Kamiya, H. Hosono, Thin Solid Films 496 (2006) 8–15.

[6] H. Hiramatsu, H. Kamioka, K. Ueda, H. Ohta, T. Kamiya, M. Hirano, H. Hosono, Phys. Status Solidi A 203 (2006) 2800–2811.

[7] H. Hiramatsu, H. Yanagi, T. Kamiya, K. Ueda, M. Hirano, H. Hosono, Chem. Mater. 20 (2008) 326–334.

[8] R. Pöttgen, D. Johrendt, Z. Naturforsch. B 63 (2008) 1135–1148.

[9] S.J. Clarke, P. Adamson, S.J.C. Herkelrath, O.J. Rutt, D.R. Parker, M.J. Pitcher, C.F. Smura, Inorg. Chem. 47 (2008) 8473–8486.

[10] B.I. Zimmer, W. Jeitschko, J.H. Albering, R. Glaum, M. Reehuis, J. Alloys Compd. 229 (1995) 238–242.

[11] P. Quebe, L.J. Terbüchte, W. Jeitschko, J. Alloys Compd. 302 (2000) 70–74.

[12] Y. Kamihara, H. Hiramatsu, M. Hirano, R. Kawamura, H. Yanagi, T. Kamiya, H. Hosono, J. Am. Chem. Soc. 128 (2006) 10012–10013.

[13] H. Takahashi, K. Igawa, K. Arii, Y. Kamihara, M. Hirano, H. Hosono, Nature 453 (2008) 376–378.

[14] Y.-W. Ma, Z.-S. Gao, L. Wang. Y.-P. Qi, D.-L. Wang, X.-P. Zhang, Chin. Phys. Lett. 26 (2009) 037401-1–037401-4.

[15] P.E.R. Blanchard, B.R. Slater, R.G. Cavell, A. Mar, A.P. Grosvenor, Solid State Sci. 12 (2010) 50–58.

[16] P.E.R. Blanchard, R.G. Cavell, A. Mar, J. Solid State Chem. 183 (2010) 1477–1483.

[17] B.W. Rudyk, P.E.R. Blanchard, R.G. Cavell, A. Mar, J. Solid State Chem. 184 (2011) 1649–1654.

[18] P.E.R. Blanchard, R.G. Cavell, A. Mar, J. Solid State Chem. 183 (2010) 1536–1544.

[19] A.M. Baergen, P.E.R. Blanchard, S.S. Stoyko, A. Mar, Z. Anorg. Allg. Chem. doi:10.1002/zaac.201100238.

[20] K. Ueda, H. Hosono, Thin Solid Films 411 (2002) 115–118.

[21] N. Fairley, CasaXPS, version 2.3.9, Casa Software Ltd., Teighnmouth, Devon, UK, 2003, http://www.casaxps.com.

[22] B. Ravel, M. Newville, J. Synchrotron Radiat. 12 (2005) 537–541.

[23] R. Tank, O. Jepsen, A. Burkhardt, O.K. Andersen, TB-LMTO-ASA Program, Version 4.7, Max Planck Institut für Festkörperforschung, Stuttgart, Germany, 1998.

[24] A.J. Signorelli, R.G. Hayes, Phys. Rev. B 8 (1973) 81–86.

[25] G. Crecelius, G.K. Wertheim, D.N.E. Buchanan, Phys. Rev. B 18 (1978) 6519–6524.

[26] S.-J. Oh, G.-H. Kim, G.A. Sawatzky, H.T. Jonkman, Phys. Rev. B 37 (1988) 6145–6152.

[27] W. Grünert, U. Sauerlandt, R. Schlögl, H.G. Karge, J. Phys. Chem. 97 (1993) 1413–1419.

[28] E. Talik, A. Novosselov, M. Kulpa, A. Pajaczkowska, J. Alloys Compd. 321 (2001) 24–26.

[29] A. Novosselov, E. Talik, A. Pajaczkowska, J. Alloys Compd. 351 (2003) 50–53.

[30] S.K. Chawla, N. Sankarraman, J.H. Payer, J. Electron Spectrosc. Relat. Phenom. 61 (1992) 1–18.

[31] A.C. Miller, G.W. Simmons, Surf. Sci. Spectra 2 (1993) 55–60.

[32] S.W. Gaarenstroom, N. Winograd, J. Chem. Phys. 67 (1977) 3500–3506.

[33] C.D. Wagner, A.V. Naumkin, A. Kraut-Vass, J.W. Allison, C.J. Powell, J.R. Rumble Jr., NIST X-ray Photoelectron Spectroscopy Database, version 3.5 (web version), National Institute of Standards and Technology, Gaithersburg, MD, 2003, http://srdata.nist.gov/xps.

[34] A.R. Gerson, T. Bredow, Surf. Interface Anal. 29 (2000) 145–150.

[35] P.A.W. van der Heide, Surf. Sci. 490 (2000) L619–L626.

[36] P.A.W. van der Heide, J. Electron Spectrosc. Relat. Phenom. 151 (2006) 79–91.

[37] A.P. Grosvenor, R.G. Cavell, A. Mar, J. Solid State Chem. 181 (2008) 2549–2558.

[38] T. Chattopadhyay, A. R. Chetal, J. Phys. C: Solid State Phys. 18 (1985) 5373–5378.

[39] J.M. Brown, L. Powers, B. Kincaid, J.A. Larrabee, T.G. Spiro, J. Am. Chem. Soc. 102 (1980) 4210–4216.

[40] B. Joseph, A. Iadecola, L. Simonelli, Y. Mizuguchi, Y. Takano, T. Mizokawa, N.L. Saini, J. Phys.: Condens. Matter 22 (2010) 485702-1–485702-5.

[41] C.L. Chen, C.L. Dong, J.L. Chen, J.-H. Guo, W.L. Yang, C.C. Hsu, K.W. Yeh, T.W. Huang, B.H. Mok, T.S. Chan, J.F. Lee, C.L. Chang, S.M. Rao, M.K. Wu, Phys. Chem. Chem. Phys. 13 (2011) 15666–15672.

[42] C.L. Chen, S.M. Rao, C.L. Dong, J.L. Chen, T.W. Huang, B.H. Mok, M.C. Ling, W.C. Wang, C.L. Chang, T.S. Chan, J.F. Lee, J.-H. Guo, M.K. Wu, Europhys. Lett. 93 (2011) 47003-1–47003-5.

[43] J.H. Scofield, Theoretical Photoionization Cross Sections from 1 to 1500 keV, Lawrence Livermore Laboratory Report (1973) UCRL-51326.

[44] A. Kisiel, P. Zajdel, P.M. Lee, E. Burattini, W. Giriat, J. Alloys Compd. 286 (1999) 61–65.

[45] L.G. Parratt, C.F. Hempstead, E.L. Jossem, Phys. Rev. 105 (1957) 1228–1232.

[46] E.A. Stern, K. Kim, Phys. Rev. B 23 (1981) 3781–3787.

Chapter 6

Conclusion

The synthesis and characterization of new quaternary chalcogenides ($RE_3MM'Ch_7$) as well as in-depth analyses of the electronic structures of known quaternary chalcogenides (*RE*CuO*Ch*) has illustrated an example of synthetic strategies to target desired physical properties. The observed trends will be useful to future investigators to fine tune these properties. This thesis, while focusing more on the electronic structures, also presents structural information which could have a profound impact on the potential uses of the compounds presented, such as ferroelectric devices and NLO materials. One difference between these two groups of compounds is the presence of oxygen in one set, which effectively separates the contents of this work into 1D and 2D structures. In this chapter, the results from this thesis are summarized and the complications arising from the application of XPS and XANES are discussed.

6.1 Choosing an electronegativity scale

In Chapter 1, it was noted that electronegativity arguments are often invoked to explain electron transfer when interpreting XPS and XANES spectra, and to account for bonding. However, electronegativity scales are numerous and choosing an appropriate one becomes an important task that must be done on a

case-by-case basis. In situations where there is a large electronegativity difference between an element and its neighbours, significant electron transfer occurs and the chosen scale is less important. However, in situations where there is a smaller electronegativity difference, the choice of scale becomes important. For example, XPS and XANES excitation and emission processes are best modeled by the Allred-Rochow and Allen scales, whereas bonding and hybridization schemes are better described by the Mulliken-Jaffé and Pauling scales. The other important aspect of scale choice is consistency; care must be taken not to mix scales to explain results. With more than four scales to choose from, inconsistency may allow for unrealistic explanations. Of course, anomalies are inevitable; however, application of a more appropriate scale can alleviate some of these anomalies. This work provides some experimental support of electronegativity scales. The observation of chalcogen BE shifts (relative to the element) in LaCuO*Ch* (*Ch* = S, Se, Te) that change systematically with chalcogen (Chapter 4) are inconsistent with the Allred-Rochow and Pauling scales; the assumptions inherent to these scales do not apply in this situation. Specifically, in the Allred-Rochow scale, the electrostatic force felt by the electron is determined for the covalent radius of the element. The chalcogenides presented throughout this work have a negative charge which would decrease their electronegativity through an increase in radius. The results, which are more in line with the Allen scale, suggest that more work needs to be done for the fine-tuning of various electronegativity scales.

6.2 X-ray spectroscopy of complex compounds

In the past, XPS and XANES have typically been used, superficially, to determine oxidation states of ionic compounds because observed shifts are large and the interpretation is relatively simple. Only recently have these techniques been employed to examine the electronic structures of complex compounds exhibiting a wide range of bonding encompassing different degrees of ionic, covalent, and metallic character. Some of the shifts observed in non-ionic systems can often be lower than 0.1 eV, which is at the limit of precision in X-ray spectroscopy.

In accordance with traditional use, XPS was first used to identify valence states in the materials, and each set of compounds provided their own idiosyncrasy. In $(La^{3+})_3(Fe^{2+})(In^{3+})(S^{2-})_7$, and $La^{3+}Cu^{1+}O^{2-}Ch^{2-}$, the valence states for Fe, La, and Cu, were determined through analysis of complex features in the XPS spectra arising from final-state effects. The assignment of La^{3+} was deduced by the presence of satellite peaks. The differentiation of Cu^{1+} and Cu^{2+} was made by noting the absence of satellite peaks or broadening of core-line peaks. The presence of high-spin Fe^{2+} was confirmed by the occurrence of multiplet splitting leading to a complex energy envelope that was resolved by comparison with theoretical spectra. These are situations where final-state effects can actually help with charge identification; however, one of the drawbacks of XPS is its occasional inability to assign charge in cases with debilitatingly strong final state effects or severe delocalization such as in strongly covalent or metallic systems. The oxidation state of Co in La_3CoInS_7 is difficult to determine precisely because

of such delocalization through a shift to more metallic nature, as evidenced by the Fermi level cutting states in the DOS curve. Only the spectrum of the Co 2p core level, and not of the other components in La_3CoInS_7, exhibits a characteristic asymmetric tail. This suggests that delocalization only occurs on the transition metal site, implying that metallic conduction may take place within the 1D chains of metal-centred octahedra. Although surprisingly little analysis has been made previously on Ga L-edge XANES spectra, the investigation of RE_3MGaCh_7, indicate the presence of Ga^{3+} in accordance with expectations.

In this work, significant advances have been made to quantify the degree of electron transfer using X-ray techniques, which is important for understanding not only these compounds, but also other technologically important materials (e.g., superconductors). The target compounds occur in two structure types: the hexagonal chalcogenides $RE_3MM'Ch_7$ and the tetragonal oxychalcogenides LaCuO*Ch*. While there is no direct structural relationship between the two, both contain portions that are apparently isolated. The former is composed of isolated chains of transition-metal octahedra (trigonal antiprisms) and triel-centred tetrahedra separated by tricapped trigonal prismatic rare-earth atoms, and the latter comprises stacked layers of alternating [*RE*O] and [Cu*Ch*] layers. Although modeling of the broad transitions in the χ vs T plots observed for $La_3M InS_7$ (*M* = Fe, Co, and Ni) as isolated 1D systems proved insufficient in this case, it has been used in the past for treatment of similar transitions in related compounds. As well, as discussed in Chapter 1, the current theories for explaining the transparent electronic properties of the oxychalcogenides revolves around the existence of

MQWs created by an independent conducting layer sandwiched between two insulating layers. Probing the isolation is important, and was done using XPS and XANES. The results are summarized in Table 6-1

Table 6-1 Electronic information from XPS and XANES analysis.

Compound	Charge formulation	Isolated portion	Transfer to/from	Transfer within
La_3FeInS_7	$(La^{3+})_3(Fe^{2+})(In^{3+})(S^{2-})_7$	1D chains of *M*-centered octahedra and *M′*-centered tetrahedra	No	Yes
La_3MInS_7 (*M* = Co, Ni)	Co & Ni unknown from XPS. Ga^{3+} from XANES		No	Yes
RE_3MGaS_7			No	Yes
LaCuO*Ch*	$La^{3+}Cu^{+}O^{2-}Ch^{2-}$	[LaO] & [Cu*Ch*] layers	Yes	Yes
$LaCuOSe_{1-x}Te_x$			Yes	Yes

Varying degrees of electron transfer were found for both structures, summarized in Figure 6-1. For $RE_3MM'Ch_7$, discussed in Chapter 2 and 3, rare-earth and transition-metal substitution had little effect on the local electronic structures of In and Ga as indicated by the essentially identical In 3d core-line and Ga L_3-absorption edge spectra in $RE_3MM'Ch_7$. This result suggests that these chains can be appropriately described as 1D, allowing for further development into interesting magnetic and electronic materials. Within the chains, electron transfer depended on the compound being examined. In all cases, clear shifts in XPS and XANES spectra support a highly ionic character in the In and Ga centred tetrahedra. A slight shift to lower absorption energy in the RE_3MGaSe_7 compounds indicate more covalent character induced by a smaller electronegativity difference. For LaCuO*Ch*, the initial observation of changes in La 3d satellite intensity suggested that as chalcogen size increased, greater orbital overlap was achieved, thus greater interlayer charge transfer was seen. This was

supported by a small increase in bond strength, as quantified by the integrated COHP values on proceeding from LaCuOS (0.11 eV/bond) to LaCuOSe (0.13 eV/bond) to LaCuOTe (0.17 eV/bond). The subtle nature of the changes warranted further investigation which was done on a solid solution $LaCuOSe_{1-x}Te_x$ (Chapter 5). Through repeated measurements on O 1s and Se 3d core-lines, the uncertainties of the XPS measurements were reduced, below the standard ±0.10 eV, which uncovered previously hidden shifts that were explained using charge transfer effects through an extended coordination sphere (Madelung potential). Firmer evidence of intralayer charge transfer was found through Cu K-edge XANES analysis in which changes in the pre-edge feature were attributed to Cu 3d/Ch 4p orbital mixing. This work is a significant extension in the applicability of XPS to detect charge transfer processes in complex compounds.

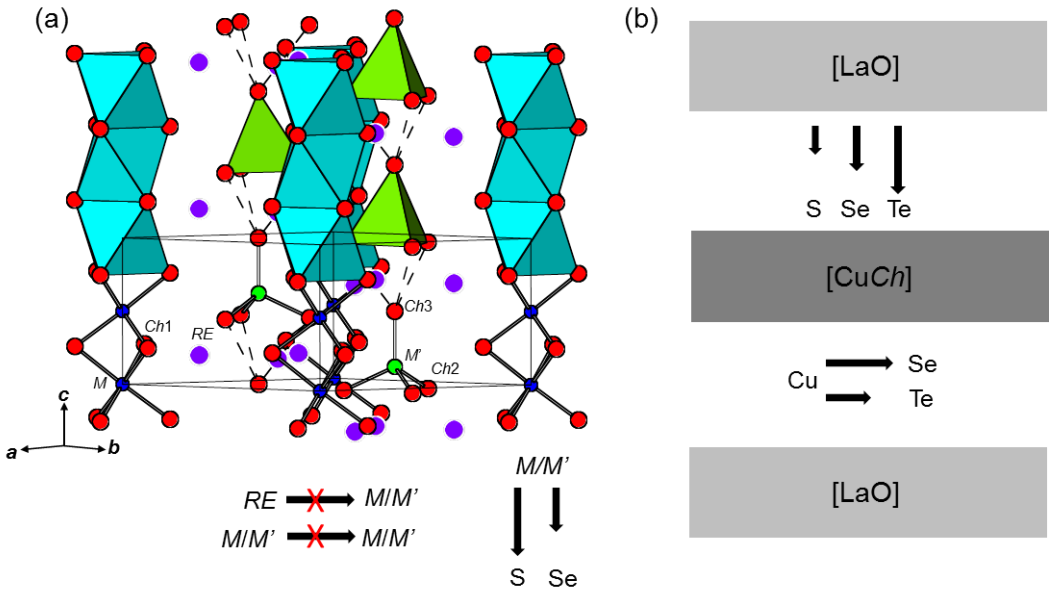

Figure 6-1 Charge transfer summary for (a) noncentrosymmetric $RE_3MM'Ch_7$ and (b) layered LaCuO*Ch*

An unexpected bonus of the XPS analysis completed in Chapter 4, on LaCuO*Ch*, was an observed correlation between Ch and core-line shift which could only be resolved if the electronegativity of Se was adjusted to a value intermediate between S and Te. This suggests that, in these compounds, the assumptions of the Allred-Rochow scale are not valid, and additional effort must be put into adjusting this electronegativity scale.

6.3 Crystal structure and properties of $RE_3MM'Ch_7$

Many new quaternary chalcogenides have been synthesized which represent a significant expansion of the $RE_3MM'Ch_7$ family of compounds. These contributions, in which the valences of the *M* and *M′* atoms are 2+ and 3+, respectively, are a subset of a larger family where the valence must sum to five, including the more well-explored 1+/4+ combination. The hexagonal structure, described previously, could potentially give rise to a wide variety of properties. Although significant rare-earth substitution (up to Dy) was attempted in the In-based samples, only a select few (6) gave the desired product while significantly more compounds (33) were formed when Ga was used instead, suggesting that significant size or electronic effects are at play.

The *c*/*a* ratios in the less numerous In compounds (0.62-0.63) were found to vary almost exclusively with *RE* substitution as the cell parameters (a = 10.128–10.147 Å; c = 6.276–6.864 Å) were little changed in the presence of different transition metals (Fe → Ni) although the limited scope of the series makes pinpointing the cause difficult. The more extensive Ga series presents a

clearer picture in which the *RE* component is primarily responsible for changes in the *c*/*a* ratio (0.59-0.64) through significant contractions in the *a*-axis (10.138Å–9.470 Å). Interestingly, the Ga compounds introduced another possible avenue to increase the asymmetry; slight increases in the *c*/*a* ratio are manifested as a shortening of the *M*–S bond distances in the transition-metal-centered octahedra, thus introducing asymmetry apart from the tetrahedra. We speculate that by progressively tuning the *c*/*a* ratio, noncentrosymmetry induced properties, such as piezoelectric and ferroelectric behaviour, may also be tuned.

The magnetic properties showed no clear dependence on structural change, but they fall into a variety of types. The vast majority are simply paramagnetic, with exceptions found in the Ce-based compounds, which show varying degrees of ferromagnetic behaviour (strongly non-linear χ^{-1} vs T curves), and the Tb-based compounds, which all show downturns in magnetic susceptibility indicative of antiferromagnetic ordering.

6.4 Future work

This work contains significant extensions of the application of XPS and XANES to layered compounds. It expands on previous work in our group, completed by Peter Blanchard, which focused primarily on the interlayer interactions (or lack thereof) of the potentially superconducting oxypnictides. In accordance with our expectations, interlayer interactions in the oxychalcogenides were preserved even upon pronounced chemical substitution. It would be very interesting to examine the extent of the interlayer interactions as a function of

rare-earth in which progressively smaller rare-earth atoms, in principle, may bring the separated layers closer together and induce greater interlayer charge transfer. Doing so may actually not enhance the observed properties, but could lead to additional areas of research dealing with methods to change the optical properties via increased layer isolation. Determining how hole mobilities and layer conductivities change as a result of these modification could lead to impressive tuning capabilities and significant enhancements in transparent electronics.

The newly discovered In- and Ga-containing noncentrosymmetric, quaternary chalcogenides have opened a huge array of new compounds to explore and properties to measure. Although primarily sulphur based, the Se analogues were shown to exist, but the extent of their formation is not known. The larger Se ions may limit the overall rare-earth substitution range to earlier members, but it may also open the door to include larger and heavier transition metals which may lead to possible applications as topological insulators given the small predicted band gap (~0.1-0.3 eV) of the Fe compounds. On the basis of different combinations of *M* and *M*′ whose valences sum to 5+ and the overall robustness of the structure, there are hundreds of potential new compounds within this family. There are many opportunities to measure optical properties of these compounds.

The tendency of unpaired d-electrons to absorbed visible light will likely destroy any non-linear optical processes which could be present in the compounds covered here, but this opens another avenue to pursue: the expansion of the II-III subfamily to filled d-shell variants (e.g., Zn^{2+}, Cd^{2+}, deficient Cu^{+}).

Preliminary attempts to extend RE_3MInS_7 beyond the title compounds in Chapter 4 have uncovered a new set of compounds of similar composition which adopt an orthorhombic structure (*Pnma*) and are nominally $RE_7MM'Ch_{13}$. Single crystals obtained (Nd_7FeInS_{13} and Pr_7CoInS_{13}) at the rare-earth cutoff for the $RE_3MM'Ch_7$ compounds suggest that a structural transition occurs probably as a result of size constraints. It remains unclear whether or not this represents a new structure type. All avenues of characterization for these compounds need to be completed as well as the appropriate substitutions. A summary of possible extensions of the work completed in this thesis is found in Table 6-2.

Table 6-2 Future work possibilities

Proposed compound	Probable structure	Purpose	Area
*RE*CuOCh (*RE* = Ce – Lu)	Layered chalcogenides (*P*4/*nmm*)	Tune interlayer charge transfer.	Optoelectronics
$La_2ZnO_2Ch_2$		Study effects of Zn compounds (known)[1] on electronic structure	Optoelectronics
$RE_3MM'Ch_7$ (*M* = Fe, Co, Ni; *M′* = In, Ga; *Ch* = Se, Te)	Hexagonal, noncentrosymmetric ($P6_3$)	Further c/a tuning. Property measurements	Ferroelectrics, pyroelectrics, piezoelectrics
RE_3(Zn,Cd)$M'Ch7$		Filled d-shell variants for NLO	NLO, SHG
$RE_7MM'Ch_{13}$	Orthorhombic (*Pnma*)	Possible new structure type	Unknown

6.5 References

[1] A.J. Tuxworth, E.E. McCabe, D.G. Free, S.J. Clark, J.S.O. Evans, Inorg. Chem. 52 (2013) 2078–2085.

Appendix 1

Supplementary Data for Chapter 2

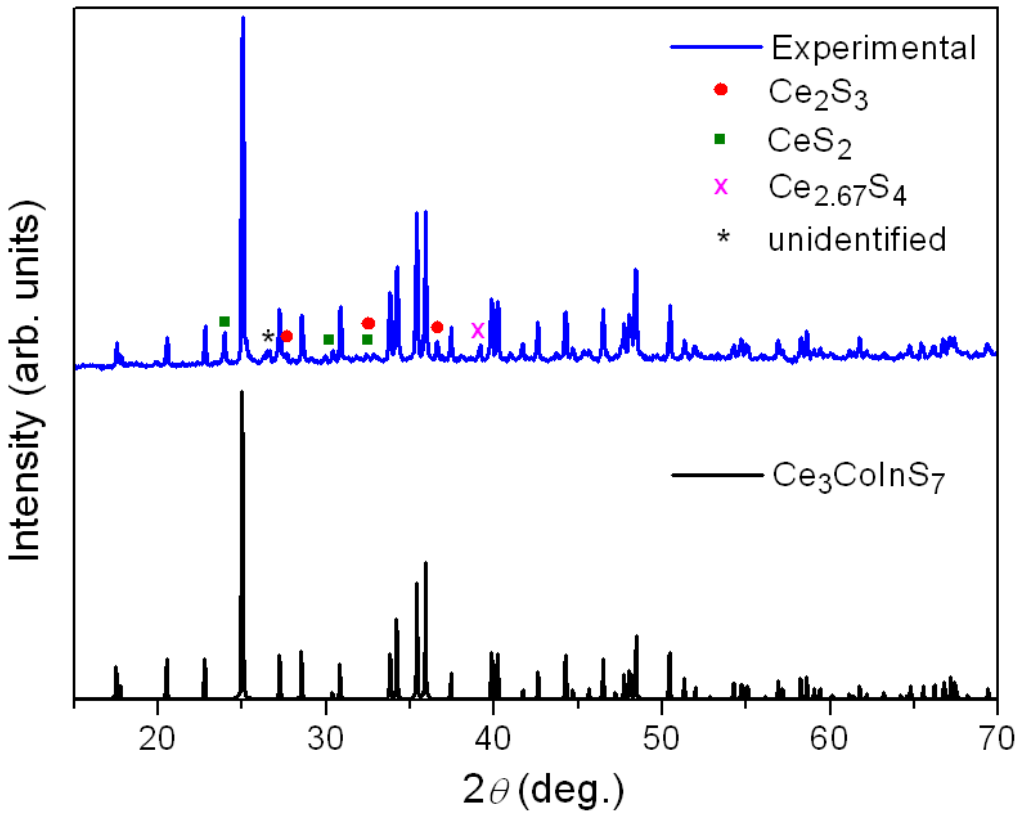

Figure A1-1 Powder XRD pattern for Ce_3CoInS_7.

Appendix 2

Supplementary Data for Chapter 4

Table A2-1 Integrated crystal orbital Hamilton populations (–ICOHP, eV per cell) for LaCuO*Ch*, LaNiAsO, and ZrCuSiAs.

	LaCuOS	LaCuOSe	LaCuOTe	LaNiAsO [a]	ZrCuSiAs [a]
Intralayer	La–O, 2.64	La–O, 2.68	La–O, 3.48	La–O, 2.56	Zr–Si, 6.00 Si–Si, 5.60
	Cu–S, 6.68	Cu–Se, 6.32	Cu–Te, 6.04	Ni–As, 7.52	Cu–As, 5.72
	Cu–Cu, 1.20	Cu–Cu, 1.24	Cu–Cu, 1.08	Ni–Ni, 0.68	Cu–Cu, 1.92
Interlayer	La–S, 0.44	La–Se, 0.52	La–Te, 0.68	La–As, 0.40	Zr–As, 6.92

[a] P. E. R. Blanchard, R. G. Cavell, A. Mar, J. Solid State Chem. 183 (2010) 1536–1544.

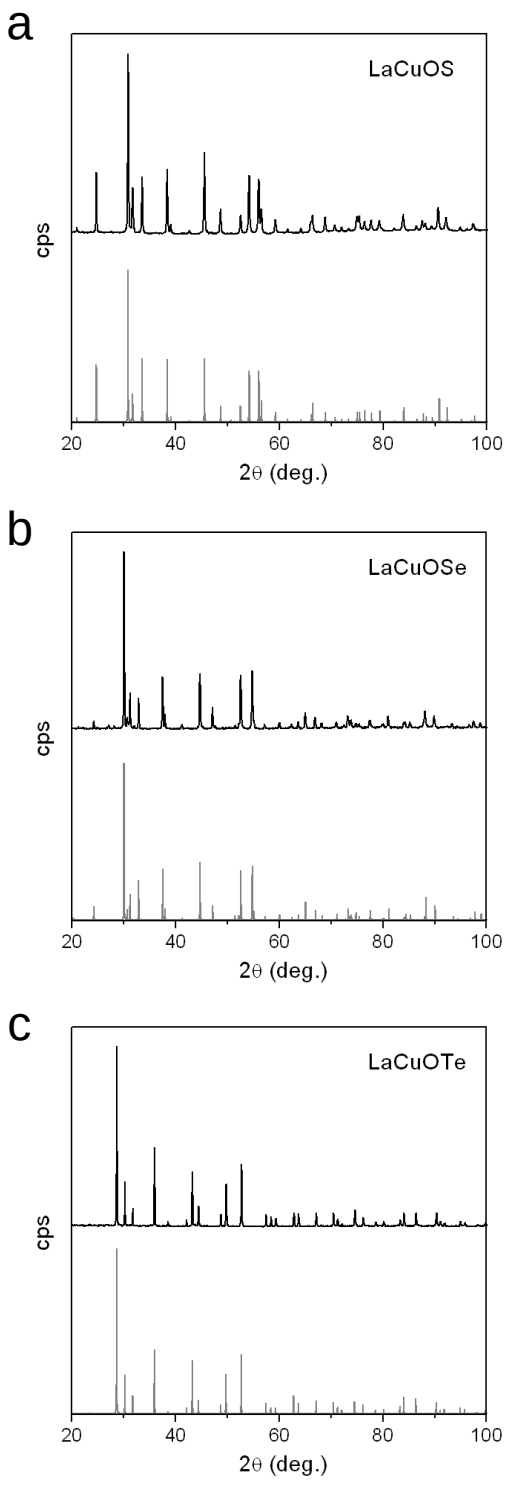

Figure A2-1 Powder XRD patterns for LaCuO*Ch* (*Ch* = S, Se, Te).

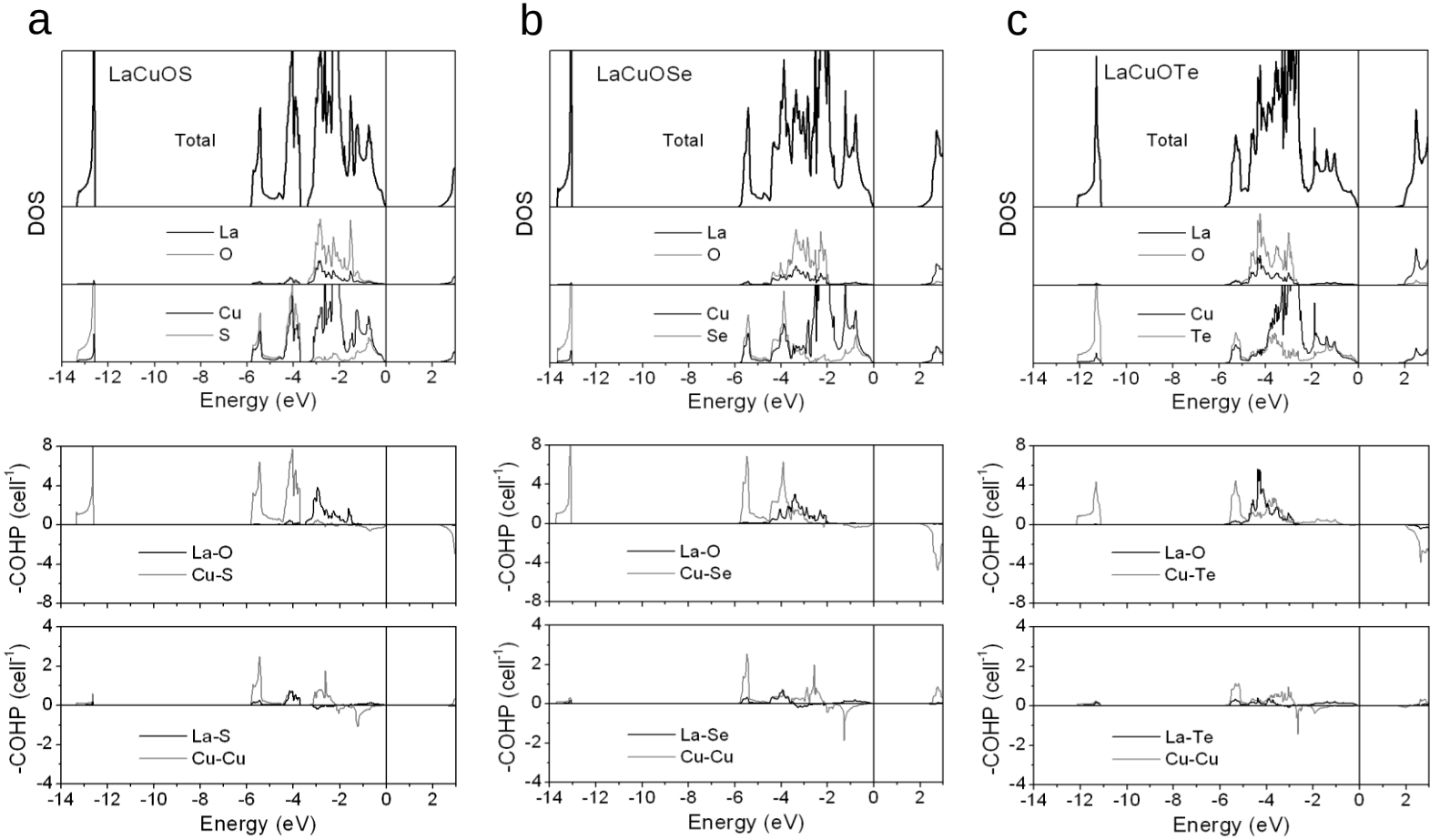

Figure A2-2 Density of states (DOS) with orbital projections and crystal orbital Hamilton population (COHP) curves for LaCuO*Ch* (*Ch* = S, Se, Te). The Fermi level is at 0 eV.

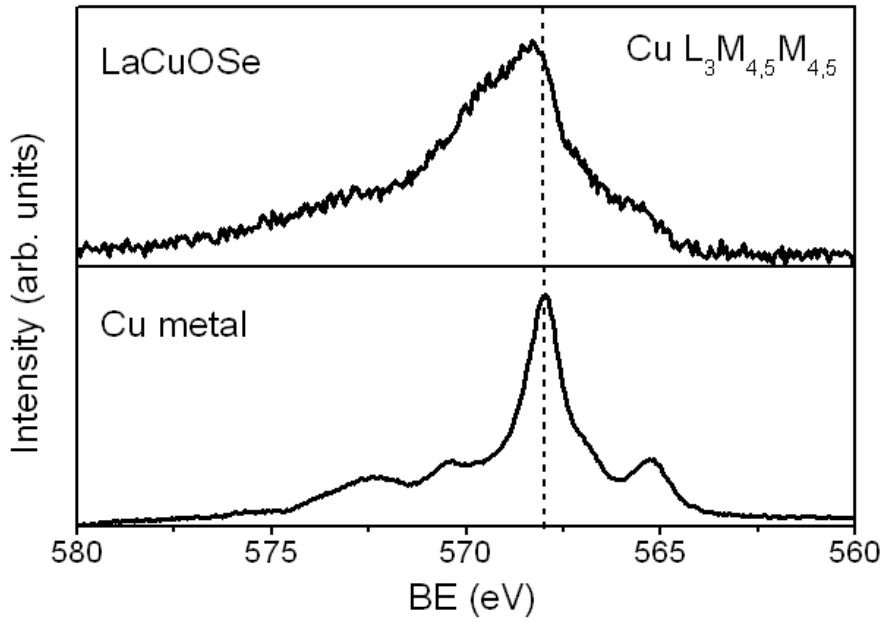

Figure A2-3 Cu Auger spectra for LaCuOSe and Cu metal, presented on a BE scale to facilitate comparison to the Cu XPS peaks. The dashed vertical line marks the BE for the Cu $L_3M_{4,5}M_{4,5}$ peak in Cu metal.

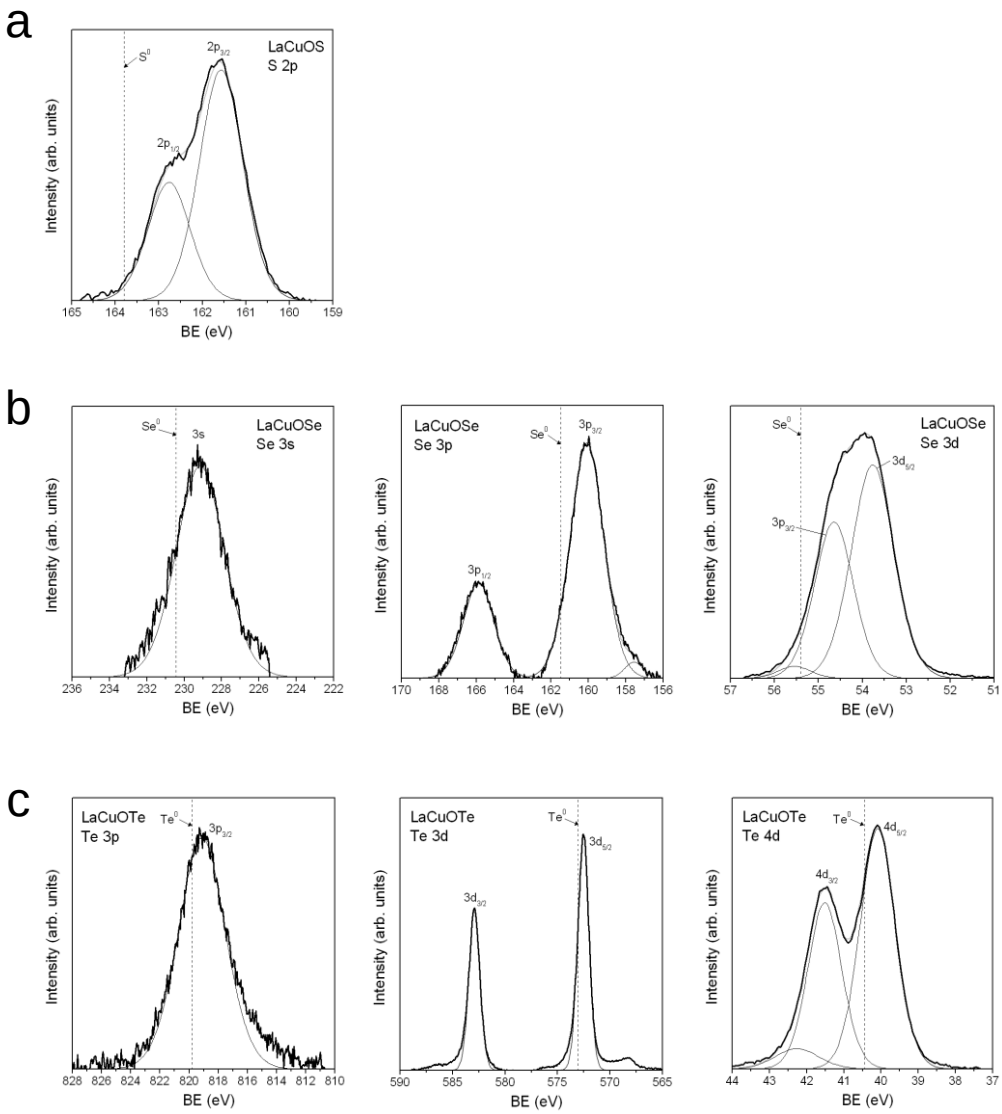

Figure A2-4 Core-line *Ch* XPS spectra for LaCuO*Ch* (*Ch* = S, Se, Te). The dashed vertical lines mark the BEs for the elemental chalcogens.

Appendix 3

Supplementary data for Chapter 5

Table A3-1 BEs (eV) for $LaCuOSe_{1-x}Te_x$ samples measured at different times.

Sample	Run 1	Run 2	Run 3
O 1s			
LaCuOSe	529.79	529.75	529.76
$LaCuOSe_{0.8}Te_{0.2}$	529.62	529.62	529.66
$LaCuOSe_{0.7}Te_{0.3}$	529.61	529.60	
$LaCuOSe_{0.6}Te_{0.4}$	529.59	529.57	529.58
$LaCuOSe_{0.4}Te_{0.6}$	529.53	529.49	529.51
$LaCuOSe_{0.2}Te_{0.8}$	529.44	529.43	529.39
LaCuOTe	529.72	529.73	529.75
Se $3d_{5/2}$			
LaCuOSe	53.93	53.93	53.93
$LaCuOSe_{0.8}Te_{0.2}$	53.85	53.86	53.86
$LaCuOSe_{0.7}Te_{0.3}$	53.85	53.85	
$LaCuOSe_{0.6}Te_{0.4}$	53.85	53.85	53.85
$LaCuOSe_{0.4}Te_{0.6}$	53.83	53.82	53.84
$LaCuOSe_{0.2}Te_{0.8}$	53.79	53.78	53.76

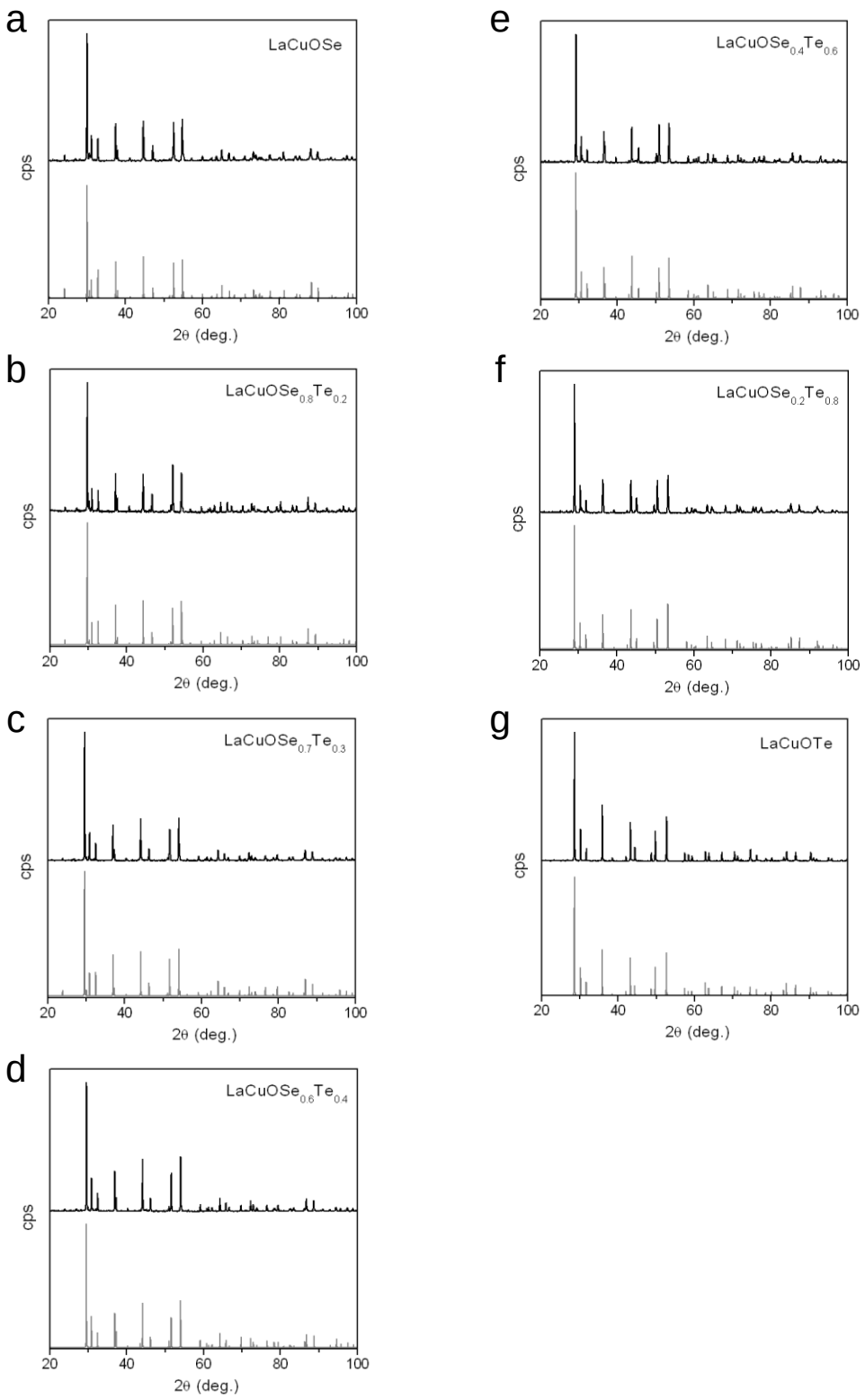

Figure A3-1. Powder XRD patterns for $LaCuOSe_{1-x}Te_x$.

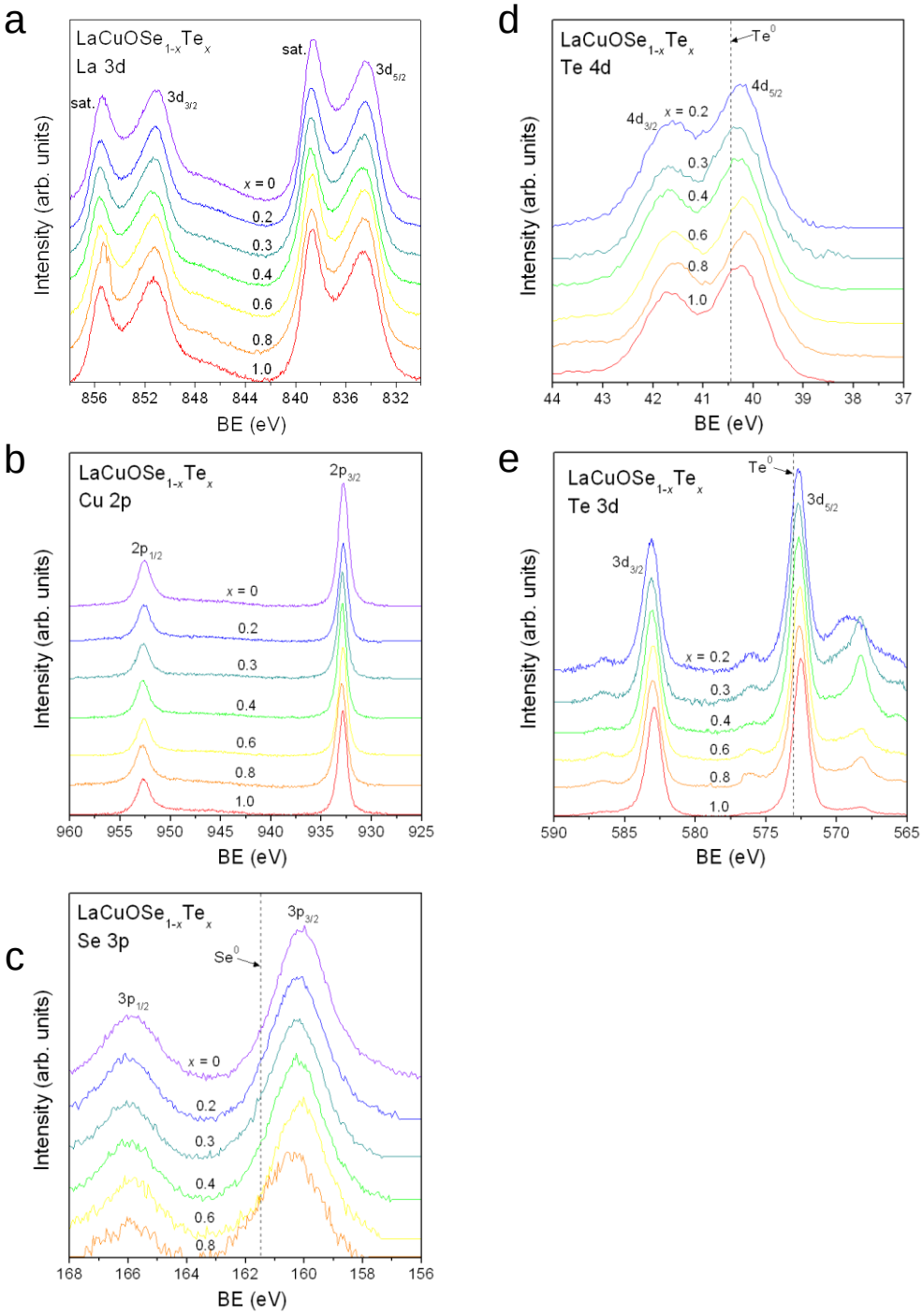

Figure A3-2. (a) La 3d, (b) Cu 2p, (c) Se 3p, (d) Te 4d, and (e) Te 3d core-line XPS spectra for $LaCuOSe_{1-x}Te_x$. Vertical dashed lines mark the BEs for the elemental chalcogens.

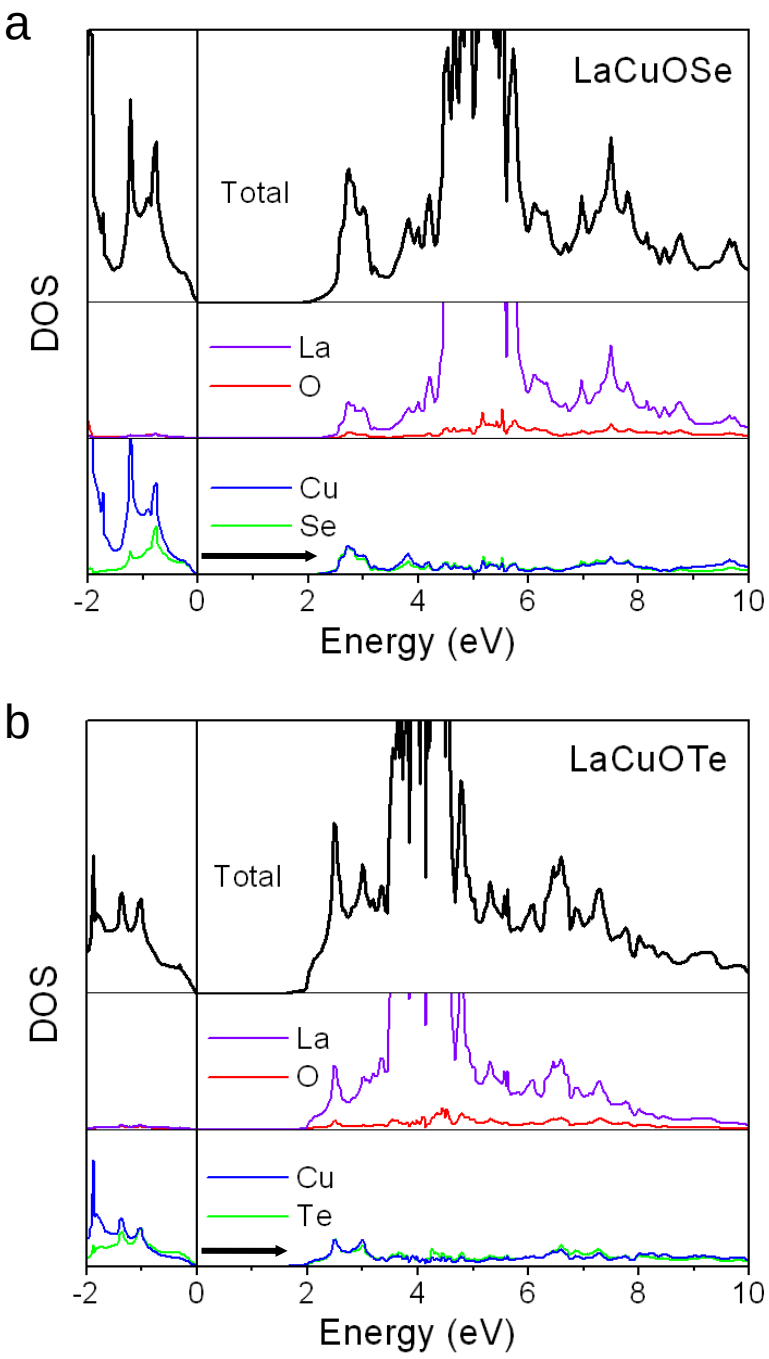

Figure A3-3. Calculated conduction states and orbital projections for (a) LaCuOSe and (b) LaCuOTe. The Fermi level is at 0 eV. The bold horizontal arrows highlight the beginning of the Cu 2p-based conduction band above the Fermi level.

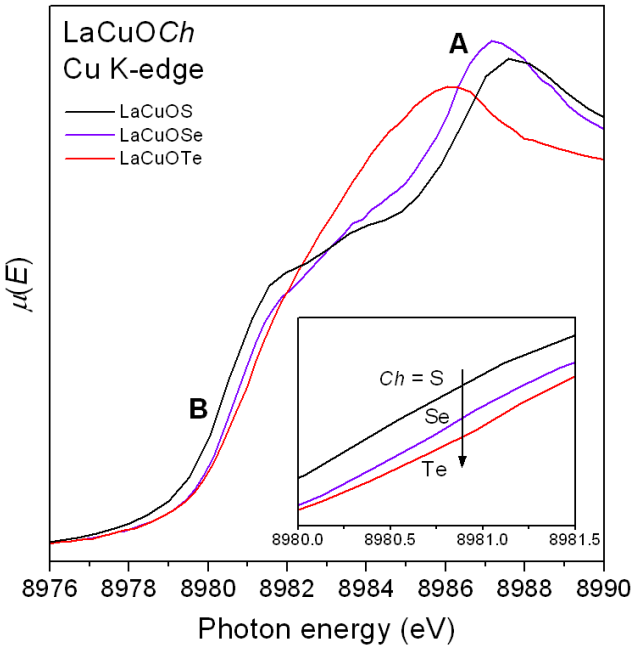

Figure A3-4. Cu K-edge XANES spectra for LaCuO*Ch* (*Ch* = S, Se, Te), with the inset highlighting the pre-edge region.